NTNU
Norwegian University of
Science and Technology

Two-Component Spin-Orbit Coupled Ultracold Atoms in the Weak and Strong Coupling Regimes

Even Thingstad

Abstract

Motivated by recent experimental advances, we study two-component spin-orbit coupled ultracold bosonic atoms in two dimensions on a square optical lattice. Using a Bose-Hubbard model with spin-conserving and non-spin-conserving nearest neighbour hoppings and spin-dependent on-site density-density interaction, our goal is to characterize phase separation and spin structure in the weakly interacting and deep Mott regimes. In the weakly coupled regime, we decouple interactions through a real space uniform density mean field theory. At zero temperature, this gives an analytic condition for the phase separation transition driven by inter- relative to intracomponent interaction. Solving the self-consistent equations at finite temperature reveals entropic remixing in the phase separated regime and a more surprising entropy driven phase separation in the mixed regime. This is a consequence of complex interplay between interaction and spin-orbit coupling, and can be explained through the effect of component imbalance on the effective single-particle dispersion relation. We also provide an alternate explanation based on thermal occupation of eigenstates with a characteristic imbalance. In the strongly interacting Mott regime, we derive an effective spin Hamiltonian describing the magnetic phases of the Mott insulator. The competition between anisotropic Heisenberg and Dzyaloshinskii-Moriya interactions gives rise to various ferromagnetic, antiferromagnetic, spiral, stripe, vortex, and skyrmion phases. On basis of classical Monte-Carlo simulations in the literature, we reconstruct the phase diagram with a classical variational approach, while magnon excitation spectra and quantum fluctuations are calculated with Holstein-Primakoff transformation and subsequent spin wave expansion. The analysis shows that states with ferromagnetic or antiferromagnetic ordering of boson species are protected against thermal fluctuations by a gap, and well described by classical states. States with equal superposition of boson species at each lattice site are subject to relatively large quantum fluctuations, which may cause breakdown of the states within their classical parameter space regions. The dispersion relations are gapless and linear around the minima to lowest order in the spin wave expansion.

i

Sammendrag

Med nylige eksperimentelle framskritt som bakteppe ser vi på spinn-bane-koblede ultrakalde boson-
iske atomer i to ulike hyperfine tilstander. For et dypt og kvadratisk optisk gitter i to dimensjoner
benytter vi en Bose-Hubbard-modell med tunnelering til nabogitterpunkter og frastøtende veksel-
virkning internt på hvert gitterpunkt. Målet med denne oppgaven er å se på faseseparasjon og
romlig spinntekstur i det svakt vekselvirkende og i Mottisolatorregimet av parameterrommet. For
den svakt vekselvirkende fasen antar vi uniform gass og benytter middelfeltsteori for komponent-
tetthetene. Ved null temperatur finner vi en analytisk betingelse for full faseseparasjon drevet
av forholdet mellom vekselvirkningen for atomer i ulike og i samme hyperfine tilstand. Ved en-
delig temperatur gir de selvkonsistente likningene gjeninnblanding av minoritetskomponenten i
den faseseparerte fasen og en mer overraskende entropidrevet faseseparasjon i den blandede fasen.
Sistnevnte er en mangepartikkeleffekt som oppstår som følge av komplisert samspill mellom spinn-
bane-kobling og vekselvirkning. Vi forklarer den ved hjelp av endringen i den effektive enpartikkel-
beskrivelsen komponentubalanse medfører. En alternativ forklaring tar utgangspunkt i den termisk
fyllingen av egentilstander med en karakteristisk ubalanse. For den sterkt vekselvirkende Mott-
isolatorfasen utleder vi en effektiv spinnmodell. Konkurranse mellom et anisotropt Heisenberg-
ledd og Dzyaloshinskii-Moriya-vekselvirkning fører til et mangfoldig fasediagram med ferromag-
netiske, antiferromagnetiske, spiral-, stripe-, virvel- og skyrmionfaser. På bakgrunn av klassiske
Monte-Carlo-simulasjoner rekonstruerer vi fasediagrammet ved hjelp av variasjonstilstander for de
ulike fasene. Eksitasjonsspektre og kvantefluktuasjoner studeres ved hjelp av Holstein-Primakoff-
transformasjon og påfølgende spinnbølgeutvikling. Tilstander med ferromagnetisk eller antiferro-
magnetisk ordning av atomene er beskyttet av gap i eksitasjonsspekteret, har minimale kvante-
fluktuasjoner og beskrives derfor godt av klassiske tilstander. Isolatortilstander med samtlige
atomer i jevn superposisjon av de hyperfine tilstandene har derimot relativt store kvantefluktua-
sjoner som bryter klassisk degenerasjon og som fører til ustabilitet for tilstrekkelig sterk Dzyaloshinskii-
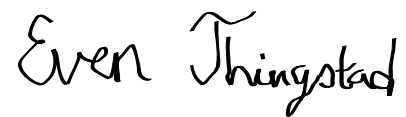Moriya-vekselvirkning.

Abbreviations

BEC	Bose-Einstein condensate
DM	Dzyaloshinskii-Moriya
IC	Incommensurate
MI	Mott insulator
S1	Spiral-1. Spiral phase in the plane spanned by $\hat{z}$ and $\hat{x} \pm \hat{y}$.
S2	Spiral-2. Spiral phase in the $\hat{x}$-$\hat{z}$ or $\hat{y}$-$\hat{z}$ plane.
SF	Superfluid
SkX	Skyrmion crystal
SOC	Spin-orbit coupling
VX	Vortex phase
zFM	Ferromagnet with ordering along the $\hat{z}$-axis.
zAFM	Antiferromagnet with ordering along the $\hat{z}$-axis.

Nomenclature

N	Number of lattice sites
t	Hopping amplitude of ordinary hoppings
$\beta_{l\delta}$	Spin-orbit coupling matrix
η	Off-diagonal term in $\beta_{l\delta}$ determining SOC strength in $\hat{y}$-direction.
κ	Off-diagonal term in $\beta_{l\delta}$ determining SOC strength in $\hat{x}$-direction or strength of Rashba SOC, where $\eta = -\kappa$
γ_x	Diagonal term in $\beta_{l\delta}$ determining SOC strength in $\hat{x}$-direction. Typically set to 0.
γ_y	Diagonal term in $\beta_{l\delta}$ determining SOC strength in $\hat{y}$-direction. Typically set to 0.
t_0	Combined hopping amplitude for ordinary and SOC-induced hoppings.
α	Gauge field strength determining relative importance of ordinary and SOC-induced hoppings in $\hat{x}$-direction.
β	Gauge field strength determining relative importance of ordinary and SOC-induced hoppings in $\hat{y}$-direction.
u	Intracomponent interaction strength.
λ	Inter- relative to intracomponent interaction strength.
$\mathcal{D}$	Dzyaloshinskii-Moriya interaction strength.
S	Spin quantum number or length of spin in classical spin model.

Preface

This Master thesis is the result of research conducted during the final year of the two year Master Program in Physics at the Norwegian University of Science and Technology (NTNU). I would like to thank my supervisor Prof. Asle Sudbø for invaluable guidance and enthusiastic support throughout the year. Many thanks go also to the friends and fellow physics students I have met during my years in Trondheim and Munich.

Even Thingstad
Trondheim, Norway
May 2017

Contents

Chapter 1

Introduction

1.1 Motivation and background

The complexity of interacting quantum many-particle systems is tremendous, and a challenge for classical computers [1]. An alternative is the use of quantum simulation, which is not based on numerical methods applied to some equation, but rather the time evolution of a highly controllable quantum system [2]. With their inherent quantum behaviour, tunability, and absence of impurities, cold atom systems are well suited for this [3]. Cooling atomic gases down to nanokelvin temperatures, one can make these systems simulate condensed matter physics and reach otherwise inaccessible parameter regimes, enabling the study of novel phenomena. The history of ultracold atoms and Bose-Einstein condensation already contains fascinating physics.

In 1924, Albert Einstein received a letter from the younger colleague S. N. Bose, who wanted his opinion on a paper on the statistical description of light [4]. Einstein was impressed, translated the article, and complemented it with a discussion on the implications for atomic gases. The two articles appeared alongside in Zeitschrift für Physik in 1924 [5, 6]. In a second article [7], Einstein went one step further and predicted the phenomenon nowadays known as Bose-Einstein condensation: the macroscopic occupation of a single quantum state.

Unfortunately, the applicability of any theory is not determined by how interesting it is. Due to the exceptionally low temperature required, Bose-Einstein condensation was for a long time regarded a curiosity without much relevance in real systems. This changed upon the experimental discovery of superfluid liquid helium in 1938 [8, 9]. Shortly after, Bose-Einstein condensation was proposed as underlying mechanism [10, 11], and Landau came up with the first phenomenological theory of superfluidity [12, 13]. In its simplest form, in spite of dragging an impurity through the condensate, excitations become impossible below a critical velocity determined by the condensate excitation spectrum. When Bogoliubovs analysis of the weakly interacting Bose-Einstein condensate showed a linear dispersion relation at small energies, the two approaches constituted the first microscopic theory of a superfluid [11, 13, 14]. The theoretical research continued the following years. Although Einsteins original paper still provides a satisfactory description of Bose-Einstein condensation in non-interacting systems, it was far from clear whether condensation was also possible in interacting systems [15, 16]. A definition was provided by Penrose and Onsager through the concept of off-diagonal long range order (ODLRO) [16, 17], but to this day, there is no general rigorous proof for condensation in interacting systems.

In 1995, 70 years after the theoretical prediction, Bose-Einstein condensation was realized in atomic gases. Groups lead by E. A. Cornell and C. E. Wieman at Boulder and W. Ketterle at MIT reached condensation temperatures using laser- and evaporative cooling for alkali atoms [11, 18–21]. The momentum distribution was measured with absorption imaging after a time-of-flight expansion, and developed an additional non-Gaussian peak below the condensation temper-

ature, corresponding to the macroscopic ground state occupation predicted by Einstein. For these achievements, Cornell, Wieman, and Ketterle shared the 2002 Nobel prize.

The experimental realization caused a boom in the experimental and theoretical research on Bose-Einstein condensates. Soon, several groups had achieved Bose-Einstein condensation, and the techniques for its realization were becoming standard [20]. Nowadays, in the words of Galitski and Spielman [22], while "theorists create spherical cow models, in cold atom physics, experimentalists can actually make spherical cows". Among the many examples of tunability, one can instantaneously turn off the trapping potential, tune interactions between atoms with Feshbach resonances [23], and generate periodic potentials using laser-induced dipole oscillations [24]. The latter is particularly important because it is a prerequisite to simulate many condensed matter systems.

In the experiments with ^{87}Rb of the Boulder group, as a mere coincidence, it was discovered that the condensate was split into two clouds with particles in different hyperfine states [21, 25]. Since a particle can be in any superposition of hyperfine states, particles in two-component boson mixtures can be attributed a pseudo-spin [26]. This raises the question of whether exotic phenomena related to spin in massively studied electronic systems can be realized and simulated with cold atoms. Unlike electrons, atoms do not have a net charge, so the physical origin must necessarily be different, but innovative use of magnetic fields and lasers can typically provide an implementation.

An example of an effect for which electron spin is at the forefront, is spin-orbit coupling. For electrons, this is a relativistic correction to the non-relativistic Schrödinger equation [27]. For rotationally symmetric potentials in atomic physics, it is manifest as coupling between the orbital and spin angular momenta of the electron, contributing to the fine structure [28]. More generally, there is spin-orbit coupling in the presence of an electric field. Using symmetry considerations and group theory, splitting of energy bands in semiconductors cubic in quasimomentum was found theoretically by Dresselhaus [29]. Rashba and Sheka found splitting linear and isotropic in momentum [30, 31], while Bychov and Rashba later found a similar effect in the two-dimensional electron gas [32]. Spin-orbit coupling is also of interest in the rapidly developing field of spintronics [33], where the goal is manipulation of spin in condensed matter systems. Magnetization of ferromagnetic domains through spin-orbit coupling has applications in data storage and memory handling [26].

Although SOC has been well known for a long time, the last decade, it has attracted massive attention due to the realization that it can lead to topological insulators [34, 35]. In the quantum Hall effect, a strong magnetic field breaks time-reversal invariance and causes conducting surface states, even if the bulk is insulating [22, 36]. These states are protected by a topological invariant, and therefore extremely robust [37]. For spin-orbit coupled systems, strong magnetic fields are not necessary due to an additional topological invariant still capable of protecting the surface states [38, 39]. Topology is of relevance in many other systems as well, such as superfluids and magnets [11, 40, 41]. The 2016 Nobel prize was shared by D. J. Thouless, F. D. M. Haldane, and J. M. Kosterlitz for their study of topological phases of matter and topological phase transitions [40]. The new type of transition was ground breaking because it cannot be explained by spontaneous symmetry breaking in the Landau-Ginzburg-Wilson paradigm of phase transitions.

Motivated by this, we return to the question of whether a synthetic spin-orbit coupling can be realized in cold atom systems. For quite a long time, proposals on how to realize spin-orbit coupling existed [42, 43], but it was first achieved only in 2011 [44]. Again, this was a nice illustration of the flexibility shown by cold atom systems. Through the Doppler effect, Raman transitions between hyperfine states are made velocity dependent, thus providing the coupling between momentum and pseudo-spin required by SOC [22]. As with the first realization of BEC in atomic gases, this sparked interest in the community. The following years saw measurements of properties such as excitation spectra [45, 46], lack of Galilean invariance [47], phase separation, and spin textures [44, 48–50]. The observation of Zitterbewegung is a particularly nice demonstration of the simulative power of spin-orbit coupled cold atom systems [51, 52]. Predicted from the Dirac equation almost 90 years ago, its measurement remains out of reach for electrons [53, 54].

All the experiments above use a one-dimensional spin-orbit coupling equivalent to an equal

linear combination of Rashba and Dresselhaus SOC. The realization of their general linear combination was achieved in 2016 [55, 56], following the realization in atomic Fermi gases earlier the same year [57, 58]. This opens new possibilities for the study of two-dimensional topological insulators, possibly also in bosonic systems.

More than 20 years of Bose-Einstein condensation in atomic gases have shown that an experimental breakthrough is typically followed by rapid replication and subsequent standardization of techniques forming a basis for further study. Mixtures of ultracold atoms can be used to simulate effects of spin-orbit coupling, with exciting prospects for topological insulators and applications in spintronics. Spin-orbit coupled ultracold atoms is therefore an active and rapidly developing research field.

1.2 Structure of thesis

Chapters 5 and 6 form the main body of this thesis, while chapters 1-4 provide an introduction to the systems we are studying and their theoretical description. In chapter 7, we conclude. There are two appendices. Below, we provide a more detailed description of the contents in each chapter.

In chapter 2, we give some conventions used throughout the thesis, and discuss some basic concepts. Then, we present the less trivial Bogoliubov transformation generalized to more than two boson species. We will need this when analysing spin model excitation spectra in chapter 6.

In chapter 3, we provide an introduction to cold atom systems and their experimental realization. We then formulate the basics of spin-orbit coupling, and calculate the well known dispersion relation of the spin-orbit coupled Bose gas in the continuum.

In chapter 4, we derive a Bose-Hubbard model for spin-orbit coupled systems which serves as starting point for the remainder of the thesis. We then discuss the single species superfluid to Mott insulator transition (SF-MI) and some recent articles treating the spin-orbit coupled case.

Applying a homogeneous density mean field theory, we study the Bose-Hubbard model in the weak coupling limit in chapter 5, discussing the phase separation transition occurring due to inter-component interaction.

In chapter 6, we go to the opposite limit of strong interactions. First, we derive an effective spin Hamiltonian, before studying it with a classical variational approach. Finally, we study quantum fluctuations by means of the Holstein-Primakoff transformation.

In chapter 7, we conclude. In appendix A, we discuss some aspects of self-consistent determination of mean field parameters relevant for chapter 5. In appendix B, we present the details of the effective spin model derivation in chapter 6.

Chapter 2

Preliminaries

2.1 Mathematical conventions

We typically follow common conventions in physics.

Vectors are denoted by boldface letters, for instance position $\mathbf{r}$, momentum $\mathbf{k}$, and gauge field $\mathbf{A}$. Exceptions include the Cartesian unit vectors $\hat{x}$, $\hat{y}$, and $\hat{z}$, and the vector of Pauli matrices $\vec{\sigma}$, where we use the standard definitions

$$\sigma^x = \begin{pmatrix} 0 & 1 \\ 1 & 0 \end{pmatrix} \qquad \sigma^y = \begin{pmatrix} 0 & -i \\ i & 0 \end{pmatrix} \qquad \sigma^z = \begin{pmatrix} 1 & 0 \\ 0 & -1 \end{pmatrix}. \tag{2.1}$$

Column vectors describing spin structure are also not typeset as bold, and neither are matrices. The transpose of a matrix P is denoted by P^T, while $P^\dagger$ and P^* denote the hermitian and complex conjugate matrices. We also let h.c. denote the hermitian conjugate, so that $O + \text{h.c.} = O + O^\dagger$.

Throughout this thesis, we will be using several indices. Various momenta or quasi-momenta are typically denoted by $\mathbf{q}$ or $\mathbf{k}$, although we drop the boldface notation if such a momentum occurs in a sub- or superscript. Indices i and j typically refer to lattice sites, while σ refers to spin components, and l, δ, and m refer to one of the spatial directions in a two-dimensional system, namely x or y.

Expectation values are denoted by brackets, and we use natural units with $\hbar = k_B = 1$. In plots, dimensionful labels on the axes must typically be interpreted in units of a characteristic system scale with the same physical dimension, for instance the ordinary hopping rate t in chapter 5.

Considering a square lattice Hamiltonian, for instance the Heisenberg model

$$H = -J \sum_{\langle ij \rangle} \mathbf{S}_i \cdot \mathbf{S}_j = -2J \sum_{i,\delta} \mathbf{S}_i \cdot \mathbf{S}_{i+\delta}, \tag{2.2}$$

nearest neighbour summation is denoted by $\langle ij \rangle$, and is understood to include also the term where i and j are interchanged. This leads to the factor 2 in the equivalent second form, where we include only $\delta \in \{\hat{x}, \hat{y}\}$. We typically set the lattice constant to 1.

2.2 Bose-Einstein condensation

In this section, we go through the basic mechanism of Bose-Einstein condensation of non-interacting particles, and discuss in particular the importance of system dimensionality and low energy behaviour of the dispersion relation.

Consider a d-dimensional quantum system of bosons where possible states are characterized by quasimomentum vector $\mathbf{k}$ and energy E_k, where $\mathbf{k} = 0$ is a minimum of the dispersion relation. In the Grand Canonical Ensemble, eigenstate occupation numbers are controlled by a chemical potential μ, and given by

$$n_k = \frac{1}{e^{\beta(E_k - \mu)} - 1}, \tag{2.3}$$

where $\beta = 1/T$ is the inverse temperature. To have non-negative occupation numbers, we require μ to be smaller than the ground state energy E_0. Assume $E_0 = 0$. For small temperatures, μ must be tuned close to 0 to obtain significant densities, and the low temperature means that only low energy modes can contribute. Assume therefore a power-law dependence

$$E_k = Ck^\nu, \tag{2.4}$$

where we for simplicity have assumed a rotationally symmetric dispersion relation. We now aim at relating the density ρ of the system with the chemical potential. In the thermodynamic limit, one may rewrite the sum over the eigenstate occupation numbers in (2.3) as an integral,

$$\rho = \frac{1}{V} \frac{1}{e^{\beta(E_0 - \mu)} - 1} + \frac{1}{V} \int \frac{D(E)}{e^{\beta(E - \mu)} - 1} dE, \tag{2.5}$$

where $D(E)$ is the density of states and V the volume. Depending on dimension and the low energy behaviour ν, the integral above can be limited to a finite maximum value at $\mu = 0$, for instance for the free Bose gas in 3 dimensions. Below a critical transition temperature, particles have to condense into the minimum. We now derive conditions on ν and the dimension for this to happen.

The density of states is

$$D(E) = \sum_k \delta(E - E_k) \propto \int dk \; k^{d-1} \delta(E - Ck^\nu) \tag{2.6}$$

Calculating the delta function integral gives $D(E) \propto E^{d/\nu - 1}$. The maximum density ρ_{ex} of particles in excited states is then

$$\rho_{\mathrm{ex}} \propto \int dE \frac{E^{d/\nu - 1}}{e^{\beta E} - 1}. \tag{2.7}$$

Possible divergences come from small energy, and by Taylor expanding the denominator, we have to consider $\int E^{d/\nu - 2} dE$. This diverges for $d/\nu - 2 \leq -1$, so Bose-Einstein condensation is only possible for $d > \nu$. As proclaimed, finite temperature Bose-Einstein condensation is possible for the free boson gas in 3 dimensions ($d = 3, \nu = 2$). In two-dimensional systems with quadratic dispersion, it is not, and this is an important result for us since we consider two-dimensional systems. In the strong coupling regime considered in chapter 6, we will however encounter dispersion relations linear in quasimomentum, for which finite temperature Bose-Einstein condensation is again possible.

2.3   Quantum mechanics in periodic potentials

The presence of a periodic potential is characteristic for many condensed matter systems. We therefore give a brief review of quantum mechanics in periodic potentials. In particular, since we in chapter 4 want to derive the Bose-Hubbard model on an optical lattice, we discuss Wannier functions in a harmonic potential.

Consider a periodic potential $V(x)$ with lattice constant a in one dimension. Since we later consider Hamiltonians separable with respect to spatial direction, this can easily be generalized to higher dimensions. The eigenfunctions of such a potential are Bloch waves, and on the form [59]
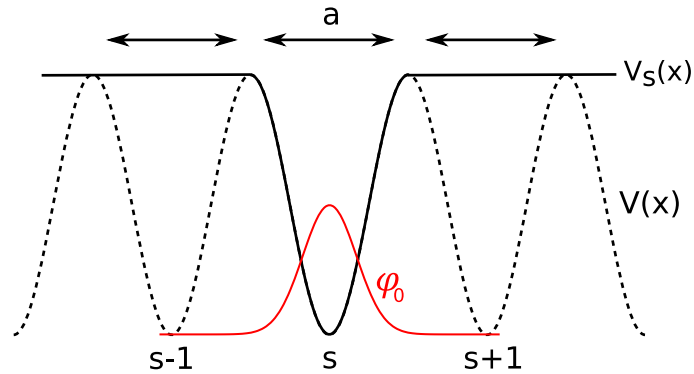
Figure 2.1: A periodic potential $V(x)$ may be though of as a sum over atomic potentials $V_s(x)$ corresponding to a given lattice site. In a deep lattice, bound states of these atomic potentials are well localized around the lattice site minimum and rapidly decaying.

$$\psi_k^n(x) = e^{ikx} u_k^n(x), \tag{2.8}$$

where k is known as the quasi- or crystal momentum, and $u_k^n(x)$ is periodic with the same periodicity as the lattice. The quasimomentum vectors can be taken to lie within the first Brillouin zone, $-\pi/a < k \le \pi/a$, and the energy spectrum forms bands $\{n\}$.

In the context of particles on an atomic lattice, the periodic potential is a sum over single-atom potentials. In the tight-binding approximation, the central assumption is that the potential close to an atom is approximated by the single atom Hamiltonian [60]. In the vicinity of this atom, we expect single-atom orbitals ϕ_0^n to be a good approximation to the eigenfunctions. By translational symmetry, this applies also for eigenfunctions localized around all other atoms. We work with an optical lattice, but can still think of the potential $V(x)$ as composed of localized potential wells $V_s(x)$, as illustrated in figure 2.1. With the ideal harmonic potential, outside the part of the real axis with length a corresponding to a given potential minimum s, the potential can be set to 0 exactly. Assuming the potential is deep, the eigenfunctions ϕ_s^n of $V_s(x)$ are well localized around lattice site minimum s at position x_s. One can then construct a linear combination of such eigenfunctions,

$$\frac{1}{\sqrt{N}} \sum_s e^{ikx} \phi_s^n(x), \tag{2.9}$$

which satisfies Blochs theorem assuming eigenfunctions are zero outside the spatial region of their designated lattice site. Since this is not strictly true, this linear combination is not an exact Bloch eigenfunction ψ_k^n, but for a deep lattice, it is a good approximation. Motivated by this, we introduce Wannier functions as the inverse Fourier transform of the Bloch waves,

$$w_s^n(x) = \frac{1}{\sqrt{N}} \sum_k e^{-ikx_s} \psi_k^n(x). \tag{2.10}$$

In the deep lattice limit, we therefore expect w_s^n to approach the single well eigenfunction ϕ_s^n, and to be localized around the given lattice site. Using that Bloch waves form a complete and orthogonal set, one can show that the Wannier functions do too. One may therefore expand any state in the localized Wannier functions. We use such an expansion in chapter 4.

2.4   Bogoliubov transformations

When calculating excitation spectra in chapter 6, we will need a special technique known as the Bogoliubov transformation. It is named after N. Bogoliubov, who applied it to the weakly interacting Bose gas to explain superfluidity in 1947 [14], as mentioned already in the introduction. It works equally well also for fermions, and is an essential ingredient in the famous BCS-theory of superconductivity developed a few years later [61–63]. A third application is the calculation of magnon dispersion relations in various quantum spin models [64]. This is how we will be using it. First, we go through the basic case with two different bosons using Bogoliubovs original approach. We then consider the dynamic matrix method, which is more practical for a larger number of boson operators [65, 66].

The starting point of Bogoliubov was the Hamiltonian [11],

$$H = \sum_k \frac{k^2}{2m} a_k^\dagger a_k + \frac{u}{2V} \sum_{k p_1 p_2} a_{p_1+k}^\dagger a_{p_2-k}^\dagger a_{p_1} a_{p_2}. \tag{2.11}$$

Assuming weak interactions and macroscopic occupation of the zero momentum state, terms in the interaction where less than two operators destroy or create particles in the $\mathbf{k} = 0$ mode are neglected. This gives quadratic Hamiltonian on the form [11]

$$H = E_0 + \frac{1}{2} \sum_{k \neq 0} \left\{ \left(\frac{k^2}{2m} + un \right) \left(a_k^\dagger a_k + a_{-k}^\dagger a_{-k} \right) + un \left(a_k^\dagger a_{-k}^\dagger + a_k a_{-k} \right) \right\}, \tag{2.12}$$

where n is the approximate density of particles. One should think of a_k and a_{-k} as completely independent operators. For convenience, we let $A_k = \left(k^2/2m + un \right)$ and $B_k = un$. The Hamiltonian can be diagonalized by the transformation [13]

$$a_k = u_k \alpha_k - v_k \alpha_{-k}^\dagger \tag{2.13}$$

$$a_{-k} = u_k \alpha_{-k} - v_k \alpha_k^\dagger, \tag{2.14}$$

where we can choose u_k and v_k to be real. We require the new operators α_k and $\alpha_k^\dagger$ to satisfy boson commutation relations, and this gives condition $u_k^2 - v_k^2 = 1$. Inserting the above transformation in the Hamiltonian (2.12), one can show that choosing [13]

$$u_k = \left[\frac{1}{2} \left(\frac{A_k}{\omega_k} + 1 \right) \right]^{1/2} \qquad v_k = \left[\frac{1}{2} \left(\frac{A_k}{\omega_k} - 1 \right) \right]^{1/2} \tag{2.15}$$

with

$$\omega_k = \sqrt{A_k^2 - B_k^2} \tag{2.16}$$

renders the Hamiltonian on the form of the non-interacting Bose gas

$$H = E_0 + \frac{1}{2} \sum_{k \neq 0} (\omega_k - A_k) + \sum_{k \neq 0} \omega_k \alpha_k^\dagger \alpha_k, \tag{2.17}$$

where we have used $\sum_k \alpha_k^\dagger \alpha_k = \sum_k \alpha_{-k}^\dagger \alpha_{-k}$.

Of special interest is the number of particles in excited states [13]. This is

$$N - N_0 = \sum_{k \neq 0} \langle a_k^\dagger a_k \rangle. \tag{2.18}$$

Inserting the Bogoliubov transformation gives

$$N - N_0 = \sum_k \langle (u_k \alpha_k^\dagger - v_k \alpha_{-k})(u_k \alpha_k - v_k \alpha_{-k}^\dagger) \rangle \tag{2.19}$$

$$= \sum_{k \neq 0} v_k^2 + \sum_{k \neq 0} (u_k^2 + v_k^2) \langle \alpha_k^\dagger \alpha_k \rangle, \tag{2.20}$$

where we have used that $\langle \alpha_k^\dagger \alpha_{-k}^\dagger \rangle = \langle \alpha_k \alpha_{-k} \rangle = 0$ since the Hamiltonian is diagonal in these operators. For the same reason, the expectation value $\langle \alpha_k^\dagger \alpha_k \rangle$ is simply the Bose-Einstein distribution $n_B(\omega_k)$. The first term in the above expression comes from boson commutation relations, and shows that with weak interactions, bosons find themselves in finite momentum states even at zero temperature.

In the above calculation, we skipped the derivation of the coefficients u_k and v_k. This requires some calculation, but is quite doable. If more than two different bosons are coupled, a more systematic approach would be an advantage. In the dynamic matrix method, the idea is to write the problem on a form where one can apply familiar matrix diagonalization by finding the eigenvalues and -vectors.

Consider a more general Hamiltonian [66]

$$H = \sum_{i,j=1}^n \left[\tau_{ij} a_i^\dagger a_j + \frac{1}{2} \left(\gamma_{ij} a_i^\dagger a_j^\dagger + \gamma_{ji}^* a_i a_j \right) \right], \tag{2.21}$$

where $\{a_i\}$ are n independent boson annihilation operators satisfying usual commutation relations, and τ_{ij} and γ_{ij} are matrices. The hermiticity of H gives $\tau_{ij} = \tau_{ji}^*$ and $\gamma_{ij} = \gamma_{ji}$. The Hamiltonian can be written as [66]

$$H = \frac{1}{2} \psi^\dagger M \psi - \frac{1}{2} \text{Tr}(\tau), \tag{2.22}$$

where $\psi^\dagger = (a_1^\dagger, ..., a_n^\dagger, a_1, ..., a_n) \equiv (a^\dagger, a^T)$, and M is the matrix

$$M = \begin{pmatrix} \tau & \gamma \\ \gamma^\dagger & \tau^T \end{pmatrix}. \tag{2.23}$$

The last term in (2.22) is due to the non-commutativity of creation and annihilation operators for the same boson species. To diagonalize the problem, introduce a new set of operators $\phi^\dagger = (\alpha^\dagger, \alpha^T)$ such that $\psi = T\phi$ for some matrix T. Inserted in the Hamiltonian, this gives a term $\phi^\dagger T^\dagger M T \phi$. Thus, we need properties [66]

- $\phi = T^{-1}\psi$ satisfies boson commutation relations

- $T^\dagger M T = D$, with diagonal matrix D

Going back to Bogoliubovs original calculation, the first requirement corresponds to $u^2 - v^2 = 1$, and the second to the intelligent choice of u and v that we made. The first requirement significantly complicates the problem, since otherwise, ordinary orthogonal diagonalization would have been sufficient.

We can write the transformation as

$$\begin{pmatrix} a \\ (a^\dagger)^T \end{pmatrix} = \begin{pmatrix} U_1 & V_1 \\ V_2 & U_2 \end{pmatrix} \begin{pmatrix} \alpha \\ (\alpha^\dagger)^T \end{pmatrix}. \tag{2.24}$$

Comparing the expressions for a and $a^\dagger$ gives $U_2 = U_1^*$ and $V_2 = V_1^*$ [65]. Expressed in term of the new bosons, the condition that ψ are also bosons becomes

$$[\psi_i, (\psi^\dagger)_j] = \sum_{kl} T_{ik}[\phi_k, \phi_l^\dagger](T^\dagger)_{lj} = J_{ij}, \tag{2.25}$$

where J is the matrix

$$J = \begin{pmatrix} 1 & 0 \\ 0 & -1 \end{pmatrix}. \tag{2.26}$$

If we assume the operators in ϕ are bosons, then $[\phi_k, \phi_l^\dagger] = J_{kl}$, and hence, we can write (2.25) on matrix form as $TJT^\dagger = J$, or equivalently $T^\dagger = JT^{-1}J$. The diagonalization requirement $T^\dagger MT = D$ then takes the form [65]

$$T^{-1}JMT = JD. \tag{2.27}$$

If we can find a set of eigenvectors diagonalizing MJ, we can therefore also diagonalize the physical problem. Whether this is actually possible still depends on the coefficients τ_{ij} and γ_{ij}, but we now have a systematic way of attacking the problem.

One can show [66] that the eigenvalues of the matrix $\tilde{M} = JM$ appear in pairs $\pm\omega_1,\ ...,\pm\omega_n$. The diagonal matrix can therefore be written as $D = \mathrm{diag}(\Omega, \Omega)$, with $\Omega = \mathrm{diag}(\omega_1, ..., \omega_n)$ consisting of all the positive eigenvalues. Inserting this back into (2.22) gives

$$H = \sum_{i=1}^{n} \omega_i \alpha_i^\dagger \alpha_i + \frac{1}{2}(\mathrm{Tr}\,\Omega - \mathrm{Tr}\,\tau). \tag{2.28}$$

In addition to the thermal excitation term, we obtain quantum corrections. One may now use this matrix method to re-derive the formula for the Hamiltonian of the weakly interacting Bose gas.

Finally, a note on terminology. The method we just discussed is called the dynamic matrix method. The reason is that the Heisenberg equation of motion for the boson operators becomes the Schrödinger-like [65]

$$i\frac{\mathrm{d}\psi}{\mathrm{d}t} = \tilde{M}\psi, \tag{2.29}$$

where $\tilde{M}$ is the matrix we use to find the physical eigenvalues of the problem.

Chapter 3

Cold atoms and spin-orbit coupling

3.1 Cold atom systems

Ever since the first experimental realization, atomic Bose-Einstein condensation has been an active research field for both theorists and experimentalists. The cooling of atomic gases down to nanokelvin temperatures has become standard, and is performed at multiple laboratories worldwide [20]. In this section, we aim at describing some of the theoretical and experimental concepts underlying the experimental realization of Bose-Einstein condensation. The books by Pitaevskii and Stringari [11] and Pethick and Smith [13] provide a more detailed introduction.

3.1.1 Internal states and pseudo-spin

Due to the concept of quantum statistics, whether the particles of a gas are identical or not is of fundamental importance. One might therefore expect novel features in a mixture of Bose-Einstein condensates. It could be a mixture of different isotopes or atoms [67], but more common is atoms in different hyperfine states.

To take a concrete example, consider ^{87}Rb, which is a popular isotope because of a fortunate suppression of inelastic collisions between atoms in two of the hyperfine states [21]. Since it is an alkali metal, it has 86 electrons in the inner shells, and an additional electron with spin described by a spin operator $\mathbf{I}$ with spin quantum number $I = 1/2$. The atom also has a nuclear spin $\mathbf{J}$ with spin quantum number $J = 3/2$ [13]. These spins can be combined to a total spin $\mathbf{F} = \mathbf{I} + \mathbf{J}$. According to the rules for addition of spin variables [59], $\mathbf{F}$ is a new spin variable with spin quantum number $3/2 \pm 1/2$. Since the magnetic quantum number m_F can take the values $-F, -F + 1, ..., F$, there are $3 + 5 = 8$ possible internal states. Due to interaction between the electron and nuclear spins, there is an energy difference between the $F = 1$ and $F = 2$ states. In presence of a magnetic field, the degeneracy with respect to magnetic quantum number is lifted as well. The internal states of the atom are typically shown in a level diagram, as in figure 3.1a.

Experimentally, one can choose two of the internal states in the level diagram and make sure that the occupation of other states is negligible within the trapping potential. The atoms can then be in any superposition of the two hyperfine states. This generates a two-dimensional Hilbert space, which is isomorphic to a spin-1/2 system. This justifies labelling the hyperfine states as spin states $|\uparrow\rangle$ and $|\downarrow\rangle$. The spin structure of any operator acting a single particle state can then be expressed in terms of Pauli matrices and the identity, giving a description completely analogous to electrons with an intrinsic spin.
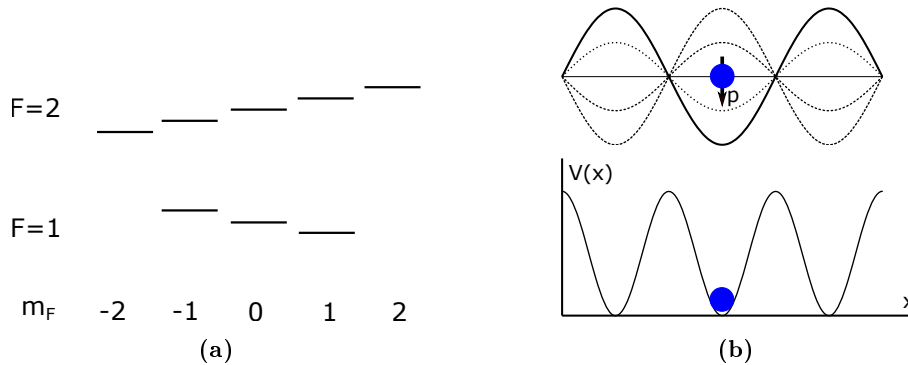
Figure 3.1: (a) Figure adapted from Ref. [68]. Level diagram for energy of internal spin states of an alkali atom with nuclear spin $3/2$ in a magnetic field. Interaction between the electron and nuclear spins gives an energy difference between the $F = 1$ and $F = 2$ states, while the presence of the magnetic field lifts the degeneracy with respect to magnetic quantum number m_F. In (b), an oscillating electric field induces a dipole moment, which oscillates in or out of phase with the electric field depending on the driving frequency. In both cases, the dipole interaction with the electric field causes a periodic potential.

3.1.2   Cooling

A typical phase diagram describing states of matter shows three different phases [11]. At high temperature, the system is in a liquid or gaseous phase, but at sufficiently low temperature, molecules start to form, and the system enters a solid phase. To achieve Bose-Einstein condensation in atomic gases, this must be prevented [21]. Starting from a gas, the formation of molecules cannot happen through processes involving only two particles, since the formation of a bound state leaves an excess potential energy which due to momentum conservation cannot be compensated for by an increase in kinetic energy [69]. For three-body processes, two particles can enter a bound state, and the excess energy can be transferred to the relative motion between the newly formed molecule and the third particle participating in the process. The rate at which such processes happen is proportional to ρ^3, where ρ is the density of the gas. This suggests that by using a sufficiently dilute gas, molecule formation is so slow that the atomic gas is pertained sufficiently long to reach kinetic equilibrium [20]. This can happen through the more frequent two-body processes. Bose-Einstein condensation can therefore occur in the time-window after thermalization of the gas and before a significant fraction of the condensate is lost due to molecule formation.

A typical experimental protocol for achieving Bose-Einstein condensation therefore starts with vaporization. To cool the gas down to nK temperatures, most experiments use multiple cooling techniques. Typically, laser cooling is applied applied first, which may include Zeeman slowing, Doppler cooling, and Sisyphus cooling [13, 20, 70]. For the final cooling step down to Bose-Einstein condensation temperatures, most experiments use evaporative cooling [20]. By letting high energy particles escape, followed by kinetic re-equilibration, the number of low energy particles is increased [13, 68]. Recently, Bose-Einstein condensation has also been reached with laser-cooling techniques only [71].

3.1.3   Trapping and optical lattices

To prevent interaction with the surroundings, the atoms need to be trapped. Several techniques exist, based on application of lasers and magnetic fields.

In magnetic traps [13], the idea is to use the magnetic field dependence of the hyperfine state splitting. If a magnetic field gradient is present, this generates a force which can be used to trap particles in regions with a local minimum in the magnetic field strength $B = |\mathbf{B}|$. Atoms in other hyperfine states will be repelled from such regions. These cannot be trapped, since a

local maximum in B cannot be achieved in free space. This follows from the Maxwell equations by considering $\nabla^2 B^2$ [11]. Since in any case, the trapping potential depends on boson species, magnetic traps are typically not optimal for mixtures of bosons in different hyperfine states.

Optical traps do not have this disadvantage. The idea is to use an electric field $\mathbf{E}(\mathbf{r})$ to induce a dipole moment $\mathbf{p}$, which again interacts with the electric field through the dipole interaction $H_{\mathrm{dip}} = -\mathbf{p} \cdot \mathbf{E}$. In the quantum mechanical problem, one can use second order perturbation theory with H_{dip} as the perturbation to calculate corrections to the energy of the hyperfine states [11, 13]. For our purposes, the classical driven harmonic oscillator suffices to explain the qualitative features. The amplitude of the oscillation depends on driving frequency ω, and is proportional to the electric field. The dipole potential therefore becomes [24]

$$V_{\mathrm{dip}} = -\langle \mathbf{p}(t) \cdot \mathbf{E}(\mathbf{r}, t) \rangle \propto \alpha(\omega) \left\langle |\mathbf{E}(\mathbf{r}, t)|^2 \right\rangle, \tag{3.1}$$

where the brackets denote time average. Depending on whether the system is driven below or above the resonance frequency, the dipole moment oscillates in or out of phase with the electric field, and the atoms prefer to sit at spots with large or small time-averaged electric field. Such regions are naturally created by laser beams. With a standard Gaussian profile [72], atoms experience a harmonic trapping potential around the focus point for sub-resonant driving.

The creation of an optical lattice is based on the above principle. Two counter-propagating laser beams form a standing wave, and time average gives the desired periodic potential, as illustrated in figure 3.1b. If we let k_L be the wavevector of the lasers and assume plane waves propagating in the positive and negative x-directions, the resulting potential is [24]

$$V(\mathbf{r}) = V_0 \sin^2 k_L x, \tag{3.2}$$

where the lattice depth V_0 is proportional to laser intensity. Hence, the periodicity of the potential is $\pi/k_L = \lambda_L/2$.

By considering various laser geometries, it is possible to generate a plethora of lattices, examples being triangular [73], hexagonal [74], and kagome [75] lattices. Simpler, but of special importance to us, is the two-dimensional square lattice. This can be generated by adding a second set of counter-propagating lasers in the y-direction. By choosing the polarization differently, the two sets of lasers do not interfere. With equal intensities, the lattice potential then becomes

$$V(\mathbf{r}) = V_0 \left(\sin^2 k_L x + \sin^2 k_L y \right). \tag{3.3}$$

The minima of this potential form a square lattice. By adding strong confinement in the z-direction, a two-dimensional gas of atoms in an optical lattice can been produced. This is the focus of the investigations in this thesis.

An alternate way of avoiding interference is to use lasers with somewhat different frequencies [69]. Interference terms in the dipole potential are then washed away by the resulting beat phenomenon. This is particularly useful when one wants to avoid interference between more than two lasers, since there are only two independent polarizations available.

3.1.4 Interaction and Feshbach resonances

We require the atoms of the Bose gas to be isolated from any external reservoir. Interactions therefore play an important role in thermalization of the gas, as mentioned in section 3.1.2. In this section, we discuss the characteristics of interaction in cold atom systems.

Although atoms consist of several particles – a nucleus and electrons – treating the atoms as point particles, we may describe their interaction with a potential $V(\mathbf{r})$, where $\mathbf{r}$ is the relative coordinate. The interaction is typically strongly repulsive at small distances, while dipole-dipole interaction gives a tail $V(r) \propto -1/r^6$ at large distances [59].

In a dilute gas, particles are usually far apart and weakly interacting. The effect of interactions on the Bose-Einstein condensate is therefore dominated by the rare event that particles get close. This is described by scattering theory. At low temperatures, the scattering properties of the system as described by the differential scattering cross section are determined by a single parameter known as the scattering length a [13]. Qualitatively, the particle wave lengths are too large to resolve details of the interaction potential [76]. Due to this insensitivity, the interaction can be replaced by an effective interaction on a simpler form, $V(\mathbf{r}) \rightarrow V_{\text{eff}}(\mathbf{r})$ [13]. A popular choice is the delta function potential

$$V_{\text{eff}}(\mathbf{r}) = U_0 \delta(\mathbf{r}), \tag{3.4}$$

although strictly speaking, it must be interpreted as a Fermi pseudo-potential to produce the correct scattering properties [69, 77]. Calculation of the scattering length from the pseudo-potential gives connection

$$U_0 = \frac{4\pi\hbar^2 a}{m} \tag{3.5}$$

between the true and the effective potential. This is a direct relation between the scattering length and the interaction strength of the cold bosons in the system.

An important concept for the ultracold atomic gas is Feshbach resonances. By increasing the depth of an attractive potential, whenever a new bound bound state enters the system, the scattering length diverges and changes sign according to [13]

$$a \propto \frac{C}{E - E_{bs}}, \tag{3.6}$$

where E is the energy of the particles, and E_{bs} is the energy of the bound state. Possible bound states also include states where the particles find themselves in different hyperfine states than they were originally. For such states, the difference $E - E_{bs}$ can be tuned with a magnetic field. Hence, the scattering length, and by extension the effective interaction, can be tuned with a magnetic field, which is easily controllable.

3.2 Spin-orbit coupling

In this section, we first discuss the basic properties of spin-orbit coupling in electronic systems, and then outline how a synthetic spin-orbit coupling can be realized in two-component ultracold atom systems.

3.2.1 Electronic Spin-Orbit Coupling

Spin-orbit coupling is a coupling between the spin and the momentum of a particle. For electrons, it arises from the Dirac equation as a relativistic correction to the Schrödinger equation for a particle moving in an electrostatic potential V [27],

$$H_{\text{SOC}} = -\frac{e}{2m_e^2 c^2} \mathbf{S} \cdot \mathbf{p} \times \nabla V, \tag{3.7}$$

where $\mathbf{S}$ is the spin operator, m_e the electron mass, and e the elementary charge. For the hydrogen atom with spherically symmetric Coulomb potential $V(r)$, this gives a contribution to the fine structure of the atom [28]. Using that ∇V is radial and that the orbital angular momentum is $\mathbf{L} = \mathbf{r} \times \mathbf{p}$, the relativistic correction becomes

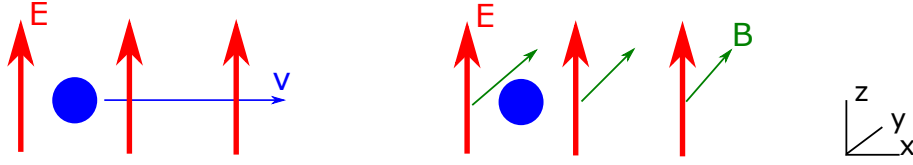$$H_{\text{SOC}} = \lambda_{SO} \mathbf{S} \cdot \mathbf{L}, \tag{3.8}$$

Figure 3.2: Interpretation of spin-orbit coupling as an effective magnetic field. If an electron is moving with velocity **v** in an electric field **E** (left panel), there is an effective magnetic field $\mathbf{B}_{\text{eff}} = -\mathbf{v} \times \mathbf{E}/c^2$ in the rest frame of the electron (right panel). Figure adapted from Ref. [22].

with some coupling strength λ_{SO}. Spin-orbit coupling therefore becomes a coupling between the spin and orbital angular momentum of the electron. This explains the the name, although the concept is really more general. Whenever an electron moves in an electric field, there is coupling between the spin and momentum of the particle.

A different way to view spin-orbit coupling is through an effective magnetic field in the rest-frame of the electron. Consider, as in figure 3.2, an electron moving with velocity **v** perpendicular to an electric field **E**. In the reference frame where the electron is at rest, Lorentz transformation of the electric field gives a magnetic field

$$\mathbf{B}_{\text{eff}} = -\mathbf{v} \times \mathbf{E}/c^2 \tag{3.9}$$

to lowest order in v/c. In this frame, there is a Zeeman interaction $H \propto \mathbf{S} \cdot \mathbf{B}_{\text{eff}}$. Hence, there must be a contribution

$$H_{\text{SOC}} \propto \mathbf{S} \cdot \mathbf{p} \times \mathbf{E} \tag{3.10}$$

also in the original frame. Working out the details, the prefactors agree with the prefactors in (3.7).

We now specialize to the case of atoms moving in two dimensions, which we take to be the xy-plane. This situation in realized for instance at interfaces between solid-state materials [26]. With electric field **E**, the spin-orbit coupling is proportional to

$$\vec{\sigma} \cdot \mathbf{p} \times \mathbf{E} = \sigma_x(E_z p_y - E_y p_z) - \sigma_y(E_z p_x - E_x p_z) + \sigma_z(E_y p_x - E_x p_y). \tag{3.11}$$

Since $\langle p_z \rangle = 0$ for the two-dimensional electron gas, we get

$$H_{\text{SOC}} \propto E_z(\sigma_x p_y - \sigma_y p_x) + \sigma_z(E_y p_x - E_x p_y). \tag{3.12}$$

This shows that spin-orbit coupling on the form $\mathbf{S} \cdot \mathbf{p} \times \mathbf{E}$ can generate any linear coupling between the momenta and the z-component of the spin. The second term couples the x- and y-components of the spin in a particular way, namely as

$$H_R = \kappa_R(\sigma_x p_y - \sigma_y p_x) \tag{3.13}$$

This is known as Rashba spin-orbit coupling, and was used to explain spin resonance in two-dimensional semiconductors by Bychov and Rashba in 1984 [26, 32]. The most general linear coupling between electron momentum and the x- and y-components of the spin is on the form

$$H_{\text{SOC}} = \sum_{l\delta} \beta_{l\delta} \sigma_l p_\delta, \tag{3.14}$$

with spin-orbit coupling matrix $\beta_{\gamma\delta}$ [78]. One may therefore ask whether other forms of $\beta_{l\delta}$ could be of relevance as well. As realized by Dresselhaus [27, 29], there may be coupling of higher order in momentum on the form
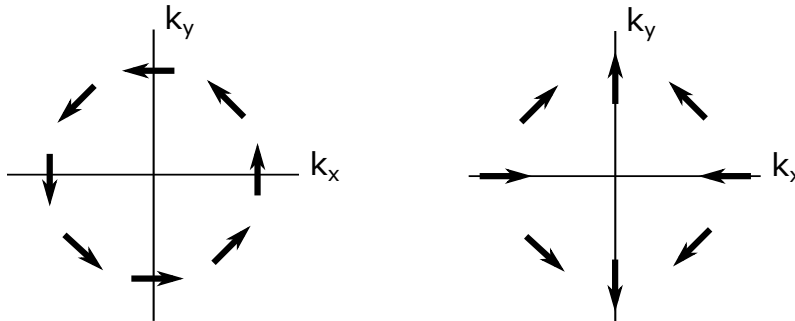
Figure 3.3: Effective magnetic fields $\mathbf{\Omega}(\mathbf{k})$ as function of momentum $\mathbf{k}$. Left panel: Rashba SOC on the form $\sigma_x k_y - \sigma_y k_x$. Right panel: Dresselhaus SOC on the form $\sigma_x k_x - \sigma_y k_y$.

$$H_{\mathrm{D}}^{\mathrm{3D}} = \gamma_c k_z^2 (-\sigma_x k_x + \sigma_y k_y) \tag{3.15}$$

in zincblende structures. When the system is subject to strong confinement in the z-direction, it can written in the form (3.14), since upon replacement of k_z^2 with the expectation value, the uncertainty principle gives an appreciable uncertainty $\langle k_z^2 \rangle$. The result is therefore a so called Dresselhaus spin-orbit coupling on the form

$$H_{\mathrm{D}} = \kappa_D (\sigma_x k_x - \sigma_y k_y). \tag{3.16}$$

Earlier, we discussed the interpretation of SOC as a momentum-dependent magnetic field, $H_{\mathrm{SOC}} = -\mathbf{S} \cdot \mathbf{B}(\mathbf{k})$. Regardless of physical origin, this gives a nice way of visualizing the two types of spin-orbit coupling. In figure 3.3, we plot the effective magnetic fields as function of momentum vector $\mathbf{k}$.

The Rashba and Dresselhaus spin-orbit couplings can be represented in different ways. For the forms above, the Rashba spin-orbit coupling comes as off-diagonal elements in the SOC-matrix, while Dresselhaus SOC is on the diagonal. Considering for instance the Dresselhaus SOC, we can however obtain the equivalent form $H_{\mathrm{D}} \propto \sigma_x k_y + \sigma_y k_x$ by making a $\pi/4$ rotation. Similarly, the Rashba SOC can be represented by $H_{\mathrm{R}} \propto \sigma_x k_x + \sigma_y k_y$. Considering for a moment the atomic gas, the different representations are again equivalent, but since spin represents hyperfine states, spin-variables are not affected by a real space rotation. To show equivalence of the above forms, one therefore has to rotate with angle $\pi/2$ instead of $\pi/4$.

A case especially interesting for applications is when the strengths of the Rashba and Dresselhaus SOC are equal, giving rise to a so called persistent spin helix (PSH). Experimentally, this has been realized in quantum well structures by tuning the confinement in z-direction, and hence $\langle k_z^2 \rangle$ in equation (3.15) [79]. Since at the PSH point, the spiral structure is particularly stable [26], it has been proposed to make a spin field-effect transistor based on SOC at the PSH point [80].

Spin-orbit coupling is a relativistic effect, so extreme conditions are required to give observable effects [22]. Particles then have to move at relativistic speeds or be subject to strong electric fields, as in many condensed matter systems. An example is topological insulators [35], where spin-orbit coupling drastically affects transport properties. As usual in condensed matter systems, the parameter regime is largely fixed by the properties of the material one is studying, and being a relativistic effect, spin-orbit coupling is typically small [81]. Contrary to this, the synthetic spin-orbit coupling we consider next can be made large, and shows high flexibility.

3.2.2 Synthetic spin-orbit coupling

We have seen that for electrons, spin-orbit coupling can be caused by an electric field. In cold atom systems, the atoms are neutral and spin corresponds to hyperfine states. Any coupling between

momentum and spin must therefore have a fundamentally different origin.

The first realization of a spin-orbit coupled BEC came in 2011, and used a Raman transition scheme [44]. Nowadays, the use of Raman lasers for this purpose has become standard, and has been used in numerous experiments all over the globe [46, 51, 52, 82–85]. An alternate way to generate SOC is to drive the system with some time-periodic perturbation which can cause spin-orbit coupling in a time-averaged Floquet Hamiltonian [86] for the system [87–91]. Recently, this was implemented using pulsed magnetic field gradients [92].

To explain the more common Raman transition scheme, one may consider two counter-propagating lasers with frequencies ω_A and $\omega_B = \omega_A - \Delta\omega$, and wave vectors $\mathbf{k}_A$ and $\mathbf{k}_B$ [22, 93, 94]. Assume we are interested in two hyperfine states of the atom with energies ω_1 and ω_2. The two lasers couple each of these states to an excited state with energy ω_E. By absorption of a photon from laser beam A and stimulated re-emission into laser beam B, the Raman lasers cause a transition from hyperfine state 1 to hyperfine state 2. In addition, such a transition transfers momentum $\mathbf{k}_A - \mathbf{k}_B$ to the atom. If $\Delta\omega$ is close to $\omega_2 - \omega_1$, the transition is resonant. Since the laser frequency difference as observed by the atom depends on the atomic velocity due to the Doppler effect, the transition rate is coupled to momentum.

Utilizing several lasers and coupling between up to four of the hyperfine states of the atom, one can in principle produce any linear combination of Dresselhaus and Rashba spin-orbit coupling [22]. Theoretical proposals have existed for some years, but the experimental realization turned out to be a much more challenging than then simple one-dimensional SOC equivalent to equal linear combination of Rashba and Dresselhaus SOC. For bosons, it was achieved in 2016 by a group in Shanghai [55, 56], following the realization in atomic Fermi gases earlier the same year [57, 58].

3.3   Continuum spin-orbit coupled Bose gas

Consider the spin-orbit coupled non-interacting Bose gas in two dimensions. With an additional magnetic field causing Zeeman splitting $2h$ between the two relevant components of the gas, the system is described by Hamiltonian

$$H = \frac{\mathbf{p}^2}{2m} - h\sigma_z + \eta\sigma_x p_y + \kappa\sigma_y p_x. \tag{3.17}$$

The effect of spin-orbit coupling on the dispersion relation is especially easy to understand when there is no Zeeman splitting. The spin-orbit coupling gives a contribution to particle energy linear in momentum, where the sign depends on whether the spin is aligned parallel or anti-parallel to the effective magnetic field. The dispersion relation is therefore shifted in momentum space, and the ground state is no longer at $\mathbf{k} = 0$.

Since the Hamiltonian consists exclusively of momentum component operators, we can factor out the spatial dependence of the energy eigenvectors and write

$$\psi_k(\mathbf{r}) = e^{i\mathbf{k}\cdot\mathbf{r}}\phi, \tag{3.18}$$

where ϕ is a position independent two-component column vector. The resulting eigenvalue problem

$$\begin{pmatrix} \frac{k^2}{2m} - h & \eta k_y - i\kappa k_x \\ \eta k_y + i\kappa k_x & \frac{k^2}{2m} + h \end{pmatrix} \phi = E_k\phi \tag{3.19}$$

gives continuum dispersion relation

$$E_{k\pm} = \frac{k^2}{2m} \pm \sqrt{h^2 + \kappa^2 k_x^2 + \eta^2 k_y^2}. \tag{3.20}$$

This dispersion relation is plotted in figure 3.4. For Rashba SOC, where $\eta = -\kappa$, the dispersion relation is isotropic with a continuously degenerate minimum, as in 3.4a. As shown in 3.4b, this large
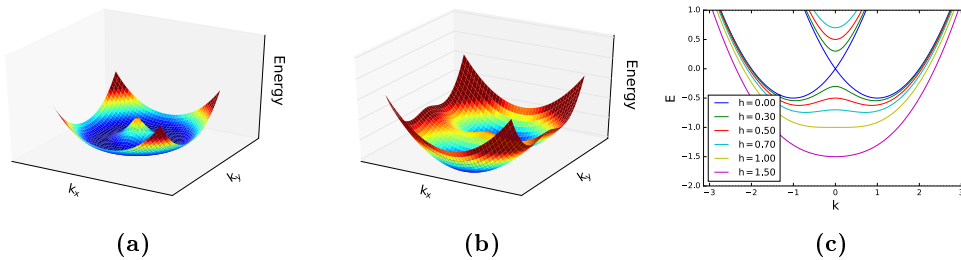
(a)   **(b)**   **(c)**

Figure 3.4: Dispersion relation as function of quasimomentum. For the Rashba SOC in (a), there is a circularly symmetric continuously degenerate minimum. This degeneracy is lifted for $\kappa \neq \eta$ in (b), corresponding to a general linear combination of Rashba and Dresselahaus SOC, for which there are two minima at finite $\mathbf{k}$. In (c), we plot the dispersion relation for Rashba SOC as function of $k = |\mathbf{k}|$ with various Zeeman field strengths h at $m = \kappa = 1$. For sufficiently large h, the minima at finite $\mathbf{k}$ vanish.

degeneracy is lifted when $|\kappa| \neq |\eta|$, and the dispersion relation instead has two isolated minima. The large ground state degeneracy for pure Rashba SOC makes Bose-Einstein condensation harder since the effective dimension of the density of states is reduced by one [95]. For two-dimensional systems, as discussed in chapter 2, Bose-Einstein condensation at finite temperature in minima with quadratic dispersion is already not possible. The continuously degenerate minimum is still an important qualitative feature, since the effective dimensionality amongst others is important for the amount of fluctuations in the system. For three-dimensional systems, finite-temperature Bose-Einstein condensation of non-interacting particles becomes impossible because of the perfect Rashba SOC [22, 96]. Interactions may however partially lift the massive degeneracy.

In figure 3.4c, we plot the dispersion relation for Rashba SOC with mass $m = 1$ and spin-orbit coupling $\kappa^2 = \eta^2 = 1$. The minimum at finite $\mathbf{k}$ vanishes for sufficiently strong Zeeman field h. The condition for this can be determined from $\partial E_{k-}/\partial k = 0$, which gives extrema at $k = 0$ and

$$k^2 = \kappa^2 m^2 - \frac{h^2}{\kappa^2}. \tag{3.21}$$

When the second term on the right hand side becomes larger than the first, there is no solution at finite k. Thus, the condition to get a minimum at finite $\mathbf{k}$ is $|h| < \kappa^2 m$. We show in chapter 5 that something analogous happens when the cold atoms reside on an optical lattice.

The location of the minima at finite quasi-momentum can be tested experimentally with a time-of-flight (TOF) measurement. When switching off the confinement and Raman lasers, spin and quasimomentum are projected down on momentum and spin eigenstates. After a free expansion, the momentum distribution is mapped to a real space distribution, which can be measured for instance by absorption imaging, as in [44]. In figure 1 there, the clouds of oppositely polarized spins come closer upon increasing the Zeeman splitting, before merging at a critical value. In Ref. [45], the entire dispersion relation is measured with spin-injection spectroscopy.

In the above mentioned paper [44], one also measured the effect of a Zeeman term on a parameter quantifying phase separation. Although the Zeeman term always favours phase separation, the transition point may come only at a critical Zeeman splitting due to spin-dependent interactions and spin-orbit coupling. The interactions can also cause phase separation. Without spin-orbit coupling, this can be addressed with the Gross-Pitaevskii equation for a homogeneous condensate. One may show that the conditions for stability of the mixed condensate become [11, 13]

$$u_{\uparrow\uparrow} > 0 \qquad u_{\downarrow\downarrow} > 0 \qquad u_{\uparrow\uparrow} u_{\downarrow\downarrow} > u_{\uparrow\downarrow}^2. \tag{3.22}$$

The physical interpretation is quite straightforward. If either of the intracomponent interactions are negative, the attraction causes a collapse, and can even lead to a phenomenon coined a "bosen-

ova" [97, 98]. The last condition expresses that if intercomponent repulsion is stronger than the intracomponent repulsion, phase separation is energetically favourable.

One may now ask how spin-orbit coupling affects the stability of the mixture. This is the subject of chapter 5.

Chapter 4

Bose-Hubbard models

In the previous chapter, we discussed the physics of spin-orbit coupled ultracold atoms. In this chapter, our aim is to go from the description of this in first quantization to a many-body description in second quantization. Applying the tight-binding approximation, we derive the Bose-Hubbard model including spin-orbit coupling. Finally, we discuss some properties of the superfluid to Mott insulator (SF-MI) quantum phase transition in the Bose-Hubbard model with and without spin-orbit coupling.

4.1 Bose-Hubbard model derivations

In first quantization, an N-particle state can be represented as

$$\Psi_N(\mathbf{r}_1, ..., \mathbf{r}_N) = \prod_{i=1}^{N} \phi_i(\mathbf{r}_i), \tag{4.1}$$

where, due to the two internal spin states, the single particle state ϕ_i is characterized by a two-component column vector,

$$\phi_i(\mathbf{r}_i) = \begin{pmatrix} \phi_{i\uparrow}(\mathbf{r}_i) \\ \phi_{i\downarrow}(\mathbf{r}_i) \end{pmatrix}. \tag{4.2}$$

The Hamiltonian describing the non-interacting spin-orbit coupled gas of N cold atoms of mass m in an external potential $V(\mathbf{r})$ is then

$$h = \sum_{i=1}^{N} \left(\frac{\mathbf{p}_i^2}{2m} + V(\mathbf{r}) + \sum_{l\delta} \beta_{l\delta} \sigma_i^l p_i^\delta \right). \tag{4.3}$$

Here, $l, \delta \in \{x, y\}$, and σ_i^l is Pauli matrix l acting on the spin space of particle i. Similarly, p_i^δ is momentum component δ of the same particle. The matrix $\beta_{l\delta}$ was introduced in the previous chapter, and quantifies the form and strength of the SOC. The external potential $V(\mathbf{r})$ includes the square optical lattice potential discussed in the previous chapter,

$$V(\mathbf{r}) = V_0 \left(\sin^2 k_L x + \sin^2 k_L y \right). \tag{4.4}$$

There are two energy scales associated with this lattice. In addition to the lattice depth V_0, the recoil energy $E_R = k_L^2/2m$ is a typical kinetic energy for particles on the lattice. In experiments, there is typically also a slowly varying trapping potential confining atoms within some finite region. This potential may have significant effects on the system [24], but for simplicity, we consider an infinite system without such trapping potentials.

In second quantization, interaction is introduced through the term

$$H_u = \sum_{\sigma\sigma'} \int \mathrm{d}\mathbf{r} \, \mathrm{d}\mathbf{r}' \, \Psi_\sigma^\dagger(\mathbf{r})\Psi_{\sigma'}^\dagger(\mathbf{r}')V_{\sigma\sigma'}(\mathbf{r}-\mathbf{r}')\Psi_{\sigma'}(\mathbf{r}')\Psi_\sigma(\mathbf{r}), \tag{4.5}$$

where $\Psi_\sigma^\dagger(\mathbf{r})$ is the creation operator for a particle of species σ at position $\mathbf{r}$, and $V_{\sigma\sigma'}(\mathbf{r}-\mathbf{r}')$ is a component dependent two-particle potential. Using effective contact potential

$$V_{\sigma\sigma'}(\mathbf{r}-\mathbf{r}') = \frac{1}{2}g_{\sigma\sigma'}\delta(\mathbf{r}-\mathbf{r}') \tag{4.6}$$

generalized to component-dependent interaction $g_{\sigma\sigma'}$ [99], we get

$$H_u = \frac{1}{2}\sum_{\sigma\sigma'} g_{\sigma\sigma'} \int \mathrm{d}\mathbf{r} \, \Psi_\sigma^\dagger(\mathbf{r})\Psi_{\sigma'}^\dagger(\mathbf{r})\Psi_{\sigma'}(\mathbf{r})\Psi_\sigma(\mathbf{r}). \tag{4.7}$$

The full Hamiltonian in second quantization is now

$$\begin{aligned}
H = \sum_{\sigma\sigma'} \int \mathrm{d}\mathbf{r} \, \Psi_\sigma^\dagger(\mathbf{r})&\left\{ \delta_{\sigma\sigma'}\left[\frac{\mathbf{p}^2}{2m}+V(\mathbf{r})\right] + \sum_{l\delta} \beta_{l\delta}(\sigma_l)^{\sigma\sigma'} p_\delta \right\}\Psi_{\sigma'}(\mathbf{r}) \\
&+ \frac{1}{2}\sum_{\sigma\sigma'} g_{\sigma\sigma'} \int \mathrm{d}\mathbf{r} \, \Psi_\sigma^\dagger(\mathbf{r})\Psi_{\sigma'}^\dagger(\mathbf{r})\Psi_{\sigma'}(\mathbf{r})\Psi_\sigma(\mathbf{r}).
\end{aligned} \tag{4.8}$$

Below, we provide two derivations of the Bose-Hubbard model for spin-orbit coupled systems in the tight-binding approximation, corresponding to $V_0 \gg E_R$. In this limit, both give the same answer. The first is based on naive replacement of derivatives of the real space field operator $\Psi(\mathbf{r})$ with discrete lattice site operators. Although simple and intuitive, it fails to connect the parameters in the resulting Bose-Hubbard model with the original lattice parameters. More rigorous is Wannier state approach.

4.1.1   Naive discretization

We aim at replacing the field operators in the above second quantized Hamiltonian with lattice site creation operators $\psi_i^\dagger = (a_{i\uparrow}^\dagger, a_{i\downarrow}^\dagger)$ and $\psi_i = (a_{i\uparrow}, a_{i\downarrow})^T$. The motivation for this is that in the tight-binding approximation, the regions between lattice site minima are classically forbidden, and hence, particles sit close to the lattice site. We express the integral as a discrete sum and replace the derivatives in the momentum operator according to [100]

$$\partial_\delta \Psi(\mathbf{r}) = \frac{1}{2}(\psi_{i+\delta} - \psi_{i-\delta}) \tag{4.9}$$

$$\partial_\delta^2 \Psi(\mathbf{r}) = \psi_{i+\delta} + \psi_{i-\delta} - 2\psi_i, \tag{4.10}$$

where we have used the middle point expression for the first derivative to ensure hermiticity in the spin-orbit coupling term. Inserting this in (4.8), terms on the form $\sum_i \psi_i^\dagger \psi_i$ do not interest us since they are merely a renormalization of the chemical potential. Collecting the contributions from the kinetic, spin-orbit coupling, and interaction terms, we get

$$H = -\frac{1}{2ma^2}\sum_{i,\delta}\psi_i^\dagger(\psi_{i+\delta}+\psi_{i-\delta}) - i\sum_{l\delta}\sum_i \frac{\beta_{l\delta}}{2a}\psi_i^\dagger \sigma^l(\psi_{i+\delta}-\psi_{i-\delta}) + \frac{1}{2}\sum_{\sigma\sigma'}\sum_i g_{\sigma\sigma'}\psi_{i\sigma}^\dagger\psi_{i\sigma'}^\dagger\psi_{i\sigma'}\psi_{i\sigma}. \tag{4.11}$$

Letting $1/2ma^2 \to t$, $\beta_{l\delta}/2a \to \beta_{l\delta}$ and $g_{\sigma\sigma'} \to u_{\sigma\sigma'}$, we can write this as

$$H = \sum_{i,\delta} \left\{ -t\, \psi_i^\dagger \psi_{i+\delta} - i\psi_i^\dagger \left(\sum_l \beta_{l\delta} \sigma_l \right) \psi_{i+\delta} + \text{h.c.} \right\} + \frac{1}{2} \sum_{\sigma\sigma'} \sum_i u_{\sigma\sigma'} a_{i\sigma}^\dagger a_{i\sigma'}^\dagger a_{i\sigma'} a_{i\sigma}. \tag{4.12}$$

For $\beta_{l\delta} = 0$ and $u_{\sigma\sigma'} = u\delta_{\sigma\sigma'}$, this is nothing but the famous Bose-Hubbard model. Here, we have generalized it to a spinor condensate with spin-orbit coupling and spin-dependent interaction.

4.1.2 Wannier function derivation

In this section, we provide a more formal derivation. Instead of using some unspecified localized operators, we use the Wannier functions of the non-interacting problem without spin-orbit coupling, as discussed in section 2.3. Since these form a complete and orthogonal set, one may expand the position creation and annihilation operators in the Wannier basis,

$$\Psi_\sigma(\mathbf{r}) = \sum_i w_\sigma(\mathbf{r} - \mathbf{r}_i)\, a_{i\sigma}, \tag{4.13}$$

where $a_{i\sigma}^\dagger$ creates a particle of species σ in the lowest band Wannier state localized around $\mathbf{r}_i$. Since the atoms are cold, we have omitted the higher band terms and suppressed the band index n.

Inserting the Wannier function expansion in the kinetic and external potential terms of the Hamiltonian (4.8) gives [69]

$$H_{\text{kin}} + \hat{V}_{\text{ext}} = \sum_{ij} \sum_\sigma a_{i\sigma}^\dagger a_{j\sigma} \int d\mathbf{r}\, w_{i\sigma}^*(\mathbf{r}) \left(\frac{\mathbf{p}^2}{2m_\sigma} + V_\sigma(\mathbf{r}) \right) w_{j\sigma}(\mathbf{r}). \tag{4.14}$$

In the limit $V_0/E_R \to \infty$, we may use the harmonic approximation for the potential, and this gives trapping frequency

$$\omega/E_R = 2\sqrt{V_0/E_R}. \tag{4.15}$$

We may then approximate the Wannier functions with the Gaussian ground state of the harmonic potential, which is exponentially decaying. The Wannier functions are localized around lattice sites in the deep lattice limit, and hence, the overlap between the Wannier functions $w_{i\sigma}(\mathbf{r})$ and $w_{j\sigma}(\mathbf{r})$ decreases rapidly with distance $|\mathbf{r}_i - \mathbf{r}_j|$. Terms with $i = j$ in (4.1.2) simply renormalize the chemical potential. In order to get non-trivial dynamics, we therefore include terms where i and j are nearest neighbours, but neglect all other terms. With spin-independent mass and external potential, the Wannier functions are spin-independent, and we can write the coupling between nearest neighbours as

$$t = -\int d\mathbf{r}\, w^*(\mathbf{r} - \mathbf{r}_i) \left(\frac{\mathbf{p}^2}{2m} + V(\mathbf{r}) \right) w(\mathbf{r} - \mathbf{r}_{i+\delta}). \tag{4.16}$$

Since the Wannier functions are Gaussian, the overlap between two neighbouring lattice sites is exponentially suppressed in $\sqrt{V_0/E_R}$ [101, 102].

For the spin-orbit coupling term, one obtains

$$H_{\text{SOC}} = -i \sum_{l\delta} \beta_{l\delta} \sum_{ij} \sum_{\sigma\sigma'} \left[\int d\mathbf{r}\, w_\sigma^*(\mathbf{r} - \mathbf{r}_i) \partial_\delta w_{\sigma'}(\mathbf{r} - \mathbf{r}_j) \right] b_{i\sigma}^\dagger (\sigma_l)^{\sigma\sigma'} b_{j\sigma'}. \tag{4.17}$$

Mirror symmetry dictates that the term from $i = j$ gives zero, and that there is a contribution for nearest neighbours only when $j = i \pm \delta$. Neglecting all other terms and noticing that $i \leftrightarrow j$ gives a relative minus sign, we can write the Hamiltonian as

$$H_{\mathrm{SOC}} = -i \sum_{i,\delta} \psi_i^\dagger \left(\sigma_l \tilde{\beta}_{l\delta} \right) \psi_{i+\delta} + \mathrm{h.c.} \tag{4.18}$$

in terms of a rescaled

$$\tilde{\beta}_{l\delta} = \beta_{l\delta} \left[\int \mathrm{d}\mathbf{r} \; w^*(\mathbf{r} - \mathbf{r}_i) \partial_\delta w(\mathbf{r} - \mathbf{r}_{i+\delta}) \right], \tag{4.19}$$

where we have omitted the spin index of the Wannier functions because they are spin independent. This can easily be generalized.

For the interaction term, the Hamiltonian becomes

$$H_u = \frac{1}{2} \sum_{\sigma\sigma'} \sum_{ijkl} g_{\sigma\sigma'} \left[\int \mathrm{d}\mathbf{r} \; w_{i\sigma}^*(\mathbf{r}) \; w_{j\sigma'}^*(\mathbf{r}) \; w_{k\sigma'}(\mathbf{r}) \; w_{l\sigma}(\mathbf{r}) \right] a_{i\sigma}^\dagger a_{j\sigma'}^\dagger a_{k\sigma'} a_{l\sigma} \tag{4.20}$$

Here, we include only terms with $i = j = k = l$, and end up with

$$H_u = \frac{1}{2} \sum_{i,\sigma\sigma'} u_{\sigma\sigma'} a_{i\sigma}^\dagger a_{i\sigma'}^\dagger a_{i\sigma'} a_{i\sigma}, \tag{4.21}$$

where

$$u_{\sigma\sigma'} = g_{\sigma\sigma'} \int \mathrm{d}\mathbf{r} \; |w_\sigma(\mathbf{r})|^2 |w_{\sigma'}(\mathbf{r})|^2 = g_{\sigma\sigma'} \int \mathrm{d}\mathbf{r} \; |w(\mathbf{r})|^4. \tag{4.22}$$

Since all Wannier functions belong to the same lattice site, there is polynomial and not exponential dependence on the lattice deepness parameter V_0/E_R. Because of this qualitative difference between the on-site interaction and hopping terms, one can easily tune the ratios the hopping amplitudes and the interaction several orders of magnitude, as demonstrated in the experiment [103].

By redefining $\tilde{\beta}_{l\delta} \to \beta_{l\delta}$ and collecting the terms, we arrive at the Hamiltonian (4.12), but where the model coefficients have been related to the lattice parameters. The general scheme for determining the model parameters can be summarized as follows:

- Calculate the Bloch eigenstates of the non-interacting single-particle problem without SOC

- Fourier transform the Bloch waves to obtain Wannier states

- Use the Wannier states to calculate model parameters through the above integrals

More than the qualitative arguments we have already given, we will not concern ourselves with the details of this, and take model parameters as given.

4.2   System Hamiltonian

We have shown that the tight-binding Hamiltonian of interacting spinor bosons with spin-orbit coupling on a lattice takes the quite general form

$$H = \sum_{i,\delta} \left\{ -t \; \psi_i^\dagger \psi_{i+\delta} - i\psi_i^\dagger \left(\sum_l \beta_{l\delta} \sigma_l \right) \psi_{i+\delta} + \mathrm{h.c.} \right\} + \frac{1}{2} \sum_{\sigma\sigma'} \sum_i u_{\sigma\sigma'} a_{i\sigma}^\dagger a_{i\sigma'}^\dagger a_{i\sigma'} a_{i\sigma} - \sum_{i\sigma} \mu_\sigma n_{i\sigma}. \tag{4.23}$$

Several conventions for representing this Hamiltonian exist. First, we explicitly write out the matrix structure in spin space and discuss the physical interpretation of the terms. We then discuss an elegant way to represent the Hamiltonian in terms of a non-Abelian gauge field.

4.2.1   Matrix representation

Introduce the spin-orbit coupling hopping amplitude

$$s_{i,i+\delta}^{\sigma,-\sigma} = -i \sum_{l \in \{x,y\}} \beta_{l\delta}(\sigma_l)^{\sigma,-\sigma}. \tag{4.24}$$

Since $l \in \{x,y\}$, σ_l is off-diagonal, and writing out the matrix structure of the Hamiltonian (4.23), we obtain

$$H = \sum_{\langle ij \rangle} \begin{pmatrix} a_{i\uparrow}^\dagger & a_{i\downarrow}^\dagger \end{pmatrix} \begin{pmatrix} -t & s_{ij}^{\uparrow\downarrow} \\ s_{ij}^{\downarrow\uparrow} & -t \end{pmatrix} \begin{pmatrix} a_{j\uparrow} \\ a_{j\downarrow} \end{pmatrix} + \frac{1}{2} \sum_{i\sigma\sigma'} u_{\sigma\sigma'} n_{i\sigma}(n_{i\sigma'} - \delta_{\sigma\sigma'}) - \sum_{i\sigma} \mu_\sigma n_{i\sigma}, \tag{4.25}$$

where we have rewritten the interaction term using density operators $n_{i\sigma} = a_{i\sigma}^\dagger a_{i\sigma}$ and require $s_{ij}^{\sigma\sigma'}$ to be anti-symmetric under $i \leftrightarrow j$ to preserve hermiticity. From the definition of $s_{ij}^{\sigma,-\sigma}$, we then obtain symmetry relations

$$\begin{aligned} s_{ij}^{-\sigma,\sigma} &= -\left(s_{ij}^{\sigma,-\sigma}\right)^* \\ s_{ji}^{\sigma,-\sigma} &= -s_{ij}^{\sigma,-\sigma} \\ s_{ji}^{-\sigma,\sigma} &= \left(s_{ij}^{\sigma,-\sigma}\right)^*. \end{aligned} \tag{4.26}$$

All these coefficients can be expressed in terms of $s_{i,i+\delta}^{\uparrow\downarrow} \equiv s_\delta$. In terms of the matrix elements $\beta_{l\delta}$, we get

$$s_\delta = -i\beta_{x\delta} - \beta_{y\delta}. \tag{4.27}$$

We now write the elements in the spin-orbit coupling matrix $\beta_{l\delta}$ as

$$\beta_{l\delta} = \begin{pmatrix} \gamma_x & \eta \\ \kappa & \gamma_y \end{pmatrix}. \tag{4.28}$$

Since a general linear combination of Rashba and Dresselhaus spin-orbit coupling can be realized by choosing a matrix with only diagonal or only off-diagonal elements, we will typically set $\gamma_x = \gamma_y = 0$. At some point, we will typically also specialize to the case of pure Rashba spin-orbit coupling by setting $\eta = -\kappa$.

The interaction term coefficients can in general be written as

$$u_{\sigma\sigma'} = u \begin{pmatrix} 1 + \delta/2 & \lambda \\ \lambda & 1 - \delta/2 \end{pmatrix}, \tag{4.29}$$

so that λ is the inter- relative to intracomponent interaction strength, while δ quantifies the difference between the intracomponent interactions of the two boson species. For the remainder of this thesis, we set $\delta = 0$. As discussed in section 3.1.4, experimentalists have large freedom to tune the interaction between particles.

The above Hamiltonian is represented schematically in figure 4.1. The diagonal terms in the hopping matrix correspond to regular spin-conserving hoppings, since the term $a_{i\sigma}^\dagger a_{i+\delta,\sigma}$ creates a particle at lattice site i and destroys one with the same spin at $i + \delta$. Similarly, the off-diagonal
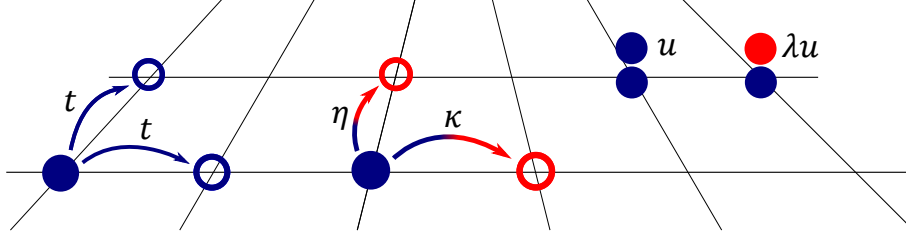
Figure 4.1: Schematic representation of the spin-orbit coupled Bose-Hubbard Hamiltonian. In addition to regular spin-conserving hoppings with amplitude t, there are SOC-induced non-spin-conserving hoppings with amplitudes κ and η in the x- and y-directions. The interaction energy between two particles of the same species at the same lattice site is u, while the corresponding intercomponent interaction is λu.

terms in the matrix correspond to hoppings with spin-flip, which is exactly what SOC corresponds to in the Raman transition picture. The on-site particle interaction strengths are also illustrated in the figure.

4.2.2   Non-Abelian gauge field representation

In this section, we discuss a related way to represent the Hamiltonian. The general spin-orbit coupled Bose-Hubbard model with on-site density-density interaction can be written as [104]

$$H = -t_0 \sum_{\langle ij \rangle} \psi_i^\dagger T_{ij} \psi_j + \frac{1}{2} \sum_{i,\sigma\sigma'} u_{\sigma\sigma'} n_{i\sigma}(n_{i\sigma'} - \delta_{\sigma\sigma'}) - \sum_{i,\sigma} \mu_\sigma n_{i\sigma}. \tag{4.30}$$

For off-diagonal spin-orbit coupling matrix $\beta_{l\delta}$, T_{ij} can be expressed as $T_{ij} = \exp[i\mathbf{A} \cdot (\mathbf{r}_j - \mathbf{r}_i)]$, where $\mathbf{A} = (\alpha\sigma_y, \beta\sigma_x, 0)$ is a non-Abelian gauge field. The justification for this is that for charged particles in an electromagnetic field, the electromagnetic vector potential $\mathbf{A}_{\text{EM}}$ couples linearly to the particle momenta [22], just like the Pauli spin-matrices in our spin-orbit coupling term. In the tight-binding limit, the interaction with the electromagnetic fields therefore appears in exactly the same way. In contrast to the electromagnetic vector potential components, the components of our gauge potential $\mathbf{A}$ do not commute, and $\mathbf{A}$ is therefore said to be non-Abelian.

To compare with our previous Hamiltonian, Taylor expand the exponential by using $(\sigma_l)^2 = 1$. This gives

$$\exp(i\alpha\sigma_l) = \cos(\alpha) + i\sin(\alpha)\sigma_l. \tag{4.31}$$

The Hamiltonian becomes

$$H = -t_0 \sum_i \left\{ \psi_i^\dagger \left(\cos\alpha + i\sin\alpha\ \sigma_y \right) \psi_{i+\hat{x}} + \psi_i^\dagger \left(\cos\beta + i\sin\beta\ \sigma_x \right) \psi_{i+\hat{y}} + \text{h.c.} \right\} \tag{4.32}$$

$$= \sum_i \left\{ \psi_i^\dagger \begin{pmatrix} -t_0\cos\alpha & -t_0\sin\alpha \\ t_0\sin\alpha & -t_0\cos\alpha \end{pmatrix} \psi_{i+\hat{x}} + \psi_i^\dagger \begin{pmatrix} -t_0\cos\beta & -it_0\sin\beta \\ -it_0\sin\beta & -t_0\cos\beta \end{pmatrix} \psi_{i+\hat{y}} + \text{h.c.} \right\}. \tag{4.33}$$

We may compare this with the Hamiltonian (4.25). The spin-orbit coupling coefficients can be related through $\kappa = t_0\sin\alpha$ and $\eta = t_0\sin\beta$. Unlike the previous Hamiltonian, the ordinary hopping amplitudes are component-dependent. There is therefore a difference between the two representations, but for Rashba SOC with $\eta = -\kappa$ and $\beta = -\alpha$, the two Hamiltonians are again equivalent with $t = t_0\cos\alpha$.

Another choice for the non-Abelian gauge potential is $\mathbf{A} = (\alpha\sigma_x, \beta\sigma_y, 0)$, corresponding to a diagonal SOC-matrix $\beta_{\gamma\delta}$. Both conventions are in use in the literature, but we stick to the off-diagonal form.

4.3 Superfluid to Mott insulator transition

We now discuss some characteristics of the Bose-Hubbard model we derived in the previous section. First, we consider the single-species case and the superfluid to Mott insulator (SF-MI) quantum phase transition present in this system. Based on recent literature, we then consider the spin-orbit coupled two-component model and describe some of its special features.

4.3.1 Single species SF-MI transition

The single species Bose-Hubbard model can be obtained by removing the intercomponent interaction and spin-orbit coupling in the model we derived in the previous section, obtaining

$$H = -t_0 \sum_{i,\delta} (a_i^\dagger a_{i+\delta} + a_{i+\delta}^\dagger a_i) + \frac{u}{2} \sum_i n_i(n_i - 1) - \mu \sum_i a_i^\dagger a_i, \qquad (4.34)$$

where we have expressed the bosons in the interaction term through the density operators n_i. As discussed in section 4.1.2, one can tune the ratio t/u several orders of magnitude, between the regimes where the kinetic and interaction terms dominate. We consider therefore the model in these two extreme limits, the superfluid regime $t \gg u$ and the Mott insulating regime $t \ll u$.

Consider first $u = 0$. In addition to the chemical potential term controlling the number of particles, there is only the kinetic term, which prefers delocalization of particles across the entire lattice. One may calculate the energy spectrum exactly by introducing the Fourier transform, analogous to our calculations in chapter 5. The ground state then corresponds to the $\mathbf{q} = 0$ state. In terms of lattice site creation operators, one may then write the ground state as [103]

$$|\psi_{\text{SF}}\rangle \propto \left(\sum_i a_i^\dagger \right)^M |0\rangle, \qquad (4.35)$$

where $|0\rangle$ is the vacuum, and the total number of particles M is determined by the chemical potential.

In the opposite limit, setting $t = 0$, the Hamiltonian is separable. As argued in the book by Sachdev [105], the many-body eigenstates are lattice site occupation number states $|\{n_i\}\rangle$, where n_i is an integer representing the number of particles at lattice i. Following the argument there, we minimize the energy at each lattice site with respect to n_i, obtaining as function of μ a stepwise increasing lattice site occupation n at every lattice site. In second quantization, the ground state can then be written as [103]

$$|\Psi_{\text{MI}}\rangle \propto \prod_i \left(a_i^\dagger \right)^n |0\rangle. \qquad (4.36)$$

The two states have completely different properties. Physically, the Mott insulator state corresponds to a classical state where particles sit at given lattice sites. In the superfluid phase, particles condense in the Bloch state with the lowest energy. While the number of particles at each lattice site is fixed in the Mott insulator, in the superfluid phase, they are Poisson distributed in the thermodynamic limit [101].

The superfluid to Mott insulator transition was measured experimentally by Greiner *et al.* [103] using time-of-flight measurement. In the superfluid phase, emergence of coherent matter waves from the lattice sites gives an interference pattern at the equivalent wave vectors $\mathbf{q} = 2k_L(n_x, n_y)$, where n_x and n_y are integers. Tuning the lattice depth above a critical value corresponding to the SF-MI transition, loss of coherence destroys the pattern.

The excitation spectra of the two phases are also fundamentally different. For the superfluid, breaking of the global U(1) symmetry $b_i \rightarrow e^{i\phi}b_i$ leads to a gapless Goldstone mode [1, 105, 106]. In the Mott insulator, the fundamental excitation is the displacement of an atom from one lattice

site to another [101]. This is associated with a given energy, and possible excitations are therefore multiples of this. The excitation spectra were measured in the above mentioned experiment [103], finding excellent agreement with theory. Using interference peak width as a measure of excitations in the superfluid phase, they could find the spectrum even in the Mott insulator phase by first reducing the lattice depth down in the superfluid regime, before sudden release and free expansion.

So far, we have discussed various characteristics of the two phases in the extreme limits $t \gg u$ and $t \ll u$. In between, there is a second order quantum phase transition [105]. Considering t/u and μ as system parameters, the goal is to describe the phase diagram. The correct qualitative result can be obtained by relatively simple means using a Gutzwiller variational state [101], utilizing that in both extreme limits, the ground state is approximated by a product state. Various other methods have also been applied [107], including mean field decoupling of lattice sites in the kinetic term [105, 108], strong coupling expansion [109], and Monte-Carlo simulations [110, 111]. More recently, a new method known as boson dynamical mean field theory has also been developed [112, 113].

The phase diagram shows a hierarchy of Mott lobes, and can be found in the references [1, 101, 105]. Inside each lobe, the system has an integer number of particles per lattice site. Dimensionality is of importance, and in particular, the phase diagram in one dimension looks somewhat different than in higher dimensions [107, 114].

4.3.2   Spin-orbit coupled SF-MI transition

Consider now the spin-orbit coupled Bose-Hubbard model. The basic situation has not changed. Ordinary hopping and SOC couple neighbouring lattice sites and prefer delocalization, while the interaction term still consists only of lattice site occupation number operators favouring localization. The superfluid to Mott insulator transition therefore remains, but the two components of the condensate allow a much richer description of the two phases. In the remaining part of this thesis, the goal is to analyse the pseudo-spin structure of cold atoms with the Bose-Hubbard model. In chapter 5, we do this in the superfluid regime with weak interaction, and obtain a phase separation transition line. Chapter 6 focuses on the strongly coupled case, and here we derive an effective spin model displaying rich ground state spin textures. The SF-MI transition itself has also been studied in several articles, mostly using approaches already familiar from the single-component Bose-Hubbard model [104, 115–120]. Below, we consider some of these articles in more detail.

Graß *et al.* [115] apply a re-summed hopping expansion approach to the spinor spin-orbit coupled model, obtaining an effective action by treating the hopping term as a perturbation [107, 121]. Bolukbasi *et al.* use a Gutzwiller variational Ansatz, allowing both boson species in the lattice site product state, and minimizing the ground state energy numerically. Cole *et al.* [104] use methods reminiscent of the mean-field decoupling of the hopping term mentioned in the previous section, generalizing to spin-orbit coupled, inhomogeneous solutions by iteratively diagonalizing a finite set of single site effective Hamiltonians. He *et al.* [120] apply the boson dynamical mean field theory.

All these papers show that the critical transition parameter $(t_0/u)_c$ increases with the gauge field strength α from zero spin-orbit coupling with $\alpha = 0$, up to $\alpha = \pi/2$, where ordinary hoppings are suppressed in favour of SOC-induced spin-flip hoppings. The Mott insulating state is therefore more stable toward hoppings with spin-flip than toward ordinary hoppings. This can be understood with slave boson mean field theory [104, 120], where particle and spin degrees of freedom are decoupled. Another common feature is that magnetic texture in the Mott insulating phase is mimicked by the superfluid state on the other side of the SF-MI transition.

Chapter 5

Weak coupling

In the weakly coupled limit of the Bose-Hubbard model discussed in the previous chapter, the system is superfluid. The goal of this chapter is to describe the transition from a mixed to a phase separated state that arises through competition between interaction and spin-orbit coupling.

This problem was studied using mean field theory and classical Monte-Carlo simulations on a Landau-Ginzburg model in a recent paper [100]. Alternately, one may minimize the Gross-Pitaevskii interaction energy with respect to occupation of the four minima of the non-interacting dispersion relation [104, 122]. We instead use a real space homogeneous density mean field theory. After finding the dispersion relation of the effective single-particle Hamiltonian, we solve the self-consistent equations for Rashba SOC, obtaining the phase diagram at zero and finite temperature as function of the inter- relative to intracomponent interaction and spin-orbit coupling strength.

5.1 Mean field Hamiltonian and its diagonalization

Our starting point is the Hamiltonian (4.25) in the previous chapter. Assume weak coupling $u \ll t$, or equivalently small average filling per lattice site. Write the lattice site occupation number as

$$n_{i\sigma} = n_{0\sigma} + \delta n_{i\sigma}, \tag{5.1}$$

where we have assumed uniform component densities $n_{0\sigma} = \langle n_{i\sigma} \rangle$. The presence of spin textured ground states may violate this assumption [100, 104, 120, 122], but since the gas is homogeneous in certain parameter regimes and fluctuations in the component densities may be small, we still expect our mean field theory to reproduce real physics.

We may now decouple the interaction term by neglecting terms of order $\mathcal{O}(\delta n^2)$. This gives mean field interaction Hamiltonian

$$H_u^{\mathrm{MF}} = -\frac{1}{2}u \sum_{i\sigma} n_{i\sigma} - \frac{N}{2} \sum_{\sigma\sigma'} u_{\sigma\sigma'} n_{0\sigma} n_{0\sigma'} + \sum_{i\sigma\sigma'} u_{\sigma\sigma'} n_{0\sigma} n_{i\sigma'}, \tag{5.2}$$

which can also be seen from the general argument in [123]. Introducing quantities

$$n_0 = n_{0\uparrow} + n_{0\downarrow} \tag{5.3}$$
$$\Delta n_0 = n_{0\uparrow} - n_{0\downarrow}, \tag{5.4}$$

the constant term in (5.2) can be written as

$$H_0 \equiv -\frac{Nu}{4} \left[(1+\lambda)n_0^2 + (1-\lambda)\Delta n_0^2 \right], \tag{5.5}$$

and the full mean field Hamiltonian is

$$H^{\mathrm{MF}} = H_0 + \sum_{\langle ij \rangle} \begin{pmatrix} a_{i\uparrow}^\dagger & a_{i\downarrow}^\dagger \end{pmatrix} \begin{pmatrix} -t & s_{ij}^{\uparrow\downarrow} \\ s_{ij}^{\downarrow\uparrow} & -t \end{pmatrix} \begin{pmatrix} a_{j\uparrow} \\ a_{j\downarrow} \end{pmatrix} + \sum_{i\sigma} \left[\sum_{\sigma'} u_{\sigma\sigma'} n_{0\sigma'} - \mu_\sigma - u/2 \right] n_{i\sigma}. \qquad (5.6)$$

The hopping terms are unchanged, and the mean-field interaction simply renormalizes the chemical potential. We let $\mu_\sigma - u/2 \to \mu_\sigma$ since μ is a control parameter, but keep the dependence on $n_{0\sigma}$ explicit, since these are variational parameters.

To diagonalize this Hamiltonian, we decouple neighbouring lattice sites by introducing the Fourier transformed boson operators $a_{k\sigma}^\dagger$ and $a_{k\sigma}$ by

$$a_{k\sigma} = \frac{1}{\sqrt{N}} \sum_i a_{i\sigma} e^{-i\mathbf{k}\cdot\mathbf{r}_i} \qquad (5.7)$$

$$a_{k\sigma}^\dagger = \frac{1}{\sqrt{N}} \sum_i a_{i\sigma}^\dagger e^{+i\mathbf{k}\cdot\mathbf{r_i}}, \qquad (5.8)$$

where N is the number of lattice sites. The inverse Fourier transform gives

$$a_{i\sigma} = \frac{1}{\sqrt{N}} \sum_k a_{i\sigma} e^{+i\mathbf{k}\cdot\mathbf{r}_i} \qquad (5.9)$$

$$a_{i\sigma}^\dagger = \frac{1}{\sqrt{N}} \sum_k a_{i\sigma}^\dagger e^{-i\mathbf{k}\cdot\mathbf{r}_i}. \qquad (5.10)$$

Considering the regular hopping term in (5.6) first, and inserting the above representations for the square lattice, we get

$$\begin{aligned} H_t &= \frac{1}{N} \sum_{kq} \sum_{i,\delta,\sigma} (-t) \big(a_{q\sigma}^\dagger e^{i\mathbf{q}\cdot\mathbf{r}_i} a_{k\sigma} e^{-i\mathbf{k}\cdot(\mathbf{r}_i+\delta)} + \mathrm{h.c.} \big) \\ &= -t \sum_{k\sigma} \big(e^{ik_\delta} a_{k\sigma}^\dagger a_{k\sigma} + \mathrm{h.c.} \big) \\ &= -2t \sum_{k\delta\sigma} \cos k_\delta \; a_{k\sigma}^\dagger a_{k\sigma}, \end{aligned} \qquad (5.11)$$

where we have used the delta function identity

$$\frac{1}{N} \sum_i e^{i(\mathbf{k}-\mathbf{q})\cdot\mathbf{r}_i} = \delta_{k,q}. \qquad (5.12)$$

A similar calculation for the renormalized chemical potential term gives

$$\sum_i a_{i\sigma}^\dagger a_{i\sigma} = \sum_k a_{k\sigma}^\dagger a_{k\sigma}. \qquad (5.13)$$

Inserting this in the Hamiltonian and writing out the sum over σ', we end up with

$$H_u^{\mathrm{MF}} + H_\mu = \sum_{k\sigma} \left\{ \frac{u}{2} \left[(1+\lambda)n_0 + \sigma(1-\lambda)\Delta n_0 - (\delta/2)(n_0 + \Delta n_0) \right] - \mu_\sigma \right\} a_{k\sigma}^\dagger a_{k\sigma}. \qquad (5.14)$$

In Fourier-space, the regular hopping, interaction, and chemical potential terms give the same operator structure. We can therefore combine them to obtain

$$H_t + H_u^{\mathrm{MF}} + H_\mu = \sum_k \psi_k^\dagger \begin{pmatrix} \epsilon_{k\uparrow} & 0 \\ 0 & \epsilon_{k\downarrow} \end{pmatrix} \psi_k, \tag{5.15}$$

with

$$\begin{aligned} \epsilon_{k\sigma} = & -2t(\cos k_x + \cos k_y) - \sigma \Delta\mu/2 - \bar{\mu} \\ & \frac{1}{2} u n_0 \left[(1 + \lambda) + \sigma(1 - \lambda)\Delta n_0/n_0 \right] - u n_0 (\delta/4) \left(1 + \Delta n_0/n_0\right), \end{aligned} \tag{5.16}$$

and where we have introduced $\bar{\mu} = (\mu_\uparrow + \mu_\downarrow)/2$ and $\Delta\mu = \mu_\uparrow - \mu_\downarrow$. From now on, we set $\delta = 0$. Putting it back into the equations should mostly be a trivial generalization.

A similar calculation is performed for the spin-orbit coupling. This term couples creation and annihilation operators for different species in real space, and must therefore do so in Fourier space as well. Using the symmetry relations for $s_{ij}^{\alpha\beta}$ in equation (4.26), we can express the spin-orbit coupling as

$$H_{\mathrm{SOC}} = \sum_{i,\delta} \left\{ s_\delta a_{i\uparrow}^\dagger a_{i+\delta,\downarrow} - s_\delta a_{i+\delta,\uparrow}^\dagger a_{i\downarrow} - s_\delta^* a_{i\downarrow}^\dagger a_{i+\delta,\uparrow} + s_\delta^* a_{i+\delta,\downarrow}^\dagger a_{i\uparrow} \right\}. \tag{5.17}$$

The terms are on the form

$$\begin{aligned} \sum_i a_{i\sigma}^\dagger a_{i+\delta,-\sigma} &= \frac{1}{N} \sum_{kq} \sum_i a_{q\sigma}^\dagger \mathrm{e}^{-i\mathbf{q}\cdot\mathbf{r}_i} a_{q,-\sigma} \mathrm{e}^{i\mathbf{k}\cdot(\mathbf{r}_i+\delta)} \\ &= \sum_k a_{k\sigma}^\dagger a_{k,-\sigma} \mathrm{e}^{ik\delta}. \end{aligned} \tag{5.18}$$

Collecting all the terms gives spin-orbit coupling

$$\begin{aligned} H_{\mathrm{SOC}} &= \sum_{k,\delta} 2i \sin k_\delta \left(s_\delta a_{k\uparrow}^\dagger a_{k\downarrow} - s_\delta^* a_{k\downarrow}^\dagger a_{k\uparrow} \right) \\ &= \sum_{k,\delta} 2i \sin k_\delta \begin{pmatrix} a_{k\uparrow}^\dagger & a_{k\downarrow}^\dagger \end{pmatrix} \begin{pmatrix} 0 & s_\delta \\ -s_\delta^* & 0 \end{pmatrix} \begin{pmatrix} a_{k\uparrow} \\ a_{k\downarrow} \end{pmatrix}. \end{aligned}$$

We arrive at momentum space Hamiltonian

$$H^{\mathrm{MF}} = H_0 + \sum_k \begin{pmatrix} a_{k\uparrow}^\dagger & a_{k\downarrow}^\dagger \end{pmatrix} \begin{pmatrix} \epsilon_{k\uparrow} & s_k \\ s_k^* & \epsilon_{k\downarrow} \end{pmatrix} \begin{pmatrix} a_{k\uparrow} \\ a_{k\downarrow} \end{pmatrix} \equiv H_0 + \sum_k \psi_k^\dagger H_k \psi_k, \tag{5.19}$$

where we have defined

$$s_k = \sum_\delta 2i \sin k_\delta \; s_\delta. \tag{5.20}$$

Inserting the coefficients of the original spin-orbit coupling matrix $\beta_{l\delta}$, we get

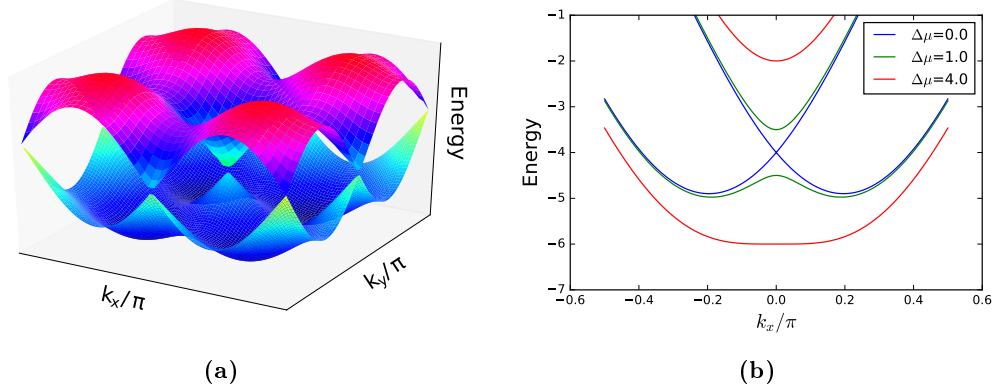$$s_\delta = s_{ij}^{\uparrow\downarrow} = -i\beta_{x\delta} - \beta_{y\delta}, \tag{5.21}$$

Figure 5.1: Single particle dispersion relation of non-interacting particles. In (a), the lowest band has four minima at $\mathbf{k} = (\pm k_0, k_0)$ and $\mathbf{k} = (k_0, \pm k_0)$, and the Zeeman field causes a gap between the energy bands at $\mathbf{k} = 0$. In (b), the dispersion relation is plotted along $k_x = k_y$ for different Zeeman fields $\Delta\mu$ in units of the hopping amplitude t.

and hence,

$$s_k = 2(\gamma_x - i\kappa)\sin q_x + 2(\eta - i\gamma_y)\sin k_y$$

as general expression for the diagonal terms. In the following, we consider Rashba SOC with $\gamma_x = \gamma_y = 0$ and $\eta = -\kappa$, and note therefore in particular

$$s_k^{\text{Rashba}} = -2\kappa(i\sin k_x + \sin k_y). \tag{5.22}$$

The Hamiltonian (5.19) can be diagonalized with a unitary transformation. Letting $\psi_k = P_k\phi_k$, where ϕ_k is composed of band index annihilation operators $a_{k\pm}$, we want $P_k^\dagger H_k P_k$ to be diagonal. The eigenvalues of H_k are

$$E_{k\pm} = \frac{1}{2}(\epsilon_{k\uparrow} + \epsilon_{k\downarrow}) \pm \sqrt{\frac{1}{4}(\epsilon_{k\uparrow} - \epsilon_{k\downarrow})^2 + |s_k|^2}. \tag{5.23}$$

Introducing $r_k = E_{k+} - \epsilon_{k\downarrow} = -(E_{k-} - \epsilon_{k\uparrow})$, the matrix of normalized eigenvectors can be written as

$$P_k = \frac{1}{\sqrt{r_k^2 + |s_k|^2}} \begin{pmatrix} r_k & s_k \\ s_k^* & -r_k \end{pmatrix}. \tag{5.24}$$

Since this is a unitary matrix, $a_{k\alpha}^\dagger$ and $a_{k\alpha}$ satisfy boson commutation relations. Note that r_k can be expressed as

$$r_k = \Delta_0 + \sqrt{\Delta_0^2 + |s_k|^2} \tag{5.25}$$

by defining Δ_0 as

$$\Delta_0 = \frac{1}{2}(\epsilon_{k\uparrow} - \epsilon_{k\downarrow}) = -u(\lambda - 1)\Delta n_0/2 - \Delta\mu/2, \tag{5.26}$$

which is in fact $\mathbf{k}$-independent. If we were to include $k_\delta\sigma_z$-terms in the Hamiltonian, this would not be the case. An imbalance Δn_0 acts on the dispersion relation in the same way as the Zeeman field $\Delta\mu$.

The dispersion relation of non-interacting particles is known also from the literature [124], and we plot it for Rashba SOC in figure 5.1. The continuous ground state degeneracy is lifted by the optical lattice, and instead, there are four minima at finite $\mathbf{k}$. If the Zeeman field is sufficiently strong, the four minima vanish in favour of a single minimum at $\mathbf{k} = 0$, as illustrated in figure 5.1b. This is analogous to the continuum result in section 3.3.

With band index α, the diagonalized mean field Hamiltonian becomes

$$H^{\mathrm{MF}} = H_0 + \sum_{k\alpha} E_{k\alpha} a_{k\alpha}^\dagger a_{k\alpha}. \tag{5.27}$$

Thermal occupation of energy eigenstates is given by the Bose-Einstein distribution. Assuming we can calculate the variational parameters n_0 and Δn_0, the mean field expectation value of any operator $O(a_i, a_i^\dagger)$ can be obtained by expressing it in terms of the new operators $a_{k\pm}, a_{k\pm}^\dagger$, for which thermal expectation values are know. In particular, it would be interesting to do this for bond current operators, trying to reproduce the anti-ferromagnetic pattern of loop currents in Refs. [104, 125].

5.2 Self-consistent determination of variational parameters

As discussed in [123], there are two equivalent methods for determining the variational parameters of a mean field theory:

- Minimizing the free energy with respect to variational parameters.

- Obtaining self-consistent equations by calculating expectation values within the mean field approximation.

The two methods lead to the same equations, but since the second method gives a somewhat simpler calculation, we only do the second in detail for finite temperature. At zero temperature, the first approach is advantageous. We give a proof of equivalence in appendix A.

Considering the first method first, the free energy is

$$\Omega = H_0 + k_B T \sum_{k\alpha} \ln\big(1 - e^{-\beta E_{k\alpha}}\big). \tag{5.28}$$

Minimization with respect to $n_{0\uparrow}$ and $n_{0\downarrow}$ gives

$$\frac{\partial \Omega}{\partial n_{0\sigma}} = 0, \tag{5.29}$$

which can be solved for n_0 and Δn_0 at fixed μ_σ. Subsequently, we should check whether the solution is a minimum by calculating the eigenvalues of the matrix of second derivatives. Alternately, one may compute the free energy for the small set of minimum candidates.

The alternate route is to solve the two equations

$$n_{0\sigma} = \frac{1}{N} \sum_k \langle a_{k\sigma}^\dagger a_{k\sigma} \rangle, \tag{5.30}$$

where brackets denote thermal average. Since the matrix P_k is hermitian and unitary, it is its own inverse, so for boson species $\uparrow$, we get

$$\langle a_{k\uparrow}^{\dagger} a_{k\uparrow} \rangle = (r_k^2 + |s_k|^2)^{-1} \left\langle (r_k^* \hat{a}_{k+}^{\dagger} + s_k^* \hat{a}_{k-}^{\dagger})(r_k \hat{a}_{k+} + s_k \hat{a}_{k-}) \right\rangle$$

$$= (r_k^2 + |s_k|^2)^{-1} \left[|r_k|^2 \langle \hat{a}_{k+}^{\dagger} \hat{a}_{k+} \rangle + |s_k|^2 \langle \hat{a}_{k-}^{\dagger} \hat{a}_{k-} \rangle + r_k^* s_k \langle \hat{a}_{k+}^{\dagger} \hat{a}_{k-} \rangle + r_k s_k^* \langle \hat{a}_{k-}^{\dagger} \hat{a}_{k+} \rangle \right]$$

$$= \frac{r_k^2}{r_k^2 + |s_k|^2} n_B(E_{k+}) + \frac{|s_k|^2}{r_k^2 + |s_k|^2} n_B(E_{k-}),$$

where the last terms in the intermediate step are zero because the Hamiltonian is diagonal in band operators, and where $n_B(E)$ is the Bose-Einstein distribution

$$n_B(E) = \frac{1}{e^{\beta E} - 1}. \tag{5.31}$$

For species $\downarrow$, the coefficients r_k^2 and $|s_k|^2$ are interchanged, and we end up with self-consistent equations

$$n_{0\uparrow} = \frac{1}{N} \sum_k \frac{1}{r_k^2 + |s_k|^2} \left\{ \frac{r_k^2}{\exp(\beta E_{k+}) - 1} + \frac{|s_k|^2}{\exp(\beta E_{k-}) - 1} \right\} \tag{5.32}$$

$$n_{0\downarrow} = \frac{1}{N} \sum_k \frac{1}{r_k^2 + |s_k|^2} \left\{ \frac{|s_k|^2}{\exp(\beta E_{k+}) - 1} + \frac{r_k^2}{\exp(\beta E_{k-}) - 1} \right\}. \tag{5.33}$$

In terms of n_0 and Δn_0, we may write this as

$$n_0 = \frac{1}{N} \sum_{k\alpha} n_B(E_{k\alpha}) \tag{5.34}$$

$$\Delta n_0 = \frac{1}{N} \sum_{k\alpha} \Delta n_{k\alpha} n_B(E_{k\alpha}), \tag{5.35}$$

with imbalance

$$\Delta n_{k\alpha} = \alpha \frac{r_k^2 - |s_k|^2}{r_k^2 + |s_k|^2} \tag{5.36}$$

characteristic for each eigenstate. When Δ_0 is negative and $|s_k|^2 = 0$, we get $r_k = 0$. The characteristic imbalance must therefore be calculated explicitly at this point, and the limiting value is

$$\lim_{|s_k| \to 0} \Delta n_{k\alpha} = -\alpha. \tag{5.37}$$

The above self-consistent equations contain a Brillouin zone sum, but are not especially irregular. At $T = 0$, they can be simplified by assuming all particles condense into the minimum of the effective single-particle dispersion relation. We consider this next.

5.2.1   Zero-temperature phase diagram

Consider first zero spin-orbit coupling. The energy eigenvalues are $\epsilon_{k\sigma}$, and with $N n_{0\sigma}$ particles in the state (k, σ), the total energy becomes

$$E_{\text{tot}} = H_0 + N n_{0\uparrow} \epsilon_{k\uparrow} + N n_{0\downarrow} \epsilon_{k\downarrow}. \tag{5.38}$$

The minimum resides at $\mathbf{k} = 0$, and the energy therefore becomes

$$E_{\text{tot}} = Nn_0 \left[-4t + \frac{1}{4}un_0(1+\lambda) - \bar{\mu} \right] + Nn_0 \left[\frac{1}{4}n_0 u(1-\lambda) \left(\frac{\Delta n_0}{n_0} \right)^2 - \frac{1}{2}\Delta\mu \left(\frac{\Delta n_0}{n_0} \right) \right], \quad (5.39)$$

where we have substituted the variables $n_{0\sigma}$ with n_0 and Δn_0. Completing the square gives

$$E_{\text{tot}} = Nn_0 \left[-4t + \frac{1}{4}un_0(1+\lambda) - \bar{\mu} \right] \quad (5.40)$$

$$+ \frac{1}{4}Nun_0^2(1-\lambda) \left[-\left(\frac{\Delta\mu}{n_0 u(1-\lambda)} \right)^2 + \left(\frac{\Delta n_0}{n_0} - \frac{\Delta\mu}{un_0(1-\lambda)} \right)^2 \right]. \quad (5.41)$$

One can check that λ drops when $\Delta n_0 = n_0$, since then, there is only one species present. We have to minimize this energy. The first term determines the average occupation n_0, but since $\bar{\mu}$ is a control parameter, we are not particularly interested in this term. Minimizing the second term under the restriction $|\Delta n_0/n_0| < 1$ reveals

$$\frac{\Delta n_0}{n_0} = \begin{cases} \frac{\Delta\mu}{n_0 u(1-\lambda)}, & \lambda \leq \lambda_{\text{crit}} \\ \text{sgn}(\Delta\mu), & \lambda \geq \lambda_{\text{crit}}, \end{cases} \quad (5.42)$$

where $\lambda_{\text{crit}} = 1 - \Delta\mu/n_0 u$. Consistent with our intuition, the Zeeman term eases the phase separation transition, and leads to a sharp but continuous transition at small Zeeman fields.

We now generalize this argument to finite spin-orbit coupling. The square root term in the dispersion relation can shift the minimum from $\mathbf{k} = 0$ to a finite quasi-momentum vector. At any given n_0 and Δn_0, we want to know where this happens. Choosing pure Rashba or pure Dresselhaus SOC, the conditions $\partial E_{k-}/\partial k_\delta$ give possible solutions $\mathbf{k} = 0$ and

$$\sin^2 k_x = \sin^2 k_y = \frac{1}{(2 + \kappa^2/t^2)} \left(\frac{\kappa^2}{t^2} - \frac{\Delta_0^2}{4\kappa^2} \right). \quad (5.43)$$

For

$$|\Delta_0| \geq 2\kappa^2/t, \quad (5.44)$$

there is no solution at finite quasi-momentum, and the minimum sits at $\mathbf{k} = 0$.

The idea is again to assume that all particles condense into a dispersion relation minimum at zero temperature. The location and energy of the minima still depend on the variational parameters, but condensation into the four degenerate minima fixes the imbalance to the characteristic imbalance of these states. We may therefore calculate Δn_0 for the finite-$\mathbf{k}$ minimum through

$$\Delta n_0 = \Delta n_{k\alpha} \quad (5.45)$$

by inserting the momentum space location of the minima from equation (5.43).

We consider in particular the phase transition driven by interaction. For a small Zeeman field $\Delta\mu$, it is always possible to choose Δn_0 so that minima at finite $\mathbf{k}$ exist. Since this imposes an additional restriction on Δn_0, it might be energetically favourable to condense in $\mathbf{k} = 0$, where there are no restrictions other than $|\Delta n_0|/n_0 \leq 1$. The strategy for determining the phase diagram should therefore be the following:

- Assuming the minimum resides at finite quasi-momentum vector, determine the imbalance from (5.45) at fixed n_0 subject to the restrictions $|\Delta_0| < 2\kappa^2/t$ and $|\Delta n_0|/n_0 \leq 1$.

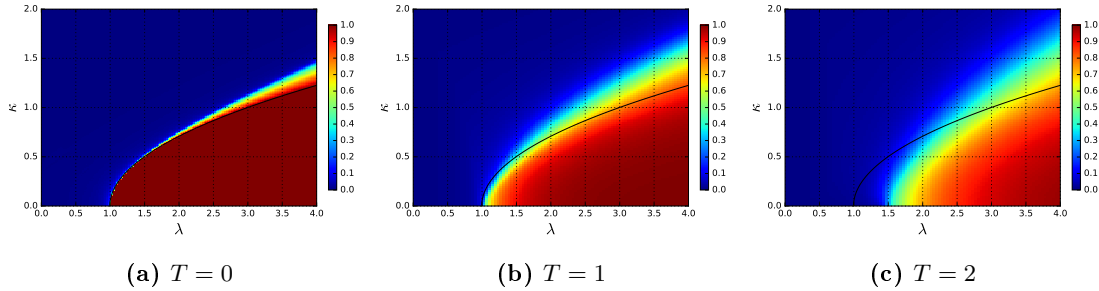- Minimize $E_{\mathbf{k}=0,-}$ subject to $|\Delta n_0|/n_0 \leq 1$. This can be done analytically.

(a) $T = 0$ **(b)** $T = 1$ **(c)** $T = 2$

Figure 5.2: Imbalance Δn_0 as function of spin-orbit coupling strength κ and inter-species interaction λ for temperatures $T = 0, 1, 2$. The black line shows the analytic condition (5.46), where complete phase separation is reached at $T = 0$. Both κ and T are measured in units of the hopping amplitude t.

- Compare the two energies and pick out the smallest. The imbalance Δn_0 takes value that optimizes the best energy.

Based on the above procedure, a simple analytic condition for complete phase separation can be derived. At zero SOC and small but finite chemical potential imbalance $\Delta\mu$, the transition is continuous. At sufficiently strong intercomponent interaction, we always expect complete phase separation. Starting in this regime and reducing λ, at some point, the dispersion relation minimum floats out from $\mathbf{k} = 0$ with characteristic imbalance $\Delta n_0/n_0 = 1$ to some finite $\mathbf{k}$. If this happens continuously, it must happen when $|\Delta_0| = 2\kappa^2/t$ can be satisfied with imbalance $\Delta n_0/n_0 = 1$. Expressing this condition in terms of λ gives transition line

$$\lambda = 1 - \frac{\Delta\mu}{un_0} + \frac{4\kappa^2}{tun_0}. \tag{5.46}$$

The transition point at $\kappa = 0$ coincides our earlier calculation. Quadratic dependence on κ is qualitatively similar to the phase diagram in Ref. [100].

For intercomponent interaction below the complete phase separation transition point, the imbalance is determined by the finite-$\mathbf{k}$ solution. The zero-temperature phase diagram is presented in figure 5.2a, where the blue region corresponds to the mixed phase with $\Delta n_0 \approx 0$, and the system is completely phase separated in the red region. Starting from the transition point and lowering λ, there is a region with intermediate imbalance, before dropping rather quickly to zero. This is also illustrated by the zero-temperature curves in figure 5.3. Here, it is also clear that the size of the intermediate imbalance region increases with spin-orbit-coupling κ. We may see this in connection with the larger numerical uncertainty in the Monte-Carlo phase diagram of [100], although there, the system finds itself in the somewhat inhomogeneous stripe phase.

5.2.2 Finite temperature phase diagram

At finite temperature, we use equations (5.32) and (5.33) to determine the imbalance. Considering parameter values κ and λ at fixed density n_0, one may find μ as function of Δn_0 by incrementing μ until the right hand side of equation (5.32) is sufficiently close to the density we want. Equation (5.33) can then be considered an equation in the single variable Δn_0, which we solve by a combination of Newtons method and the bisection algorithm [126].

Choosing parameters $n_0 = 1$, $t = 1$, and $u = 2$ well inside the superfluid regime of the Bose-Hubbard model [104, 115, 120], we present the resulting phase diagrams in figure 5.2 at $\Delta\mu = 0.01$, while 5.3 shows cuts along different fixed values of κ.
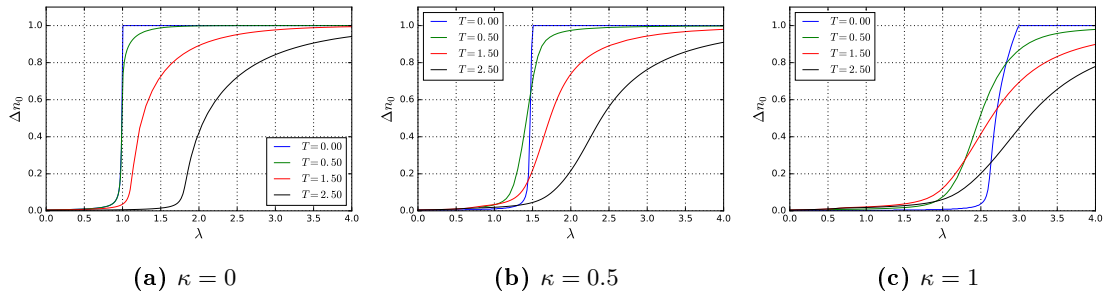
(a) $\kappa = 0$ **(b)** $\kappa = 0.5$ **(c)** $\kappa = 1$

Figure 5.3: Imbalance as function of relative intercomponent interaction at different values of κ. Each plot shows the imbalance at four different temperatures T. In the region with complete phase separation at $T = 0$, finite temperature reduces the imbalance from $\Delta n_0 / n_0 = 1$. With finite spin-orbit coupling, entropy driven phase separation causes imbalance to increase with temperature in the region with small imbalance at $T = 0$. Both κ and T are measured in units of the hopping amplitude t.

5.3 Entropy driven remixing and phase separation

In this section we discuss the obtained component imbalance phase diagrams at zero and finite temperature.

Considering the figures 5.2 and 5.3, at zero SOC, the phase separation transition occurs close to $\lambda = 1$, consistent with the continuum Gross-Pitaevskii prediction in section 3.3. The physical interpretation there applies here as well. With increasing SOC-strength κ, alignment of pseudo-spin with the effective magnetic field is an energetic asset the system is increasingly reluctant to give up. Spin-orbit coupling is not possible with only one component, and the phase separation transition therefore requires stronger inter- relative to intracomponent imbalance λ. This is the main physical mechanism behind the phase diagram in figure 5.2a.

The region with very large imbalance shrinks with temperature. This can be explained by entropic remixing. When minimizing the free energy $\Omega = U - TS$, a compromise between minimizing U and maximizing S must be reached, and the temperature T controls their relative importance. Being able to choose between different particle spin states gives additional freedom increasing the entropy. As a simple toy model, one may consider two identical, non-interacting particles with spin-$1/2$ in a two-state system. The two states can for instance represent two degenerate minima of a momentum dispersion relation. If the particles have the same spin, there are 3 different states, while for opposite spins, particle spin makes the two states with particles at different momenta distinct. In the thermodynamic limit, this effect becomes even more pronounced.

Examining the phase diagram in 5.3b and the imbalance curves in 5.3c more closely reveals also the opposite effect. There are parameter space regions where the imbalance increases with temperature. Comparing for instance the zero-temperature curve with the intermediate $T = 0.5$ curve at $\kappa = 1$ in 5.3c, from $\lambda = 0$ to approximately $\lambda = 2$, the intermediate temperature imbalance is significantly larger than at zero temperature. For $T = 0.5$, the phase separation transition takes place roughly between $\lambda = 2$ and $\lambda = 3$, while for zero temperature, the transition starts only around $\lambda = 2.5$.

This counter-intuitive phase separation can only be explained by an effect causing entropy to increase with imbalance, and which at small to moderate imbalances dominates the effect causing remixing. It can be understood by considering the behaviour of the dispersion relation (5.23) with Δ_0, which consists of the Zeeman splitting $\Delta\mu$ and imbalance Δn_0. Comparing with the continuum dispersion relation for Rashba SOC derived in chapter 3.3,

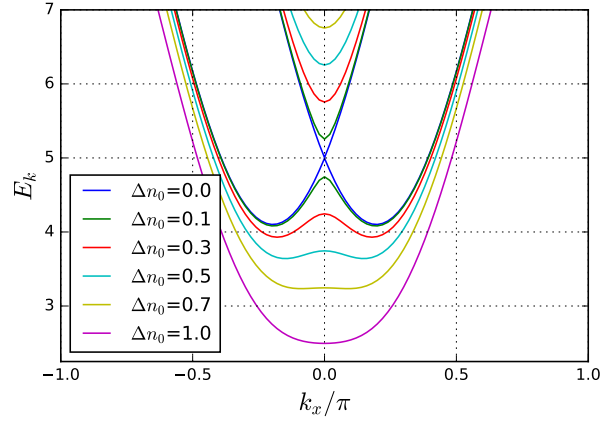$$E_{k\pm}^{\text{Cont.}} = \frac{k^2}{2m} \pm \sqrt{h^2 + \kappa^2 k^2}, \tag{5.47}$$

Figure 5.4: Dispersion relation along $k_x = k_y$ for a SOC BEC on an optical lattice with $\lambda = 3.5$ and $\kappa = 1$ at different values of the variational parameter Δn_0. At low temperature, the number of thermally accessible state increases with Δn_0, and this causes entropy driven phase separation.

one recognizes again that imbalance acts as an effective Zeeman splitting. The lattice dispersion relation is plotted along $k_x = k_y$ in figure 5.4, and is very similar to the continuum dispersion relation in figure 3.4c of chapter 3. At zero temperature, all particles reside in one of the minima. At small but finite temperature, only small regions around the minima are thermally accessible. Increasing the effective Zeeman field strength reduces the central maximum, and hence, the number of accessible states increases. The net result is that entropy increases with Δn_0, thus explaining entropy driven phase separation as an effect arising due to complex interplay between interaction and spin-orbit coupling.

In addition to the physical argument we gave earlier, the same line of reasoning can be applied to entropic remixing. In the phase-separated state, the dispersion relation has a single minimum, and reducing the imbalance flattens the region around this. Hence, the imbalance is reduced by finite temperature.

The characteristic imbalance $\Delta n_{k\alpha}$ in (5.2) can be used to explain entropic remixing and phase separation in a different manner. Equation (5.33) can be viewed as an average of $\Delta n_{k\alpha}$ weighted with Bose-Einstein distribution occupation numbers. All temperature effects are incorporated through changes in these weights. Characteristic imbalance can be plotted as function of position in **k**-space. This requires knowledge of Δn_0, which again requires us to solve equation (5.33). We can do this at some fixed value, for instance $T = 0$. The additional imbalance induced by a small change in temperature must then be compensated for by a slight change on the left hand side of the equation, which becomes the change in total imbalance. The lower band characteristic imbalance is plotted for $\kappa = 1$ and different values of λ along $k_x = k_y$ in figure 5.5. The total imbalance Δn_0 is calculated at zero temperature and increases with λ, as shown in the right panel. As we have already shown, whenever $\sin k_x = \sin k_y = 0$, the characteristic imbalance reaches its maximum value 1. For zero temperature, complete phase separation is reached approximately at $\lambda = 3.0$. In this regime, there is a rather large characteristic imbalance across the entire Brillouin zone. The dispersion relation minimum is at **k** = 0, and at zero temperature, all particles are condensed here. Upon increasing the temperature, particles go out in the states around **k** = 0 with lower characteristic imbalance. Therefore, total imbalance is reduced, and this is entropic remixing. In the mixed regime of parameter space, characteristic imbalance is small except for the sharp peak at **k** = 0. The minimum sits in a state at finite k with low characteristic imbalance. Upon increasing the temperature, states around the minima become occupied. A resulting significant contribution from the central peak explains entropy driven phase separation.
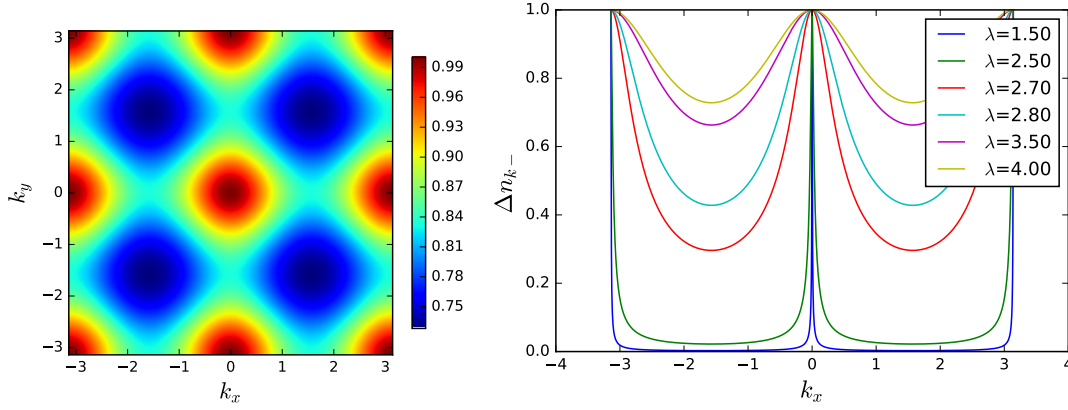
Figure 5.5: Characteristic imbalance Δn_{k-} as function quasimomentum with total imbalance determined from the self-consistent equation with $T = 0$ at $\kappa = 1$. Left panel: Imbalance in the first Brillouin zone at $\lambda = 4$. Right panel: Imbalance at various λ along $k_x = k_y$.

Both explanations of the finite temperature effects provide nice perspectives on the physics of the transition. Especially interesting is the counter-intuitive entropy driven phase separation occurring due to complex interplay between the interaction and spin-orbit coupling. There is competition between the energy and entropy terms in the free energy, spin-orbit coupling and interaction in the energy term, and effects causing entropy driven phase separation and remixing in the entropy term. The observed phase transition should therefore be regarded highly non-trivial even at mean field level.

Chapter 6

Strong coupling

In the strongly coupled regime, interaction dominates hopping from the kinetic and spin-orbit coupling terms of the Hamiltonian. The ground state is therefore a Mott insulator characterized by localization of each particle at a given lattice site, as discussed in section 4.3. For small but finite hopping amplitude in the case of electrons without spin-orbit coupling, a well known calculation reveals an antiferromagnetic Heisenberg model describing the interaction between spins at neighbouring lattice sites [127, 128]. In the same spirit, we here derive[1] a spin model describing magnetic textures in the Mott insulator of the spin-orbit coupled Bose-Hubbard model. The result is an anisotropic Heisenberg model with an additional Dzyaloshinskii-Moriya interaction [130, 131] giving rise to complex magnetic textures. Based on classical Monte-Carlo simulations in the literature [102, 104, 129], we aim at reconstructing the phase diagram with a variational approach. Finally, we use Holstein-Primakoff transformation and spin wave expansion to analyse the effect of quantum fluctuations.

6.1 Perturbation theory

In the strong coupling limit, the hopping terms can be considered small compared to the interaction. Our approach is therefore perturbation theory in the kinetic and SOC terms. We also assume half-filling, which is one atom per lattice site

The unperturbed Hamiltonian H_0 and the perturbation H_{hop} are

$$H_0 = \frac{1}{2} \sum_{i,\sigma\sigma'} u_{\sigma\sigma'} n_{i\sigma}(n_{i\sigma'} - \delta_{\sigma\sigma'}) \tag{6.1}$$

$$H_{\mathrm{hop}} = \sum_{\langle ij\rangle,\sigma\sigma'} t_{ij}^{\sigma\sigma'} a_{i\sigma}^{\dagger} a_{j\sigma'}, \tag{6.2}$$

where the matrix t_{ij} follows from the Hamiltonian (4.25).

To zeroth order, the energy eigenstates of H_0 are Mott insulating states. The ground state has exactly one boson per lattice site, since this minimizes boson interactions. Spin is irrelevant, and the ground state is therefore 2^N-fold degenerate. As we will see, this degeneracy is lifted when we go to second order perturbation theory. Our goal is to determine how this happens.

For a given ground state $|\psi_0\rangle$ of the non-perturbed Hamiltonian, the first order energy correction is

---

[1] After completing the calculations, we became aware of articles arriving at variants of the same spin model [102, 104, 129], and a review article presenting a similar derivation in more detail [93]. We go through the derivation in our original notation, before adopting the notation of [104] for easier comparison with literature.

$$\Delta E^1 = \langle \psi_0 | H_{\text{hop}} | \psi_0 \rangle . \tag{6.3}$$

The perturbation H_{hop} consists of terms proportional to $a_{i\sigma}^\dagger a_{j\sigma'}$, where i and j are nearest neighbours. Since eigenstates are orthogonal, $b_{i\alpha} | \psi_0 \rangle$ and $b_{j\beta} | \psi_0 \rangle$ must have zero overlap, and therefore

$$\Delta E^1 = 0. \tag{6.4}$$

To obtain non-degenerate ground states, one therefore has to go to second order. Here, the energy correction is

$$\Delta E^2 = \sum_n \frac{\langle \psi_0 | H_{\text{hop}} | n \rangle \langle n | H_{\text{hop}} | \psi_0 \rangle}{E_0 - E_n}, \tag{6.5}$$

where $\{|n\rangle\}$ denotes the set of excited eigenstates with energies E_n for the unperturbed Hamiltonian H_0, while E_0 is the ground state energy. To give a non-zero contribution, $|n\rangle$ must have non-zero overlap with $H_{\text{hop}} | \psi_0 \rangle$. Since the terms in H_{hop} make one particle jump to a neighbouring lattice site, $|n\rangle$ must have one single doubly occupied lattice site with an empty neighbour, and otherwise one atom per site. We divide such states $|n\rangle$ into two groups. In the same species subspace (s-subspace), the doubly occupied lattice site holds particles of the same species, while in the different species subspace (d-subspace), the two atoms are of different species. Let $\{|n_s\rangle\}$ and $\{|n_d\rangle\}$ denote the subsets of $\{|n\rangle\}$ with states belonging to the s and d subspaces. In the first case, the unperturbed excited eigenenergy is $u_s = u_{\uparrow\uparrow} = u_{\downarrow\downarrow} = u$, while in the second, it is $u_d = u_{\uparrow\downarrow} = u_{\downarrow\uparrow} = \lambda u$. We then obtain

$$\Delta E^2 = -\frac{1}{u} \sum_{n_s} \langle \psi_0 | H_{\text{hop}} | n_s \rangle \langle n_s | H_{\text{hop}} | \psi_0 \rangle - \frac{1}{\lambda u} \sum_{n_d} \langle \psi_0 | H_{\text{hop}} | n_d \rangle \langle n_d | H_{\text{hop}} | \psi_0 \rangle. \tag{6.6}$$

$$\tag{6.7}$$

This can be written as $\Delta E^2 = \langle \psi_0 | H_{\text{eff}} | \psi_0 \rangle$ with effective Hamiltonian

$$H_{\text{eff}} = H_{\text{eff}}^s + H_{\text{eff}}^d = -\frac{1}{u} H_{\text{hop}} P_s H_{\text{hop}} - \frac{1}{\lambda u} H_{\text{hop}} P_d H_{\text{hop}} \tag{6.8}$$

by introducing operators P_s and P_d projecting states down on the s and d subspaces. Since we are interested in the second order correction to the energy, we are interested only in how the effective Hamiltonian acts on the ground states $| \psi_0 \rangle$. This allows certain simplifications, which we utilize in the following. In the rest of this derivation, equality of operators therefore means acting in the same way on the subspace we are considering.

By inserting the perturbation, the effective Hamiltonian H_{eff}^r corresponding to subspace $r \in \{s, d\}$ becomes

$$H_{\text{eff}}^r = -\frac{1}{u_r} \sum_{\langle ij \rangle \alpha\beta} \sum_{\langle kl \rangle \gamma\delta} t_{ij}^{\alpha\beta} t_{kl}^{\gamma\delta} a_{i\alpha}^\dagger a_{j\beta} P_r a_{k\gamma}^\dagger a_{l\delta}. \tag{6.9}$$

To obtain finite energy correction, $H_{\text{eff}} | \psi_0 \rangle$ must still be a state with one particle per lattice site. This gives requirements $i = l$ and $j = k$. Splitting the hopping matrix $t_{ij}^{\alpha\beta}$ according to

$$t_{ij}^{\alpha\beta} = -\delta_{\alpha\beta} \, t + \delta_{\alpha,-\beta} \, s_{ij}^{\alpha\beta} \tag{6.10}$$

and inserting in the above Hamiltonian, we get

$$H_{\text{eff}}^r = -\frac{1}{u_r} \sum_{\langle ij \rangle \, \alpha\beta\gamma\delta} \left[-\delta_{\alpha\beta} t + \delta_{\alpha,-\beta} s_{ij}^{\alpha\beta} \right] \left[-\delta_{\gamma\delta} t + \delta_{\gamma,-\delta} s_{ji}^{\gamma\delta} \right] a_{i\alpha}^\dagger a_{j\beta} P_r a_{j\gamma}^\dagger a_{i\delta}. \tag{6.11}$$

Acting on a ground state for the unperturbed system, the operator $a_{j\gamma}^\dagger a_{i\delta}$ gives a state with an additional boson of type γ at position j. Depending on the type of boson at j in the state $|\psi_0\rangle$, the projection operator may either allow or prohibit this. We can therefore write

$$a_{i\alpha}^\dagger a_{j\beta} P_d a_{j\gamma}^\dagger a_{i\delta} = a_{i\alpha}^\dagger a_{j\beta} a_{j\gamma}^\dagger a_{i\delta}(1 - n_{j\gamma}) \quad = a_{i\alpha}^\dagger a_{i\delta}(\delta_{\beta\gamma} + a_{j\gamma}^\dagger a_{j\beta})n_{j,-\gamma} \tag{6.12}$$

$$a_{i\alpha}^\dagger a_{j\beta} P_s a_{j\gamma}^\dagger a_{i\delta} = a_{i\alpha}^\dagger a_{j\beta} a_{j\gamma}^\dagger a_{i\delta}(1 - n_{j,-\gamma}) = a_{i\alpha}^\dagger a_{i\delta}(\delta_{\beta\gamma} + a_{j\gamma}^\dagger a_{j\beta})n_{j\gamma}, \tag{6.13}$$

where we have used that there is only one boson per lattice site in the ground state, and where we the operators are grouped according to lattice site. The two operators acting on neighbouring local two-state Hilbert spaces can then be represented by Pauli matrices, giving rise to a nearest neighbour effective spin Hamiltonian. To do this, we have to rewrite operators of the form $a_{i\alpha}^\dagger a_{i\beta} a_{j\gamma}^\dagger a_{j\delta} n_{j\epsilon}$. Introduce short-hand notation

$$|\alpha\beta|\gamma\delta, \epsilon| = a_{i\alpha}^\dagger a_{i\beta} a_{j\gamma}^\dagger a_{j\delta} n_{j\epsilon}, \tag{6.14}$$

and associate the pseudo-spin states with column vectors according to

$$|\uparrow\rangle = \begin{pmatrix} 1 \\ 0 \end{pmatrix}, \qquad |\downarrow\rangle = \begin{pmatrix} 0 \\ 1 \end{pmatrix}. \tag{6.15}$$

By comparing the effect of boson operators on the two-state pseudo-spin Hilbert space with that of Pauli matrices on the column vectors, we get

$$| \uparrow\uparrow | = \frac{1}{2}(1 + \sigma^z) \qquad\qquad | \uparrow\downarrow | = \frac{1}{2}\sigma^+$$

$$| \downarrow\downarrow | = \frac{1}{2}(1 - \sigma^z) \qquad\qquad | \downarrow\uparrow | = \frac{1}{2}\sigma^-.$$

Similarly for the operators at lattice site j gives

$$| \uparrow\uparrow,\downarrow | = | \downarrow\downarrow,\uparrow | = 0 \qquad | \uparrow\uparrow,\uparrow | = \frac{1}{2}(1 + \sigma^z) \qquad | \uparrow\downarrow,\downarrow | = \frac{1}{2}\sigma^+$$

$$| \downarrow\uparrow,\downarrow | = | \uparrow\downarrow,\uparrow | = 0 \qquad | \downarrow\downarrow,\downarrow | = \frac{1}{2}(1 - \sigma^z) \qquad | \downarrow\uparrow,\uparrow | = \frac{1}{2}\sigma^-.$$

In addition to the two subspaces we have already introduced, we can group the terms in the Hamiltonian according to physical origin:

- tt: Two regular hoppings

- ss: Two hoppings with spin-flip

- ts: One regular hopping and one with spin-flip

Finding the spin model is now a little tedious, but in the end simply a matter of writing out all the terms in (6.11), replacing boson operators with Pauli-matrices according to the dictionary above, and expressing the operators σ^+ and σ^- in terms of the x- and y-components. This is deferred to appendix A, and the final results for the effective Hamiltonians H_{eff}^s and H_{eff}^d are

Table 6.1: Effective spin model coefficients in equation (6.18) for general linear combination of Rashba and Dresselhaus SOC on the form $H_{\mathrm{SOC}} \propto \eta\sigma_x k_y + \kappa\sigma_y k_x$.

$J_x^x = -4(t^2 - \kappa^2)/\lambda u$	$J_y^x = -4(t^2 + \eta^2)/\lambda u$
$J_x^y = -4(t^2 + \kappa^2)/\lambda u$	$J_y^y = -4(t^2 - \eta^2)/\lambda u$
$J_x^z = -4(t^2 - \kappa^2)(2\lambda - 1)/\lambda u$	$J_y^z = -4(t^2 - \eta^2)(2\lambda - 1)/\lambda u$
$\mathbf{D}_x = -4(2t\kappa/u)\hat{y}$	$\mathbf{D}_y = -4(2t\eta/u)\hat{x}$

Table 6.2: Spin model coefficients for equation (6.18) in units of $(4t_0^2/\lambda u)$ for Rashba spin-orbit coupling $H_{\mathrm{SOC}} \propto \sigma_x k_y - \sigma_y k_x$ in the notation of [104].

$J_x^x = -\cos 2\alpha$	$J_y^x = -1$
$J_x^y = -1$	$J_y^y = -\cos 2\alpha$
$J_x^z = -(2\lambda - 1)\cos 2\alpha$	$J_y^z = -(2\lambda - 1)\cos 2\alpha$
$\mathbf{D}_x = \lambda \sin 2\alpha(-\hat{y})$	$\mathbf{D}_y = \lambda \sin 2\alpha(+\hat{x})$

$$
\begin{aligned}
H_{\mathrm{eff}}^d = &- \frac{t^2}{\lambda u} \sum_{i,\delta} \left(1 - \sigma_i^z \sigma_{i+\delta}^z + \sigma_i^x \sigma_{i+\delta}^x + \sigma_i^y \sigma_{i+\delta}^y\right) - \frac{1}{\lambda u} \sum_{i,\delta} |s_\delta|^2 (1 + \sigma_i^z \sigma_{i+\delta}^z) \\
&+ \frac{1}{\lambda u} \sum_{i,\delta} \left[\, \mathrm{Re}(s_\delta^2)(\sigma_i^x \sigma_{i+\delta}^x - \sigma_i^y \sigma_{i+\delta}^y) - \mathrm{Im}(s_\delta^2)(\sigma_i^x \sigma_{i+\delta}^y + \sigma_i^y \sigma_{i+\delta}^x)\right]
\end{aligned}
\tag{6.16}
$$

$$
H_{\mathrm{eff}}^s = - \frac{2}{u} \sum_{i,\delta} \left[(t^2 - |s_\delta|^2)\sigma_i^z \sigma_{i+\delta}^z - t\,\mathrm{Re}(s_\delta)\hat{y} \cdot \vec{\sigma}_i \times \vec{\sigma}_{i+\delta} - t\,\mathrm{Im}(s_\delta)\hat{x} \cdot \vec{\sigma}_i \times \vec{\sigma}_{i+\delta}\right]
\tag{6.17}
$$

If we choose the spin-orbit coupling matrix $\beta_{l\delta}$ to be either diagonal or off-diagonal, s_δ becomes real or purely imaginary. Hence, the term with coupling between the x- and y-components of the spin disappears, and as in [104], we can write the effective spin Hamiltonian as

$$
H_{\mathrm{eff}} = \sum_{i,\delta} \left\{ \sum_{a=x,y,z} J_\delta^a S_i^a S_{i+\delta}^a + \mathbf{D}_\delta \cdot (\mathbf{S}_i \times \mathbf{S}_{i+\delta}) \right\},
\tag{6.18}
$$

with couplings J_δ^a and $\mathbf{D}_\delta$ depending on t and s_δ, and where $\mathbf{S} = \vec{\sigma}/2$. In terms of the spin-orbit coupling matrix elements κ and η, the above parameters take the values in table 6.1.

In the rest of this chapter, we focus on Rashba SOC with $\eta = -\kappa$ and use the notation of Ref. [104] introduced in section 4.2.2, where

$$
t = t_0 \cos \alpha \qquad \kappa = t_0 \sin \alpha.
\tag{6.19}
$$

One advantage is that when plotting the spin model phase diagram, one can consider arbitrary ratios of κ/t. One may now rewrite the Heisenberg couplings and Dzyaloshinskii-Moriya strengths in table 6.1 using $t^2 - \kappa^2 = t_0^2 \cos 2\alpha$, $t^2 + \kappa^2 = t_0^2$, and $2t\kappa = t_0^2 \sin 2\alpha$. This gives the spin model coefficients in table 6.2.

6.1.1   Physical origin of spin model terms

In this section, we describe some qualitative features of the spin model we have derived. The model consists of an anisotropic Heisenberg term and a cross product term known as the Dzyaloshinskii-

Moriya interaction. We consider the Heisenberg term first.

The effective Hamiltonian is constructed using second-order perturbation theory, for which the energy correction is always negative. Hence, all possible hopping processes are energetically favourable. Considering the d-subspace effective Hamiltonian in (6.16), the coefficient of the term $t^2\sigma_i^z\sigma_j^z/u$ is antiferromagnetic since tt-processes via the d-subspace are only possible at every link for antiferromagnetic ordering. Similarly, we argue that the coefficient of the z-direction Heisenberg coupling from ss-processes is ferromagnetic, and analogously for the s-subspace terms.

The Dzyaloshinskii-Moriya term in general takes the form $\mathbf{D}_\delta \cdot \mathbf{S}_i \times \mathbf{S}_{i+\delta}$. Based on symmetry arguments, it was first proposed by Dzyaloshinskii in 1958 to explain weak ferromagnetism in antiferromagnets [26, 132]. T. Moriya later showed that it can be generated by SOC [131]. In our calculation, it is clear that since the coupling strength is $2\kappa t/u$, the physical origin is virtual hopping processes with one regular spin-conserving hopping and one SOC-induced spin-flip hopping via the s-subspace. While the Heisenberg term typically prefers ferromagnetic or antiferromagnetic alignment, the Dzyaloshinskii-Moriya interaction prefers a spiral phase with orthogonal nearest neighbour spins. The competition between these different preferences is the origin of the complex magnetic phases we discuss in the next section.

An analogous spin model can also be derived for fermions [102]. Due to the Pauli principle, there is no equivalent of the s-subspace in this calculation. In the bosonic case, we can impose an effective Pauli principle by letting $\lambda \to 0$ with λu fixed. The Dzyaloshinskii-Moriya interaction is then suppressed by the huge interaction energy between atoms of the same species. One might therefore think there is no Dzyaloshinskii-Moriya interaction for fermions, but it is in fact present [102] because fermions satisfy anti-commutation relations instead of commutation relations. A similar observation is that in the d-subspace Hamiltonian without SOC, we get ferromagnetic coupling in the xy-plane, but antiferromagnetic coupling in the z-direction. The fermion model gives an isotropic ferromagnetic Heisenberg model [102]. This is again because fermions satisfy anti-commutation relations. From these observations, we infer that the boson model shares more features with the fermion model for $\lambda = 1$ than for the effective Pauli principle.

6.1.2 Fourier representation of Hamiltonian

Before discussing the magnetic texture phase diagram, we derive the Fourier representation of the Hamiltonian. Introduce Fourier and inverse Fourier transforms

$$\mathbf{S}_q = \frac{1}{\sqrt{N}}\sum_i \mathbf{S}_i e^{i\mathbf{q}\cdot\mathbf{r}_i} \tag{6.20}$$

$$\mathbf{S}_i = \frac{1}{\sqrt{N}}\sum_q \mathbf{S}_q e^{-i\mathbf{q}\cdot\mathbf{r}_i}, \tag{6.21}$$

where we will occasionally refer to $S_q = |\mathbf{S}_q|$ as the magnetic structure factor. Inserting these expressions in the Hamiltonian (6.18), using the usual delta function identity (5.12) and introducing a structure factor

$$\eta_q^a = \sum_\delta J_\delta^a \cos q_\delta, \tag{6.22}$$

we get Hamiltonian

$$H = \sum_q \left\{ \sum_a \eta_q^a S_q^a S_{-q}^a + \sum_\delta \sin q_\delta \, \mathbf{D}_\delta \cdot i\mathbf{S}_q \times \mathbf{S}_{-q} \right\}. \tag{6.23}$$

It follows from the anti-symmetry of the cross product that $\mathbf{S}_q \times \mathbf{S}_q^*$ is purely imaginary, and since $\mathbf{S}_{-q} = \mathbf{S}_q^*$, the energy stays real.
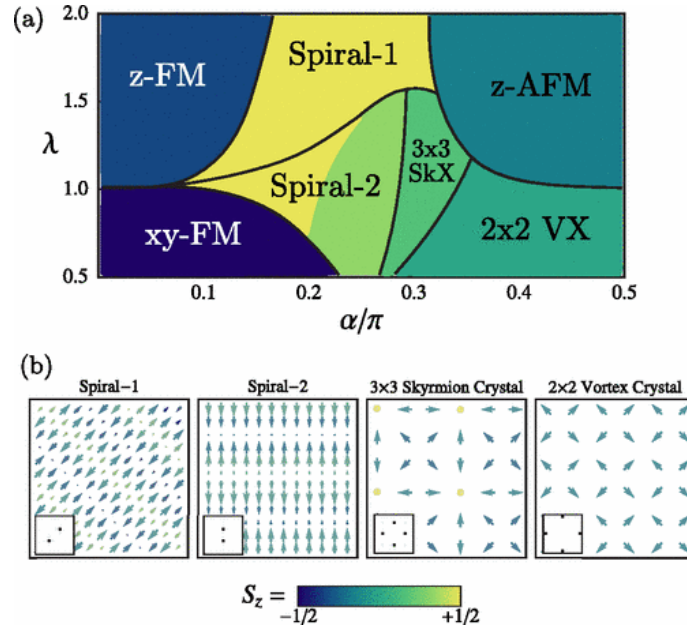
Figure 6.1: Panel (a) shows the Monte-Carlo phase diagram of Ref. [104] for the classical spin model with Rashba SOC and component-dependent interaction. Panel (b) shows some of the various non-trivial classical ground states in the system, while the inset shows the maximum of the magnetic structure factor for each of these phases. (Reprinted with permission from W.S. Cole, S. Zhang, A. Paramekanti, and N. Trivedi, Phys. Rev. Lett. 109 (2012). Copyright (2012) by the American Physical Society.)

6.2   Classical ground state phase diagram

Our goal is now to analyse the spin structure of the ground state for the effective Hamiltonian (6.18). This corresponds to the spatial structure of the two boson species. The problem has been studied in several papers using classical Monte-Carlo simulations, and we consider these in more detail below. In section 6.4, we show that quantum fluctuations can be important. Therefore, we cannot expect a classical approach reproduce the phase diagram very accurately, but it is nevertheless a good starting point for the quantum treatment. Radić *et al.* [129] studied the model at general linear-combinations of Rashba and Dresselhaus SOC, but with spin-independent interaction corresponding to $\lambda = 1$. In a paper by Gong *et al.* [102], results are presented for spin-independent interaction, Rashba SOC, and a Zeeman field. Cole *et al.* [104] studied the model for Rashba spin-orbit coupling and spin-dependent interaction. The resulting phase diagrams show a plethora of different classical ground states obtained for a finite lattice. In the rest of the chapter, we study in particular the phase diagram of the latter paper, which is reprinted in figure 6.1. In this section, we give a description of the phases in this diagram based on the article, but leave discussion of the physical mechanisms behind to section 6.3.5.

The zFM and zAFM states are regular ferromagnetic and antiferromagnetic states with ordering in the pseudo-spin z-direction. The classical xyFM-state has spin space ferromagnetic ordering with arbitrary orientation in the xy-plane. The less trivial states are illustrated in panel (b) of figure 6.1. In the spiral-1 (S1) phase, spins spiral in the plane spanned by $\hat{z}$ and $\hat{x} \pm \hat{y}$ with an incommensurate (IC) wave vector $\mathbf{q} = (q, \pm q)$ for some q. For the spiral-2 (S2) phases, spins instead spiral in the $\hat{z}$-$\hat{y}$ or $\hat{z}$-$\hat{x}$ planes, now with wavevector $\mathbf{q} = (q, 0)$ or $(0, q)$. The light green region in the phase diagram corresponds to a spiral-2 phase with commensurate $q = \pi/2$, or equivalently period 4.

The vortex is a topologically protected configuration known from spin systems such as the XY-model, and at heart of the celebrated Kosterlitz-Thouless phase transition [40, 133]. Here, it

appears as a commensurate 2x2 crystal phase (2x2 VX) in the xy-plane, as shown in panel (b) of figure 6.1. In the next section, we show that classically, the vortex phase is continuously degenerate with a set of states we will refer to as the vortex family.

The skyrmion (Sk) is yet another topologically protected configuration. It was first proposed by Skyrme as a model for hadrons [134], but later shown to be of relevance also in condensed matter systems [41]. In the classical simulations of Ref. [104], it occurs as a skyrmion crystal (SkX) of size 3x3.

6.3 Variational approach

In this section, we analyse the phase diagram of the effective spin model (6.18) with a variational approach. In Ref. [104], Monte-Carlo simulations were compared with energies of variational states for the zFM, zAFM, xyFM, 2x2 VX, 4x1 S2, and skyrmion phases, but not for the incommensurate spiral-1 and spiral-2 phases. We provide calculations for all these phases in addition to a commensurate 6x1 spiral-2 phase (6x1 S2). For the zFM, zAFM, xyFM, and vortex family states, we arrive at exact results. We obtain also an exact expression for the commensurate 4x1 spiral-2 phase, while for the incommensurate spiral-1 and spiral-2 phases, we obtain analytical expressions in the single-mode approximation. For the 6x1 S2 phase and the skyrmion phase, we minimize the energy numerically with respect to a small set of variational parameters. We also discuss physical mechanisms behind the phase diagram. As a starting point for this, one may consider the model in limits such as $\alpha = 0$, $\alpha = \pi/2$, $\lambda \to 0$ and $\lambda \to \infty$ [102, 104, 118, 135].

The variational energies in this section are purely classical. In section 6.4 we consider also the effect of quantum fluctuations.

6.3.1 Ferromagnetic and antiferromagnetic phases

For the classical zFM phase, all spins are aligned in the z-direction, $\mathbf{S}_i = S\hat{z}$. We insert this in the Hamiltonian (6.18). Since the state is uniform, the cross product between neighbouring spins is zero, so the Dzyaloshinskii-Moriya term does not contribute to the ground state energy. The energy therefore becomes

$$E_{\text{zFM}} = 2NS^2 J^z = -2NS^2 \left(\frac{4t_0^2}{\lambda u}\right)(2\lambda - 1)\cos 2\alpha. \tag{6.24}$$

For the zAFM phase, again, there is no contribution from the Dzyaloshinskii-Moriya term. Since neighbouring spins are oriented in opposite directions, we get

$$E_{\text{zAFM}} = -E_{\text{zFM}} = 2NS^2 \left(\frac{4t_0^2}{\lambda u}\right)(2\lambda - 1)\cos 2\alpha. \tag{6.25}$$

As shown in figure 6.2a, the xy-ferromagnetic state can be represented as $\mathbf{S}_i = S(\cos\phi, \sin\phi, 0)$, where ϕ is the angle between the x-axis and the direction of ferromagnetic ordering. The Dzyaloshinskii-Moriya term is still zero because spins are parallel. Inserting the spins in the Hamiltonian and using $J_x^x + J_y^x = J_y^x + J_y^y$, the classical xyFM-state is continuously degenerate with energy

$$E_{\text{xyFM}} = -NS^2 \left(\frac{4t_0^2}{\lambda u}\right)(1 + \cos 2\alpha). \tag{6.26}$$

6.3.2 Vortex and stripe phases

A similar continuous degeneracy exists for the 2x2 vortex state in figure 6.2b. To show this, consider the state illustrated in figure 6.2c, where spins are rotated with angle θ on one of the two
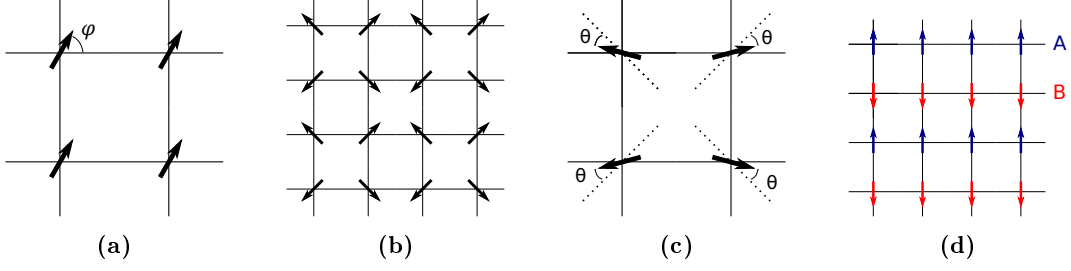
Figure 6.2: Magnetic phases in the xy-plane. The xyFM state in (a) has an arbitrary ordering angle ϕ with the x-axis. Figure (b) shows the vortex phase, while (c) shows state in the vortex family characterized by rotation with angle θ on one chessboard sublattice and angle $-\theta$ on the other. By setting $\theta = -\pi/4$, we obtain the stripe phase in (d), which can be decomposed in two sublattices A and B with opposite magnetic ordering.

chessboard sublattices, and with angle $-\theta$ on the other. We now calculate the energy of this state. The four spins $\mathbf{S}_i$ are characterized by angles ϕ_i, and after the θ-rotation, these are

$$\phi_1 = 3\pi/4 + \theta \qquad \phi_2 = \pi/4 - \theta \qquad \phi_3 = -3\pi/4 - \theta \qquad \phi_4 = -\pi/4 - \theta. \qquad (6.27)$$

This can be expressed as $\phi_{i+\hat{x}} = -\phi_i + \pi$ and $\phi_{i+\hat{y}} = -\phi_i$. Just like the Dzyaloshinskii-Moriya vectors, the spins of a vortex family state lie in the xy-plane. Therefore, only the Heisenberg term contributes to the classical ground state energy, which becomes

$$E_{\mathrm{VX}} = \sum_{i,\delta} \left\{ \sum_a J_\delta^a S_i^a S_{i+\delta}^a \right\} = \sum_{i,\delta} \left\{ J_\delta^x \cos\phi_i \cos\phi_{i+\hat{x}} + J_\delta^y \cos\phi_i \cos\phi_{i+\hat{y}} \right\}. \qquad (6.28)$$

Inserting the relations between ϕ_i and $\phi_{i+\delta}$ gives total energy

$$E_{\mathrm{VX}} = S^2 \sum_i \left(-J_x^x \cos^2\phi_i + J_x^y \sin^2\phi_i + J_y^x \cos^2\phi_i - J_y^y \sin^2\phi_i \right). \qquad (6.29)$$

Using $J_x^x = J_y^y$ and $J_x^y = J_y^x$, the angle ϕ_i disappears. In terms of Bose-Hubbard model parameters, we then get classical continuously degenerate energy

$$E_{\mathrm{VX}} = -NS^2 \left(\frac{4t_0^2}{\lambda u} \right) (1 - \cos 2\alpha). \qquad (6.30)$$

In the Monte-Carlo simulations of [104], the only state showing up is the vortex phase characterized by $\theta = 0$. They propose that this is due to finite temperature effects. The article [129] claims that the stripe phase dominates due to small deviations from perfect Rashba SOC. Classically, both effects may be of relevance, but as discussed in section 6.4.5, classical degeneracy is broken by quantum fluctuations in favour of the stripe phase shown in figure 6.2d and characterized by $\theta = \pm\pi/4$.

6.3.3   Spiral phases

The spirals can be divided into commensurate and incommensurate phases. For the commensurate phases, based on physical intuition, we propose variational states with a small set of variational parameters. We then calculate their energies in real space, before minimizing analytically (4x1 S2) or numerically (6x1 S2). For the incommensurate phases, we instead use the Fourier transformed Hamiltonian (6.23) in the single-mode approximation, using wave vector as variational parameter.
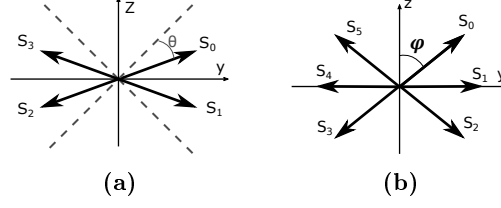
Figure 6.3: Spin orientiations $\mathbf{S}_i$ for the (a) 4x1 (b) and 6x1 spiral-2 phase variational states.

Commensurate 4x1 spiral-2 phase

The commensurate 4x1 spiral-2 phase is a state spiralling with periodicity 4 in the $\hat{y}$-$\hat{z}$-plane or $\hat{x}$-$\hat{z}$-plane. We choose the former, and can therefore write the state as

$$\mathbf{S}_{n\hat{x}+m\hat{y}} \equiv \mathbf{S}_{m\%4}, \tag{6.31}$$

where %4 denotes modulo 4. The most general 4x1 spiral-2 phase is therefore $\mathbf{S}_i = \hat{y}\sin\phi_i + \hat{z}\cos\phi_i$, described by four angles ϕ_i. We restrict ourselves to the Ansatz

$$\phi_0 = \pi/4 - \theta \qquad \phi_1 = -\pi/4 + \theta \qquad \phi_2 = -3\pi/4 - \theta \qquad \phi_3 = 3\pi/4 + \theta, \tag{6.32}$$

as illustrated in figure 6.3a. The physical motivation is the difference between the magnitudes of the Heisenberg couplings J_x^y and J_x^z. It may therefore be energetically favourable to twist spins toward either the y- or z-direction, even if the Dzyaloshinskii-Moriya term is dominant in the spiral-2 phase region. Since here, the coupling J_x^y is always ferromagnetic and typically stronger than J^z, the angle θ is usually positive.

For the above variational state, we now derive an expression for the energy. The Heisenberg coupling between the spins $\mathbf{S}_0$ and $\mathbf{S}_1$ cancels exactly the coupling between $\mathbf{S}_1$ and $\mathbf{S}_2$, but there is still Heisenberg coupling between the ferromagnetically aligned neighbouring spins in $\hat{x}$-direction. Total energy is therefore

$$E_{4\text{x1S2}} = -\left(\frac{4t_0^2}{\lambda u}\right)\frac{N}{4}\sum_{i=1,2,3,4}\left\{S_i^y S_{i+\hat{x}}^y + (2\lambda-1)\cos 2\alpha\, S_i^z S_{i+\hat{x}}^z + \lambda\sin 2\alpha(-\hat{x})\cdot\mathbf{S}_i\times\mathbf{S}_{i+\hat{y}}\right\} \tag{6.33}$$

$$= -NS^2\left(\frac{4t_0^2}{\lambda u}\right)\left\{\frac{1}{2}\left[1+(2\lambda-1)\cos 2\alpha\right] + \frac{1}{2}\left[1-(2\lambda-1)\cos 2\alpha\right]\sin 2\theta + \lambda\sin 2\alpha\cos 2\theta\right\} \tag{6.34}$$

We now minimize with respect to θ. Since the coefficient in front of $\sin 2\theta$ is positive, we get $\theta > 0$, as already predicted. The extrema of an expression on the form $A\sin x + B\cos x$ are given by $\tan x = A/B$. Inserting this back into the expression we want to minimize gives $\sqrt{A^2+B^2}$. We are then left with energy

$$E_{4\text{x1S2}} = -NS^2\left(\frac{4t_0^2}{\lambda u}\right)\left\{\frac{1}{2}\left[1+(2\lambda-1)\cos 2\alpha\right] + \sqrt{\frac{1}{4}\left[1-(2\lambda-1)\cos 2\alpha\right]^2 + \lambda^2\sin^2 2\alpha}\right\} \tag{6.35}$$

for the commensurate 4x1 spiral-2 phase. When Fourier-transforming this state, due to the periodicity, we can only have non-zero Fourier components at $q_y \in \{0, \pm\pi/2, \pi\}$ inside the first Brillouin zone. By considering each of these points separately, the Fourier transform becomes

$$\mathbf{S}_q = \delta_{\mathbf{q},\pi/2\hat{y}}\frac{NS}{2}\big(|S_0^y|(1+i)\hat{y} + (1-i)|S_0^z|\hat{z}\big), \tag{6.36}$$

where $|S_0^y|$ and $|S_0^z|$ are given by the minimization procedure. One may now insert this in the Fourier transform of the Hamiltonian in (6.23) and check that one obtains the same energy.

Commensurate 6x1 spiral-2

A similar calculation can be performed for the 6x1 commensurate spiral-2. We start with the variational state illustrated in figure 6.3b. The energy becomes

$$E_{\text{6x1S2}} = \frac{N}{6}\sum_{i=0,\dots,5}\big\{ J_x^y S_i^y S_{i+\hat{x}}^y + J_x^z S_i^z S_{i+\hat{x}}^z + J_y^y S_i^y S_{i+\hat{y}} + J_y^z S_i^z S_{i+\hat{y}}^z + \mathcal{D}\hat{x}\cdot\mathbf{S}_i\times\mathbf{S}_{i+\hat{y}}\big\}, \tag{6.37}$$

where $\mathcal{D} = (4t_0^2/\lambda u)\lambda\sin 2\alpha$ is the strength of the Dzyaloshinskii-Moriya interaction. Inserting the spins, one obtains

$$E_{\text{6x1S2}} = -NS^2\left(\frac{4t_0^2}{\lambda u}\right)\frac{1}{6}\big[2 + (4 - 2\cos 2\alpha)\sin^2\phi_0 + 6(2\lambda-1)\cos 2\alpha\cos^2\phi_0 \tag{6.38}$$

$$+ 4\cos 2\alpha\sin\phi_0 + 2\lambda\sin 2\alpha\sin 2\phi_0 + 4\lambda\sin 2\alpha\cos\phi_0\big]. \tag{6.39}$$

At any given point in parameter space, we minimize this with respect to ϕ_0, and obtain the 6x1 spiral-2 phase energy.

Performing the Fourier transform of the phase gives

$$\mathbf{S}_{q=\pi\hat{y}} = \frac{\sqrt{N}S}{3}(2\sin\phi_0 - 1)\hat{y} \tag{6.40}$$

$$\mathbf{S}_{q=\pi/3\hat{y}} = \frac{\sqrt{N}S}{3}\big\{(3/2 - \sqrt{3}i/2)\cos\phi_0\hat{z} + (1/2 + \sqrt{3}i/2)(\sin\phi_0 + 1)\hat{y}\big\}, \tag{6.41}$$

and zero for all other modes inside the first Brillouin zone except the complex conjugate mode $\mathbf{S}_{q=-(\pi/3)\hat{y}}$. For the uniform rotation with $\phi_0 = \pi/3$, $\mathbf{S}_{q=\pi\hat{y}} = 0$, so it is twisting the spins toward the $\hat{y}$-direction that leads to occupation of the secondary mode.

Spiral phases in Fourier space

When calculating the energy of the incommensurate spiral-1 and spiral-2 phases, we use the Hamiltonian (6.23) in the single mode approximation, where we assume the state to consist of only one Fourier mode. To prepare for the calculations, we now derive some requirements on the variational parameters $\mathbf{S}_q$.

The components of each Fourier mode $\mathbf{S}_q$, satisfy Parsevals theorem individually,

$$\sum_q |S_q^a|^2 = \sum_i (S_i^a)^2, \tag{6.42}$$

and summing over all components, we get

$$\sum_q |\mathbf{S}_q|^2 = NS^2, \tag{6.43}$$

In the single-mode approximation, the only non-zero components are $\mathbf{S}_{q_0}$ and $\mathbf{S}_{-q_0}$ for some quasimomentum $\mathbf{q}_0$. Using $\mathbf{S}_q = \mathbf{S}^*_{-q}$, the above equation gives

$$|\mathbf{S}_{q_0}|^2 = \frac{1}{2} N S^2. \tag{6.44}$$

We should also satisfy the stronger requirement $\mathbf{S}_i \cdot \mathbf{S}_i = S^2$. Inserting the Fourier transform and using the global Parseval theorem gives

$$\mathrm{Re}\left\{\mathbf{S}_{q_0} \cdot \mathbf{S}_{q_0} e^{-2i\mathbf{q}_0 \cdot \mathbf{r}_i}\right\} = 0. \tag{6.45}$$

Since this holds for all $\mathbf{r}_i$, it is a rather strong restriction on $\mathbf{S}_{q_0}$. Assuming $\mathbf{q}_0$ is an incommensurate wavevector, the exponential is a phase factor which takes infinitely many values with different $\mathbf{r}_i$. Since $\mathbf{S}_{q_0} \cdot \mathbf{S}_{q_0}$ is constant, the only way to satisfy (6.45) is $\mathbf{S}_{q_0} \cdot \mathbf{S}_{q_0} = 0$. Expressing the Fourier mode as

$$\mathbf{S}_{q_0} = \sqrt{NS^2/2} \, (\gamma_x e^{i\phi_x}, \ \gamma_y e^{i\phi_y}, \ \gamma_z e^{i\phi_z}), \tag{6.46}$$

Parsevals theorem becomes

$$\gamma_x^2 + \gamma_y^2 + \gamma_z^2 = 1, \tag{6.47}$$

and the constant spin length condition

$$\gamma_x^2 \cos 2\phi_x + \gamma_y^2 \cos 2\phi_y + \gamma_z^2 \cos 2\phi_z = 0 \tag{6.48}$$

$$\gamma_x^2 \sin 2\phi_x + \gamma_y^2 \sin 2\phi_y + \gamma_z^2 \sin 2\phi_z = 0. \tag{6.49}$$

For commensurate phases, the requirement is less dramatic. Considering for instance the 4x1 spiral-2 phase in the previous subsection, we have $q_0 = (\pi/2)\hat{y}$, and hence the exponential factor in (6.45) reduces to $e^{-i\pi y} = (-1)^y$. Since this is real, we do not need to rely on complete cancellation of the individual component terms in $\mathbf{S}_{q_0} \cdot \mathbf{S}_{q_0}$, since we can choose all terms $(S_q^a)^2$ to be purely imaginary. This allows us to vary the relative weight of the y- and z-directions in the Fourier transform (6.36) of the 4x1 S2 phase even with only one mode.

Incommensurate spiral-2 phase

For the incommensurate spiral-2 phase, using the representation in (6.46), we need $\gamma_x = 0$, and using the global phase freedom, we can choose $\phi_z = 0$. To satisfy (6.49), we then need $\cos 2\phi_y = -1$, and hence $\gamma_y = \gamma_z$. As illustrated by the commensurate 4x1 and 6x1 spiral-2 phases, it is often energetically favourable to twist spins toward the y-direction. This is therefore a serious constraint on the variational state, and the only variational parameter we have left is the momentum vector $\mathbf{q}_0 = (0, q_0)$.

Inserting in the Hamiltonian (6.23)

$$S_{q_0}^x = 0 \qquad S_{q_0}^y = \sqrt{\frac{NS^2}{2}} \frac{1}{\sqrt{2}} \qquad S_{q_0}^z = \sqrt{\frac{NS^2}{2}} \frac{1}{\sqrt{2}} e^{-i\pi/2} \tag{6.50}$$

and using

$$i\mathbf{S}_{q_0} \times \mathbf{S}_{-q_0} = \frac{NS^2}{2}(-\hat{x}), \tag{6.51}$$
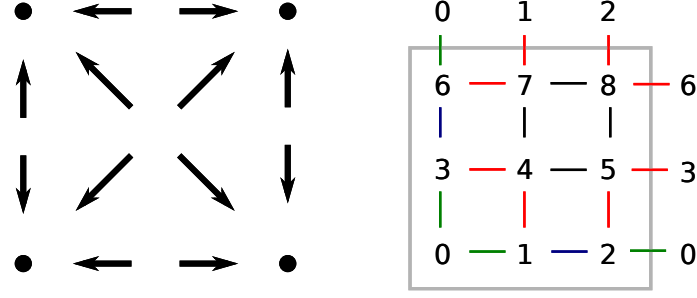
we end up with

Figure 6.4: The left panel shows the components of the 3x3 skyrmion crystal phase in the xy-plane. The right panel shows the labelling of the variational state. The spins are divided into groups, where spins 1, 2, 3, and 6 form a group, and 4, 5, 7, and 8 another, while spin 0 is a group on its own. This motivates the color-coding of links between neighbouring spins.

$$E = -NS^2 \left(\frac{4t_0^2}{\lambda u} \right) \left\{ \lambda \cos 2\alpha \cos q_0 + \lambda \sin 2\alpha \sin q_0 + \frac{1}{2} \left[1 + (2\lambda - 1) \cos 2\alpha \right] \right\}. \tag{6.52}$$

Minimizing with respect to q_0 gives the simple $q_0 = 2\alpha$, and energy

$$E_{\text{ICS2}} = - \left(\frac{4t_0^2}{\lambda u} \right) \left\{ \frac{1}{2} \left[1 + (2\lambda - 1) \cos 2\alpha \right] + \lambda \right\}. \tag{6.53}$$

Incommensurate spiral-1 phase

A similar calculation can be done for the incommensurate spiral-1 phase. We choose

$$S_{q_0}^x = S_{q_0}^y = \sqrt{\frac{NS^2}{2}} \frac{1}{2} \qquad S_{q_0}^z = \sqrt{\frac{NS^2}{2}} \frac{1}{\sqrt{2}} e^{-i\pi/2}, \tag{6.54}$$

and have momentum vector $\mathbf{q}_0 = (q_0, q_0)$. Inserting again in the Hamiltonian (6.23), the energy becomes

$$E_{\text{ICS1}} = -NS^2 \left(\frac{4t_0^2}{\lambda u} \right) \left\{ \left[\frac{1}{2} + (2\lambda - 1/2) \cos 2\alpha \right] \cos q_0 + \sqrt{2} \lambda \sin 2\alpha \sin q_0 \right\} \tag{6.55}$$

as function of the variational parameter. As earlier, the minimum of such an expression is given by the square root of the coefficients in front of the sine and cosine,

$$E_{\text{ICS1}} = -NS^2 \left(\frac{4t_0^2}{\lambda u} \right) \left\{ \left[\frac{1}{2} + (2\lambda - 1/2) \cos 2\alpha \right]^2 + 2\lambda^2 \sin^2 2\alpha \right\}^{1/2}. \tag{6.56}$$

The wavevector minimizing the energy is determined by

$$\tan q_0 = \frac{\sqrt{2} \lambda \sin 2\alpha}{1/2 + (2\lambda - 1/2) \cos 2\alpha}, \tag{6.57}$$

where $0 \leq q_0 \leq \pi$.

6.3.4 Skyrmion phase

Consider the skyrmion configuration in figure 6.4, which is based on the illustration of the skyrmion phase in [104]. We number the spins as in the right panel, and divide them into three groups. The spin $\mathbf{S}_0$ is on its own, and aligned in the z-direction. The spins 1, 2, 3, and 6 belong to the same group, and form angle θ with the z-axis. The spins 4, 5, 7, 8 constitute the last group, and form angle ϕ with the z-axis. The components in the xy-plane are as shown in the figure. We now write down all spins:

$$
\begin{aligned}
\mathbf{S}_0 &= S\hat{z} \\
\mathbf{S}_1 &= S(\cos\theta\ \hat{z} - \sin\theta\ \hat{x}) & \mathbf{S}_2 &= S(\cos\theta\ \hat{z} + \sin\theta\ \hat{x}) \\
\mathbf{S}_3 &= S(\cos\theta\ \hat{z} - \sin\theta\ \hat{y}) & \mathbf{S}_6 &= S(\cos\theta\ \hat{z} + \sin\theta\ \hat{y}) \\
\mathbf{S}_4 &= S(\cos\phi\ \hat{z} + \sin\phi\ (-\hat{x} - \hat{y})/\sqrt{2}) & \mathbf{S}_5 &= S(\cos\phi\ \hat{z} + \sin\phi\ (+\hat{x} - \hat{y})/\sqrt{2}) \\
\mathbf{S}_7 &= S(\cos\phi\ \hat{z} + \sin\phi\ (-\hat{x} + \hat{y})/\sqrt{2}) & \mathbf{S}_8 &= S(\cos\phi\ \hat{z} + \sin\phi\ (+\hat{x} + \hat{y})/\sqrt{2})
\end{aligned}
\tag{6.58}
$$

Links between spins can be characterized by which group the spins they connect belong to, and this is shown with color-coding in figure 6.4, where there are green, blue, red, and black links. Consider first the Heisenberg term. The Heisenberg energy of the skyrmion state is

$$
\begin{aligned}
9E^H/NS^2 =\ & 4\cos\theta\ J^z \\
& + 2\cos^2\theta\ J^z - \sin^2\theta\ (J_x^x + J_y^y) \\
& + 8\cos\theta\cos\phi\ J^z + 2\sqrt{2}\sin\theta\sin\phi\ (J_x^y + J_y^x) \\
& + 4\cos^2\phi\ J^z + \sin^2\phi\ (J_x^y + J_y^x - J_y^y - J_x^x),
\end{aligned}
\tag{6.59}
$$

where the different lines correspond to green, blue, red, and black links respectively.

For the Dzyaloshinskii-Moriya term, black links do not contribute since there is cancellation between links 4-5 and 7-8, and similarly for 4-7 and 5-8. For green, blue, and red links, we then get

$$
\begin{aligned}
9E^{\mathrm{DM}}/NS^2 =\ & 2\sin\theta\ (\hat{x}\cdot\mathbf{D}_y - \hat{y}\cdot\mathbf{D}_x) \\
& + 2\sin\theta\cos\theta\ (\hat{y}\cdot\mathbf{D}_y - \hat{x}\cdot\mathbf{D}_y) \\
& + 2\sqrt{2}\sin\phi\cos\theta + \sqrt{2}\sin\phi\cos\theta\ (\hat{x}\cdot\mathbf{D}_y - \hat{y}\cdot\mathbf{D}_x).
\end{aligned}
\tag{6.60}
$$

Collecting the terms and expressing the spin model coupling constants in terms of the original boson model parameters, the energy becomes

$$
\begin{aligned}
E_{3\mathrm{x}3\mathrm{SkX}}(\theta,\phi) = -\frac{NS^2}{9}\left(\frac{4t_0^2}{\lambda u}\right)\Big\{ & (4\cos\theta + 4\cos^2\phi + 2\cos^2\theta + 8\cos\theta\cos\phi)(2\lambda - 1)\cos 2\alpha \\
& - 2(\sin^2\phi + \sin^2\theta)\cos 2\alpha + 2(2\sqrt{2}\sin\theta\sin\phi + \sin^2\phi) \\
& + 4(\sin\theta - \sin\theta\cos\theta + \sqrt{2}\sin\phi\cos\theta)\lambda\sin 2\alpha\Big\}.
\end{aligned}
$$

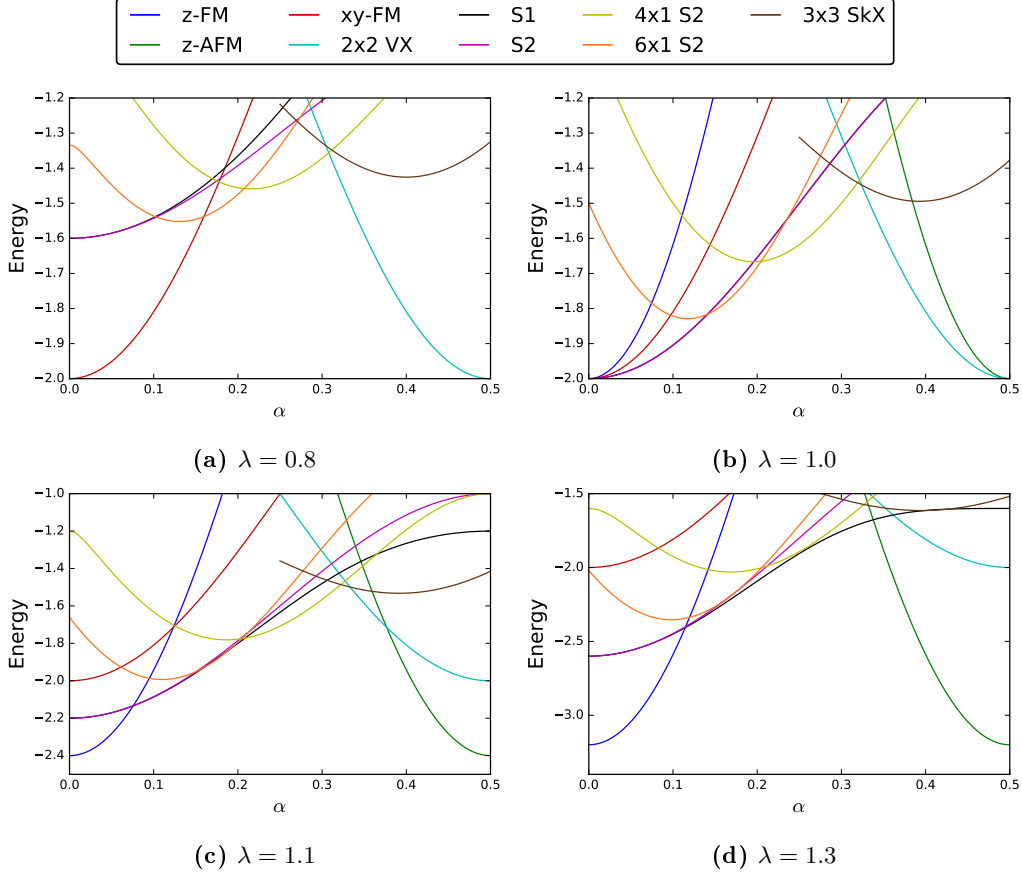This can be minimized with respect to the variational parameters θ and ϕ. We do this numerically.

Figure 6.5: Variational state energies per spin in units of $4St_0^2/\lambda u$ as function of α at different fixed λ.

6.3.5   Comparison of variational energies

In this section, we compare the variational energies and obtain a phase diagram similar to figure 6.1 obtained by Monte-Carlo simulations in [104]. We also discuss physical mechanisms behind the phase diagrams.

In figure 6.5, we have fixed λ and plot the classical ground state energies as function of α in units of $4t_0^2 S^2/\lambda u$. In 6.6, we keep α fixed and plot as function of λ. By picking out the state with the lowest energy at all points (α, λ) in parameter space, we get a phase diagram. Some of the transition lines can even be determined analytically. For instance, by equating the zAFM and vortex state energies, one obtains the transition line between the 2x2 VX and zAFM states,

$$\lambda = \frac{1}{4}\left(3 - \frac{1}{\cos 2\alpha}\right). \tag{6.61}$$

We present the variational phase diagram in figure 6.7.

Qualitatively, there is rather good agreement with the phase diagram in [104]. Although the transition lines are not at exactly the same place, the general shape is the very similar. This is to be expected, since the energy difference between various variational states can be small, as shown for instance in figure 6.5. Approximations in the variational approach and numerical errors and finite size effects in Monte-Carlo simulations may therefore distort the phase diagrams relative to each other.
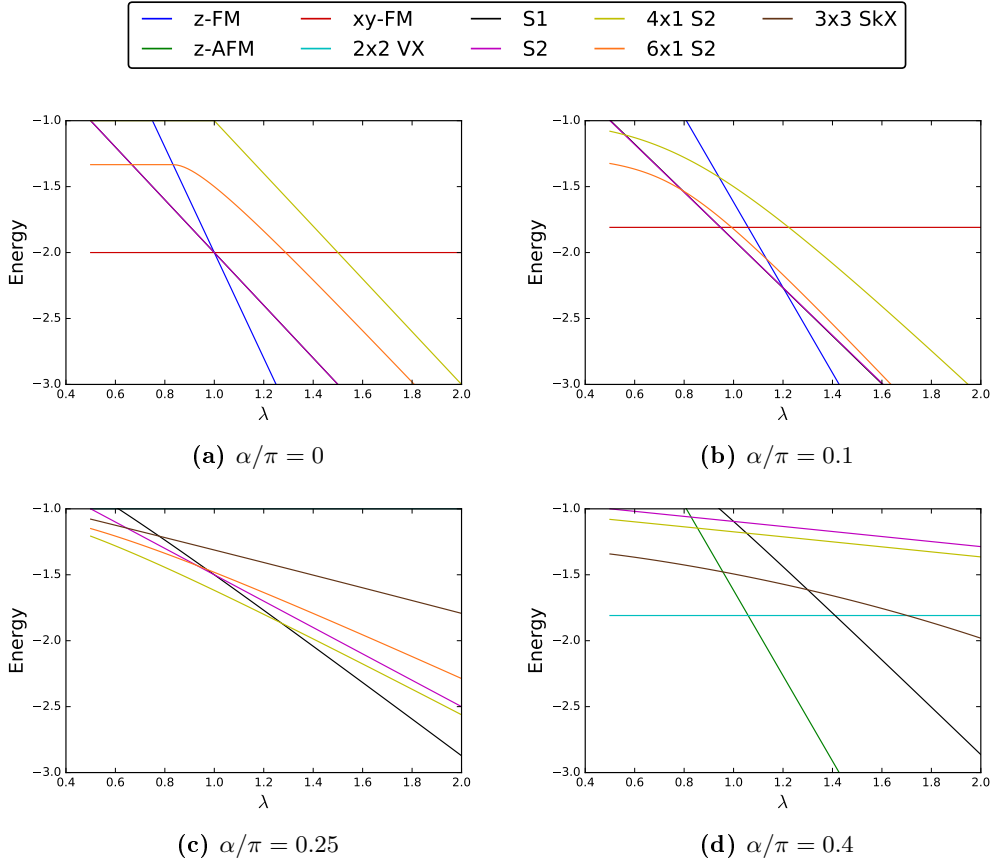
Figure 6.6: Variational state energies per spin in units of $4St_0^2/\lambda u$ as function of λ at different fixed α.
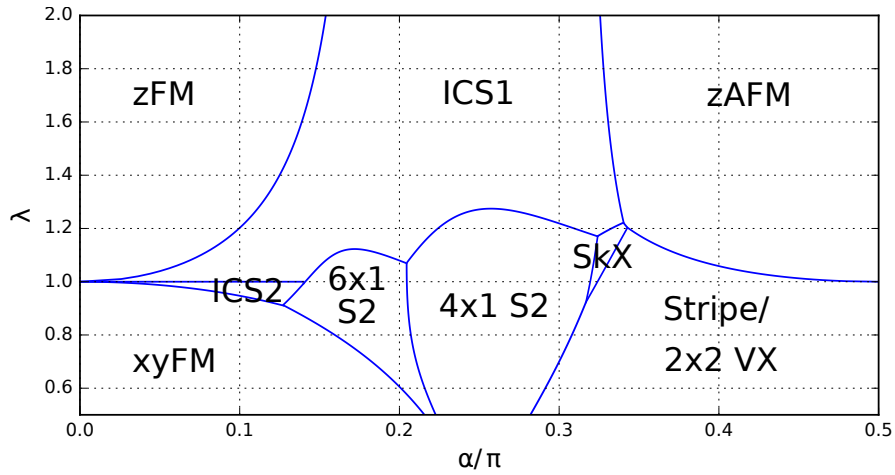

Figure 6.7: Classical variational spin texture phase diagram for the Mott insulator, where λ is the inter-relative to intracomponent interaction strength in the original boson model, and where α determines the relative importance of ordinary and SOC-induced hoppings. The phase diagram shows phases such as the z-ferromagnet (zFM), z-antiferromagnet (zAFM), ferromagnet in the xy-plane (xyFM), vortex (VX) and stripe, skyrmion (SkX), and various spiral (S) phases. For a detailed description, we refer to the main text.

The phase diagram can be understood through competition between terms in the effective spin model. Considering first small α, the coefficients in the Heisenberg term of the spin model (6.18) are ferromagnetic. Since the Dzyaloshinskii-Moriya term is small, the system typically favours ferromagnetic alignment. If $\lambda > 1$, the coupling constant J^z dominates the other Heisenberg couplings since $2\lambda - 1 > 1$, and we therefore get a z-ferromagnet. For $\lambda < 1$, the situation is reversed, and we get alignment in the xy-plane. The exception is if λ is close to 1. In the emergent slowly spiralling phases, the Heisenberg term still dominates the DM interaction, but the Heisenberg anisotropy does not.

Close to $\alpha = \pi/2$, the Heisenberg coupling J^z is antiferromagnetic and gives the zAFM phase for $\lambda \gtrsim 1$. For $\lambda < 1$, the situation is somewhat different because the couplings in the xy-plane are both ferro- and antiferromagnetic. This gives rise to the somewhat more exotic 2x2 vortex phase.

In the middle of the phase diagram, the DM term dominates and generates spiral phases. The spirals can be divided into two groups. The spiral-1 and spiral-2 phases are spiralling in different planes, and the spiral-1 phase always occurs for larger λ than spiral-2. This is because the overall strength of the Heisenberg coupling relative to the DM strength is reduced with increasing λ. Since unlike the S1 phase, the S2 phase has neighbouring spins with perfect ferromagnetic alignment, an increase in λ profits the S1 phase. In our phase diagram 6.7, the line between the incommensurate S1 and S2 phases goes at $\lambda = 1$, which can be shown by inserting $\lambda = 1$ in the two variational energies. This is a difference from the Monte-Carlo phase diagram 6.1, where this line is bent upwards. We believe the reason for this mismatch is that the incommensurate spiral phases cannot twist their spins toward the y-direction in the single-mode approximation. The effect of this is more significant for the S2-phase because of the perfect ferromagnetic alignment in one of the spatial directions.

Another difference between the phase diagrams is that the variational diagram has a smaller zFM region. Since the zFM variational energy is exact and the spiral-1 phase energy can only get better by increasing the number of variational parameters, this cannot be due to weaknesses in the variational approach. We believe instead that it traces back to finite size effects in the Monte-Carlo simulations, where Ref. [104] uses a lattice with size of order 30x30. Domain walls then make the spiral and skyrmion phases somewhat less competitive. The size of the skyrmion region is also different. This should be because our variational Ansatz for the skyrmion state is too simple, but qualitatively, we have shown the existence of a region with a competitive commensurate 3x3 skyrmion crystal occurring in approximately the right place.

We mentioned in section 4.3.2 that spin textures are typically similar at different sides of the SF-MI transition. Comparing with our weak coupling mean field result, there are similarities between the derived zero-temperature parabolic transition line in equation (5.46) and the shape of the zFM-S1 transition in the Mott insulator phase. Although the spin texture problem close to the SF-MI transition cannot be studied with the methods we have applied in this chapter, this is still an example of a resemblance in the weakly and strongly coupled regimes.

In conclusion, the location of transition lines is sensitive on method and approximations because the difference between energies of the various states can be small. This causes differences between the phase diagram obtained here and by classical Monte-Carlo simulations in Ref. [104]. In spite of this, we have reproduced the main qualitative features of the phase diagram with a variational approach. We have also discussed the physical mechanisms behind, starting from the effective spin model.

6.4   Excitation spectra

The treatment in the previous sections was entirely classical. In this section, we consider quantum excitations on top of some of the classical ground states.

Various approaches have been applied to study quantum excitations on top of spin models with Dzyaloshinskii-Moriya interaction. In the Schwinger boson mean field theory, one may use

homogeneous decoupling of link variables for ferromagnetic and antiferromagnetic phases to obtain the excitation spectrum and quantum corrections [136–138]. Jordan-Wigner fermionization is particularly well suited for one-dimensional systems [105, 118, 135], but has also been generalized to two dimensions [139]. Dynamical mean-field theory [120] and Ginzburg-Landau theory [140, 141] have also been applied successfully. We will use the Holstein-Primakoff transformation to calculate excitation spectra of the spin model [142–146].[2] Introduced already in 1940, it has ever since been a useful tool for analysing spin wave collective excitation in magnetic systems [64, 149].

We consider the zFM, zAFM, xyFM, and stripe phases. The general procedure is first to introduce Holstein-Primakoff bosons, then decouple lattice sites through Fourier transform, before diagonalizing the problem with a Bogoliubov transform. We discuss qualitative features of the excitation spectra around the minima and quantum fluctuations in the ground state on basis of the energy eigenvalues.

6.4.1 zFM excitation spectrum

For the zFM phase, introduce Holstein-Primakoff boson operators a_i such that [64]

$$S_i^z = S - a_i^\dagger a_i \tag{6.62}$$

$$S_i^+ = (2S - a_i^\dagger a_i)^{1/2} a_i \tag{6.63}$$

$$S_i^- = a_i^\dagger (2S - a_i^\dagger a_i)^{1/2}. \tag{6.64}$$

Assuming a_i and $a_i^\dagger$ satisfy boson commutation relations, one may show that the above spin operators satisfy the angular momentum algebra $[S^\alpha, S^\beta] = i\epsilon^{\alpha\beta\gamma}S^\gamma$. Boson excitations correspond to deviations from perfect ferromagnetic ordering. The idea is to make an expansion in the parameter $1/S$, and to include in the analysis only terms up to quadratic order in bosons, thus neglecting their interaction. This corresponds to the classical limit. Although we only have $S = 1/2$, praxis has shown that this expansion gives quite sensible results [150]. We get

$$S_i^z = S - a_i^\dagger a_i \qquad S_i^+ \simeq \sqrt{2S}\, a_i \qquad S_i^- \simeq \sqrt{2S}\, a_i^\dagger. \tag{6.65}$$

For the Dzyaloshinskii-Moriya interaction, we have

$$H_{\text{DM}} = \mathcal{D} \sum_i \left\{ (S_i^x S_{i+\hat{x}}^z - S_i^z S_{i+\hat{x}}^x) + (S_i^y S_{i+\hat{y}}^z - S_i^z S_{i+\hat{y}}^y) \right\}. \tag{6.66}$$

Since S_i^x and S_i^y are linear in boson operators to lowest order, we let $S_i^z \simeq S$. Inserting this in the above expression, making a shift $i + \delta \to i$ in some of the terms, the whole term becomes zero to quadratic boson order. The Hamiltonian can then be written as

$$
\begin{aligned}
H &= \sum_{i,\delta} \left\{ J^z S_i^z S_{i+\delta}^z + \frac{1}{4} J_\delta^x (S_i^+ + S_i^-)(S_{i+\delta}^+ + S_{i+\delta}^-) - \frac{1}{4} J_\delta^y (S_i^+ - S_i^-)(S_{i+\delta}^+ - S_{i+\delta}^-) \right\} \\
&= \sum_{i,\delta} \left\{ J^z S_i^z S_{i+\delta}^z + \frac{1}{4}(J_\delta^x + J_\delta^y)(S_i^+ S_{i+\delta}^- + S_i^- S_{i+\delta}^+) + \frac{1}{4}(J_\delta^x - J_\delta^y)(S_i^+ S_{i+\delta}^+ + S_i^- S_{i+\delta}^-) \right\}
\end{aligned}
\tag{6.67}
$$

---

[2] During the preparation of this manuscript, we became aware of two related very recent articles. In [147], Holstein-Primakoff transformation is applied to the model with spin-independent interaction ($\lambda = 1$) and general linear combination of Rashba and Dresselhaus SOC. In [148], the model with Rashba SOC and spin-independent interaction is investigated using quantum simulations. We discuss both articles in more detail in the final section of this chapter.

Inserting Holstein-Primakoff boson operators, we get real space Hamiltonian

$$H = E_0 - 4SJ^z \sum_i a_i^\dagger a_i + \frac{S}{2} \sum_{i,\delta} \left\{ (J_\delta^x - J_\delta^y)(a_i^\dagger a_{i+\delta}^\dagger + a_i a_{i+\delta}) + (J_\delta^x + J_\delta^y)(a_i^\dagger a_{i+\delta} + a_i a_{i+\delta}^\dagger) \right\},$$
(6.68)

where $E_0 = 2NS^2J^z$ is the classical ground state energy. Lattice sites are decoupled by introducing Fourier transformed bosons and using the usual delta function identity (5.12). We performed exactly the same type of calculation when finding the dispersion relation for the weakly coupled fluid in section 5.1. The result is

$$H = E_0 + \frac{1}{2} \sum_q \{ A_q(a_q^\dagger a_q + a_{-q}^\dagger a_{-q}) + B_q(a_q a_{-q} + a_q^\dagger a_{-q}^\dagger) \},$$
(6.69)

with

$$A_q = S \left(\frac{4t_0^2}{\lambda u} \right) [4(2\lambda - 1)\cos 2\alpha - (1 + \cos 2\alpha)(\cos q_x + \cos q_y)]$$
(6.70)

$$B_q = S \left(\frac{4t_0^2}{\lambda u} \right) (1 - \cos 2\alpha)(\cos q_x - \cos q_y).$$
(6.71)

The standard Bogoliubov transformation in section 2.4 gives energy spectrum

$$\omega_q = \sqrt{A_q^2 - B_q^2}.$$
(6.72)

Further insight is provided by Taylor-expanding ω_q around the minimum at $\mathbf{q} = 0$. To order $\mathcal{O}(q^2)$, we obtain

$$\omega_q = S \left(\frac{4t_0^2}{\lambda u} \right) \sqrt{a_0 + a_2 q^2 + \mathcal{O}(q^4)},$$
(6.73)

where

$$a_0 = [8(\lambda - 1)\cos 2\alpha - 2(1 - \cos 2\alpha)]^2$$
(6.74)

$$a_2 = (1 + \cos 2\alpha) [8(\lambda - 1)\cos 2\alpha - 2(1 - \cos 2\alpha)].$$
(6.75)

Hence, the dispersion relation has a gap $\sqrt{a_0}$ which protects the zFM state against thermal fluctuations, and quadratic dependence around the minimum. For $\alpha = 0$ and $\lambda = 1$, the spin model reduces to the isotropic Heisenberg model with quadratic dispersion [64]. This is consistent with our result, because a_0 and a_2 vanish and leave quartic dependence within the square root.

The coefficient a_2 becomes negative immediately after the gap a_0 closes, and therefore, the eigenvalue becomes imaginary. This corresponds to an instability, and we plot the line where it happens in figure 6.9. Since this is well outside the classical zFM region, our result remains valid, and we do not expect quantum fluctuations to substantially reduce the extent of the classical region. Since we have neglected the DM interaction entirely, we could not hope to reproduce the zFM-S1 transition.

We plot the dispersion relation along $q_y = 0$ for fixed λ and several α in figure 6.8b. The gap becomes smaller with increasing α because of the weaker Heisenberg coupling strength, but in addition, the effect is enhanced by the reduction of J^z relative to $J_x^y = J_y^x$.

For the XXZ-model given by $\alpha = 0$, the classical and quantum mechanical ground states are equal because $B_q = 0$ and no Bogoliubov transformation is necessary. At finite α, the classical
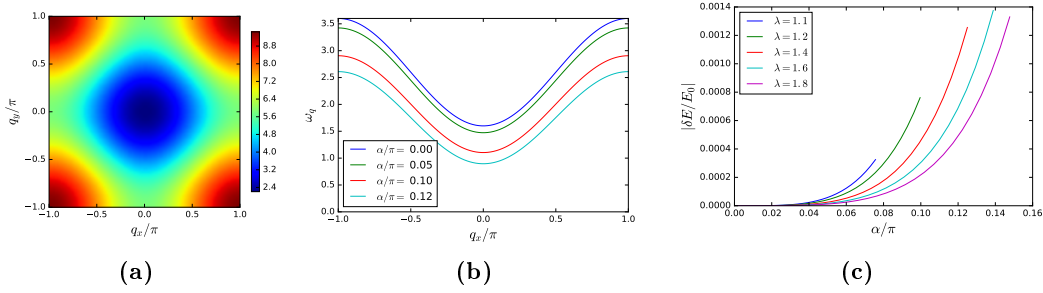
Figure 6.8: Figure (a) shows the Brillouin zone structure of dispersion relation for the z-ferromagnet at $\lambda = 1.2$ and $\alpha/\pi = 0.1$. Figure (b) shows the dispersion relation along $q_y = 0$ for $\lambda = 1.2$. The state is protected by a gap. Figure (c) shows quantum corrections for different λ up to the point where the variational calculation predicts transition to the spiral phase.

ground state energy E_0 gets an additional quantum correction $E_q - E_0$, as apparent from the diagonalized Hamiltonian

$$H = E_0 + \frac{1}{2}\sum_q (\omega_q - A_q) + \sum_q \omega_q \alpha_q^\dagger \alpha_q. \tag{6.76}$$

Since $A_q > \omega_q$, the correction is negative. Although quantum fluctuations reduce the magnetization in the preferred spin space z-direction, the possibility of quantum superposition can be utilized to reduce the ground state energy by obtaining contributions from coupling between x- and y-components. We plot the quantum corrections as function of α at different fixed λ in figure 6.8c. The corrections increase with α, but are always small.

We may now calculate the magnetization of the system using

$$M = \sum_i \langle S_i^z \rangle = NS - \sum_i \langle a_i^\dagger a_i \rangle. \tag{6.77}$$

By re-expressing the original bosons in terms of the rotated Bogoliubov bosons discussed in section 2.4, one may show

$$M = NS - \frac{1}{2}\sum_q \left(\frac{A_q}{\omega_q} - 1\right) - \sum_q \frac{A_q/\omega_q}{e^{\beta\omega_q} - 1}. \tag{6.78}$$

The corrections in the magnetization are of the same order as in the energy, as one can see by expanding them in the small parameter B_q/A_q.

For the zFM phase, we have now shown that quantum fluctuation effects are small by introducing the Holstein-Primakoff transformation. The Dzyaloshinskii-Moriya interaction does not contribute to the excitation spectrum to lowest order in the spin wave expansion, and the state is protected against thermal fluctuations by a gap.

6.4.2 zAFM excitation spectrum

We now discuss the zAFM excitation spectrum. The base case of an isotropic antiferromagnetic Heisenberg model requires a Bogoliubov transformation, and gives a linear dispersion relation [64, 128, 151]. Unlike the zFM phase, there is no choice of parameters α and λ which leads to the base case, but we still adopt the same procedure.

To reproduce the ground state in the absence of boson excitations, we need different boson operators on the sublattices with opposite magnetic ordering. To lowest order in the $1/S$-expansion, we introduce Holstein-Primakoff bosons
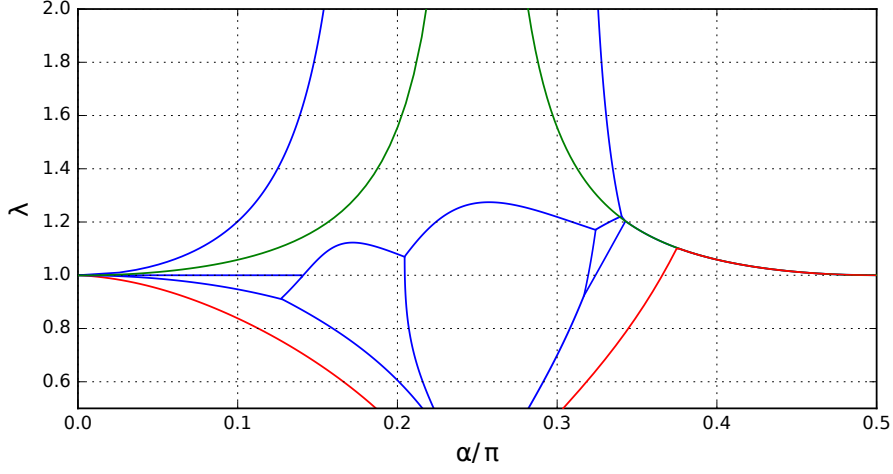
Figure 6.9: Quantum fluctuation effects on the classical Mott insulator variational phase diagram in section 6.3. The green lines show where the Holstein-Primakoff approach breaks down for the zFM- and zAFM phases. This happens outside the classical regions. The red line in the classical xyFM region indicates the appearance of a continuously degenerate minimum and possible breakdown of magnetic ordering. The red line in the classical stripe or vortex phase region indicates breakdown of the stripe phase and leads to a significant reduction of the stripe phase region to lowest order in the spin wave expansion.

$$S_\alpha^z = S - a_\alpha^\dagger a_\alpha \qquad S_\alpha^+ \simeq \sqrt{2S}\, a_\alpha \qquad S_\alpha^- \simeq \sqrt{2S}\, a_\alpha^\dagger \tag{6.79}$$

$$S_\beta^z = -S + b_\beta^\dagger b_\beta \qquad S_\beta^+ \simeq \sqrt{2S}\, b_\beta^\dagger \qquad S_\beta^- \simeq \sqrt{2S}\, b_\beta \tag{6.80}$$

for lattice sites $\alpha \in A$ on the sublattice with magnetic ordering along $+\hat{z}$, and $\beta \in B$ on the sublattice with ordering along $-\hat{z}$.

The Dzyaloshinskii-Moriya interaction is still

$$\begin{aligned}
H_{\mathrm{DM}} &= \frac{4t_0^2}{u} \sin 2\alpha \sum_i \left\{ S_i^x S_{i+x}^z - S_i^z S_{i+x}^z + S_i^y S_{i+y}^z - S_i^z S_{i+y}^y \right\} \\
&= \frac{4t_0^2}{u} \sin 2\alpha \sum_i \left\{ S_i^x S_{i+x}^z - S_{i-x}^z S_i^x + S_i^y S_{i+y}^z - S_{i-y}^z S_i^y \right\},
\end{aligned} \tag{6.81}$$

and to quadratic order in bosons, we keep only, $S_i^z \simeq \pm S$. Since the lattice sites $\mathbf{r}_{i\pm\delta}$ have the same magnetic ordering, we get

$$H_{\mathrm{DM}} \simeq 0 \tag{6.82}$$

also for the z-antiferromagnet. This leaves the Heisenberg term, and inserting the boson operators gives

$$H = -2NS^2J^z + \sum_{\alpha,\delta} 2SJ^z a_\alpha^\dagger a_\alpha + \sum_{\beta,\delta} 2SJ^z b_\beta^\dagger b_\beta$$

$$+ \frac{S}{2} \sum_{\alpha,\delta} \left\{ (J_\delta^x + J_\delta^y)(a_\alpha^\dagger b_{\alpha+\delta}^\dagger + a_\alpha b_{\alpha+\delta}) + (J_\delta^x - J_\delta^y)(a_\alpha^\dagger b_{\alpha+\delta} + a_\alpha b_{\alpha+\delta}^\dagger) \right\} \quad (6.83)$$

$$+ \frac{S}{2} \sum_{\beta,\delta} \left\{ (J_\delta^x + J_\delta^y)(b_\beta^\dagger a_{\beta+\delta}^\dagger + b_\beta a_{\beta+\delta}) + (J_\delta^x - J_\delta^y)(b_\beta^\dagger a_{\beta+\delta} + b_\beta a_{\beta+\delta}^\dagger) \right\}.$$

Introduce Fourier transformed boson operators a_q and b_q in accordance with

$$a_i = \sqrt{\frac{2}{N}} \sum_q e^{-i\mathbf{q}\cdot\mathbf{r}_i} a_q \qquad b_i = \sqrt{\frac{2}{N}} \sum_q e^{-i\mathbf{q}\cdot\mathbf{r}_i} b_q, \qquad (6.84)$$

where the sum goes over the reduced Brillouin zone $|q_y| \leq |\pi - q_x|$ for $q_x \geq 0$ and $|q_y| \leq |\pi + q_x|$ for $q_x \leq 0$. Inserting in the Hamiltonian gives

$$H = E_0 + \frac{1}{2} \sum_q \Bigg\{ \; A_q \, (a_q^\dagger a_q + a_{-q}^\dagger a_{-q} + b_q^\dagger b_q + b_{-q}^\dagger b_{-q})$$

$$+ B_q \, (a_q^\dagger b_{-q}^\dagger + a_q b_{-q} + a_{-q}^\dagger b_q^\dagger + a_{-q} b_q) \qquad (6.85)$$

$$+ C_q \, (a_q^\dagger b_q + a_q b_q^\dagger + a_{-q}^\dagger b_{-q} + a_{-q} b_{-q}^\dagger) \Bigg\}$$

with

$$A_q = 4SJ^z \qquad\qquad = -4S \left(\frac{4t_0^2}{\lambda u} \right)(2\lambda - 1)\cos 2\alpha \qquad (6.86)$$

$$B_q = S\sum_\delta (J_\delta^x + J_\delta^y)\cos q_\delta \qquad = -S \left(\frac{4t_0^2}{\lambda u} \right)(1 + \cos 2\alpha)(\cos q_x + \cos q_y) \qquad (6.87)$$

$$C_q = S\sum_\delta (J_\delta^x - J_\delta^y)\cos q_\delta \qquad = S \left(\frac{4t_0^2}{\lambda u} \right)(1 - \cos 2\alpha)(\cos q_x - \cos q_y). \qquad (6.88)$$

We now perform the Bogoliubov transformation using the dynamic matrix method described in section 2.4. We write the Hamiltonian as

$$H = E_0 + \frac{1}{2} \sum_q \left\{ \frac{1}{2} \psi_q^\dagger M_q \psi_q - 2A_q \right\}, \qquad (6.89)$$

where

$$\psi_q^\dagger = \begin{pmatrix} a_q^\dagger & a_{-q}^\dagger & b_q^\dagger & b_{-q}^\dagger & a_q & a_{-q} & b_q & b_{-q} \end{pmatrix}, \qquad (6.90)$$

and M_q is the matrix

$$M_q = \begin{pmatrix} A_q & 0 & C_q & 0 & 0 & 0 & 0 & B_q \\ 0 & A_q & 0 & C_q & 0 & 0 & B_q & 0 \\ C_q & 0 & A_q & 0 & 0 & B_q & 0 & 0 \\ 0 & C_q & 0 & A_q & B_q & 0 & 0 & 0 \\ 0 & 0 & 0 & B_q & A_q & 0 & C_q & 0 \\ 0 & 0 & B_q & 0 & 0 & A_q & 0 & C_q \\ 0 & B_q & 0 & 0 & C_q & 0 & A_q & 0 \\ B_q & 0 & 0 & 0 & 0 & C_q & 0 & A_q \end{pmatrix}. \tag{6.91}$$

By simultaneously rearranging the rows and columns of this matrix, we can write M_q on the block diagonal form

$$M_q = \begin{pmatrix} \begin{matrix} A_q & C_q & 0 & B_q \\ C_q & A_q & B_q & 0 \\ 0 & B_q & A_q & C_q \\ B_q & 0 & C_q & A_q \end{matrix} & \\ & \begin{matrix} A_q & C_q & 0 & B_q \\ C_q & A_q & B_q & 0 \\ 0 & B_q & A_q & C_q \\ B_q & 0 & C_q & A_q \end{matrix} \end{pmatrix} = \begin{pmatrix} N_q & 0 \\ 0 & N_q \end{pmatrix}. \tag{6.92}$$

The rearrangements correspond to changing the order of the operators inside ψ_q, and here, this gives

$$\psi_q^\dagger \to \psi_q^\dagger = \begin{pmatrix} a_q^\dagger & b_q^\dagger & a_{-q} & b_{-q} & a_q & b_q & a_{-q}^\dagger & b_{-q}^\dagger \end{pmatrix} \tag{6.93}$$

We now have four coupled bosons instead of eight. Consdering the 4x4 matrix N_q and using the dynamic matrix method, we need to find the positive eigenvalues of

$$\tilde{N}_q = \begin{pmatrix} A_q & C_q & 0 & B_q \\ C_q & A_q & B_q & 0 \\ 0 & -B_q & -A_q & -C_q \\ -B_q & 0 & -C_q & -A_q \end{pmatrix}. \tag{6.94}$$

These are

$$\omega_q^\pm = \sqrt{(A_q \pm C_q)^2 - B_q^2}, \tag{6.95}$$

and the Hamiltonian becomes

$$H = E_0 + \frac{1}{2}\sum_q (\omega_q^+ + \omega_q^- - 2A_q) + \sum_q \left(\omega_q^+ \alpha_q^\dagger \alpha_q + \omega_q^- \beta_q^\dagger \beta_q \right) \tag{6.96}$$

with new boson operators α_q and β_q. The eigenvalues $\omega_q^\pm$ are related by $q_x \leftrightarrow q_y$, as apparent from the coefficient C_q.

As shown in figure 6.10, the dispersion relation is gapped. The minima are located at $\mathbf{q} = (\pm\pi, 0)$ and $\mathbf{q} = (0, \pm\pi)$, around which the dispersion relation is quadratic. One may again show this by Taylor expanding around the minima. In figure 6.9, we plot the line where the gap vanishes and the state develops an instability to lowest order in the spin wave expansion. The condition is exactly the same as for the zFM state if we let $\alpha \to \pi/2 - \alpha$, and the analysis therefore remains valid in the classical zAFM region. In figure 6.10c, we plot quantum corrections to the ground state energy. The corrections are small and negative, and the qualitative picture given for the z-ferromagnet applies here as well.
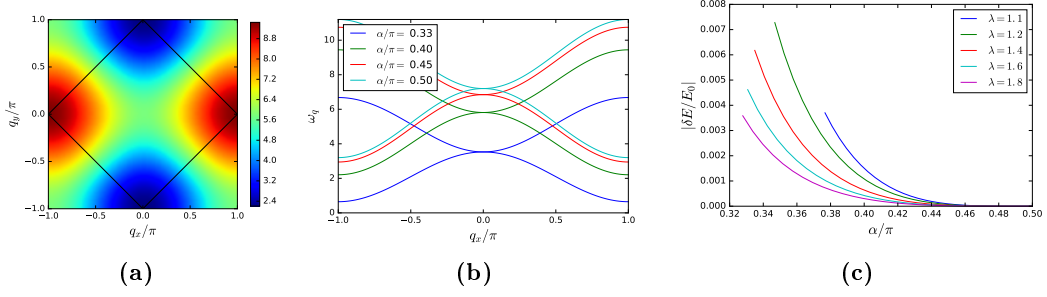
(a)   (b)   (c)

Figure 6.10: Figure (a) shows the Brillouin zone structure of the zAFM excitation spectrum eigenvalue ω_q^1 at $\lambda = 1.4$ and $\alpha/\pi = 0.4$, and the black lines indicate the reduced Brillouin zone. Figure (b) shows a cut along $q_y = 0$ at $\lambda = 1.4$ and different values of α. Finally, (c) shows the ground state energy quantum corrections up to the point where the variational calculation predicts transition to a different phase.

By introducing different bosons on the two sublattices with different magnetic ordering, we have now shown that quantum corrections are small. Hence, the ground state is well described by the classical antiferromagnetic state, and we do not expect the zAFM parameter space region to be significantly reduced by quantum fluctuations.

6.4.3 xyFM excitation spectrum

For the xy-ferromagnet, we assume spins are aligned at an angle ϕ with the x-axis, so that $\mathbf{S}_i = S(\cos\phi, \sin\phi, 0)$. We then rotate the spin space coordinate system so that the z-axis is aligned with the direction of ferromagnetic ordering. We first rotate the spin coordinate system down in the xy-plane through

$$S_i^x \rightarrow S_i^x \qquad S_i^y \rightarrow S_i^z \qquad S_i^z \rightarrow -S_i^y \tag{6.97}$$

and then do the rotation

$$\begin{pmatrix} S^x \\ S^z \end{pmatrix} \rightarrow \begin{pmatrix} \sin\phi & \cos\phi \\ -\cos\phi & \sin\phi \end{pmatrix} \begin{pmatrix} S^x \\ S^z \end{pmatrix}. \tag{6.98}$$

In the new spin space variables, the Hamiltonian becomes

$$H = \sum_{i,\delta} \left\{ (J_\delta^x \sin^2\phi + J_\delta^y \cos^2\phi) \, S_i^x S_{i+\delta}^x + J_\delta^z S_i^y S_{i+\delta}^y \right.$$
$$\left. + (J_\delta^x \cos^2\phi + J_\delta^y \sin^2\phi) \, S_i^z S_{i+\delta}^z + (J_\delta^x - J_\delta^y)\sin\phi\cos\phi \, (S_i^x S_{i+\delta}^z + S_i^z S_{i+\delta}^x) \right\} \tag{6.99}$$
$$+ \mathcal{D} \sum_i \left\{ \sin\phi(S_i^y S_{i+x}^x - S_i^x S_{i+x}^y) + \cos\phi \, (S_i^x S_{i+y}^y - S_i^y S_{i+y}^x) \right\}.$$

Introducing again the Holstein-Primakoff bosons of the ferromagnet from section 6.4.1, the term linear in boson operators from the DM interaction disappears because

$$\sum_\delta (J_\delta^x - J_\delta^y) = 0. \tag{6.100}$$

In real space, the Hamiltonian then becomes

$$H = NS^2 \sum_\delta (J_\delta^x \cos^2\phi + J_\delta^y \sin^2\phi) - 2S \sum_{i,\delta} (J_\delta^x \cos^2\phi + J_\delta^y \sin^2\phi) a_i^\dagger a_i$$

$$+ \sum_{i,\delta} \frac{S}{2} \left(J_\delta^x \sin^2\phi + J_\delta^y \cos^2\phi + J_\delta^z \right) (a_i a_{i+\delta}^\dagger + a_i^\dagger a_{i+\delta})$$

$$+ \sum_{i,\delta} \frac{S}{2} \left(J_\delta^x \sin^2\phi + J_\delta^y \cos^2\phi - J_\delta^z \right) (a_i a_{i+\delta} + a_i^\dagger a_{i+\delta}^\dagger)$$ (6.101)

$$+ iS\mathcal{D} \sum_i \left[\sin\phi \, (a_i^\dagger a_{i+x} - a_i a_{i+x}^\dagger) - \cos\phi \, (a_i^\dagger a_{i+y} - a_i a_{i+y}^\dagger) \right].$$

By Fourier transforming the various terms, we get

$$H = E_0 + \sum_q \left\{ (A_q + B_q) \, a_q^\dagger a_q + (A_q - B_q) \, a_{-q}^\dagger a_{-q} + C_q (a_q a_{-q} + a_q^\dagger a_{-q}^\dagger) \right\},$$ (6.102)

now with

$$A_q = -S \sum_\delta \left(J_\delta^x \cos^2\phi + J_\delta^y \sin^2\phi \right) + (S/2) \sum_\delta \left(J_\delta^x \sin^2\phi + J_\delta^y \cos^2\phi + J_\delta^z \right) \cos q_\delta$$ (6.103)

$$B_q = -\mathcal{D}S \left(\sin\phi \sin q_x - \cos\phi \sin q_y \right)$$ (6.104)

$$C_q = (S/2) \sum_\delta \left(J_\delta^x \sin^2\phi + J_\delta^y \cos^2\phi - J_\delta^z \right) \cos q_\delta.$$ (6.105)

The Bogoliubov transformation gives Hamiltonian

$$H = E_0 + \sum_q \left\{ \frac{1}{2}(\omega_q^+ + \omega_q^-) - A_q \right\} + \sum_q \left\{ \omega_q^+ \alpha_q^\dagger \alpha_q + \omega_q^- \beta_q^\dagger \beta_q \right\},$$ (6.106)

where α_q, β_q are two operators satisfying boson commutation relations, and where $\omega_q^\pm$ are the two positive eigenvalues of the matrix

$$\tilde{M}_q = \begin{pmatrix} A_q + B_q & 0 & 0 & C_q \\ 0 & A_q - B_q & C_q & 0 \\ 0 & -C_q & -(A_q + B_q) & 0 \\ -C_q & 0 & 0 & -(A_q - B_q) \end{pmatrix},$$ (6.107)

namely

$$\omega_q^\pm = \left| B_q \pm \sqrt{A_q^2 - C_q^2} \right|.$$ (6.108)

We can also express A_q, B_q, and C_q in terms of the parameters of the original boson model, obtaining
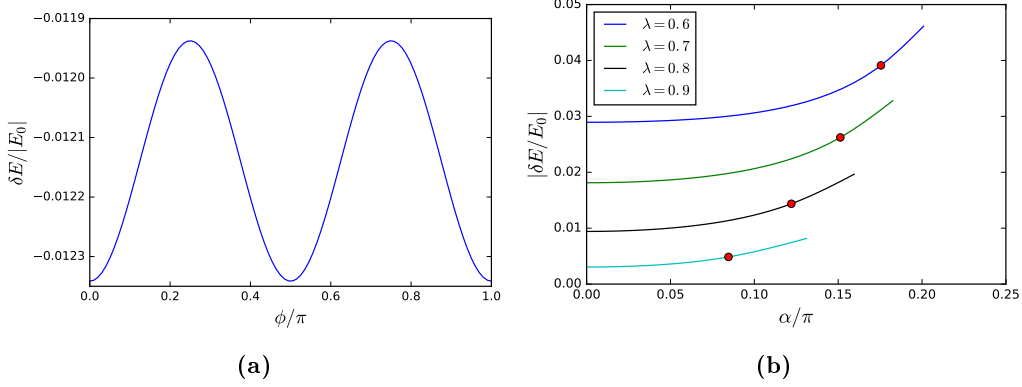
Figure 6.11: Quantum corrections δE for the xy-ferromagnet with classical energy E_0. Figure (a) shows the corrections as function of the ordering angle ϕ at $\alpha/\pi = 0.1$ and $\lambda = 0.8$. Due to the angle dependence, classical degeneracy is lifted in favour of alignment along the x- or y-axis. Figure (b) shows significant corrections increasing with α at different fixed λ inside the xyFM region predicted by the classical variational calculation. The red dots mark the appearance of the continuously degenerate minimum.

$$A_q = S\left(\frac{4t_0^2}{\lambda u}\right)\left\{1 + \cos 2\alpha - \frac{1}{2}\left[\cos 2\alpha \sin^2 \phi + \cos^2 \phi + (2\lambda - 1)\cos 2\alpha\right]\cos q_x\right.$$
$$\left. - \frac{1}{2}\left[\sin^2 \phi + \cos 2\alpha \cos^2 \phi + (2\lambda - 1)\cos 2\alpha\right]\cos q_y\right\} \tag{6.109}$$

$$B_q = S\left(\frac{4t_0^2}{\lambda u}\right)\lambda \sin 2\alpha\left[\sin \phi \sin q_x - \cos \phi \sin q_y\right] \tag{6.110}$$

$$C_q = -\frac{S}{2}\left(\frac{4t_0^2}{\lambda u}\right)\left\{\left[\cos 2\alpha \sin^2 \phi + \cos^2 \phi - (2\lambda - 1)\cos 2\alpha\right]\cos q_x\right.$$
$$\left. + \left[\sin^2 \phi + \cos 2\alpha \cos^2 \phi - (2\lambda - 1)\cos 2\alpha\right]\cos q_y\right\}. \tag{6.111}$$

Calculating the net magnetization, we need the eigenvectors of the dynamic matrix to construct the matrix T, which we again need to express $S^z = S - \sum_i a_i^\dagger a_i/N$ in terms of the new boson operators α and β. In these calculations, the Dzyaloshinskii-Moriya term drops out, so the calculation is in fact perfectly analogous to the regular two-species calculation with $B_q = 0$. The main qualitative features can however be extracted solely on basis of the eigenvalues.

First, the size of ground state energy quantum corrections indicates the importance of quantum fluctuations. Moreover, if the quantum correction to the ground state energy depends on the angle ϕ, the classical continuous degeneracy is lifted. As shown in figure 6.11a, there is in fact a very slight preference for alignment in the x- or y-direction. At $\alpha/\pi = 0.1$ and $\lambda = 0.8$, the quantum correction to the ground state energy is roughly 1 %, and the variations with alignment angle ϕ are up to 4 % of this. These are quite typical numbers, signifying that quantum corrections are important.

Second, the qualitative nature of thermal excitations is determined by the low energy behaviour of the excitation spectrum. In the following, we set $\phi = \pi/2$, which is one the states favoured by quantum fluctuations. The xy-ferromagnet dispersion relation is plotted in figure 6.12, and there is a minimum at $\mathbf{q} = 0$. Expanding around this gives

$$\omega_\pm = S\left(\frac{4t_0^2}{\lambda u}\right)\left|\lambda \sin(2\alpha)q_x \pm \sqrt{\gamma_0(\cos(2\alpha)q_x^2 + q_y^2)}\right| \tag{6.112}$$

(a)   (b)   (c)

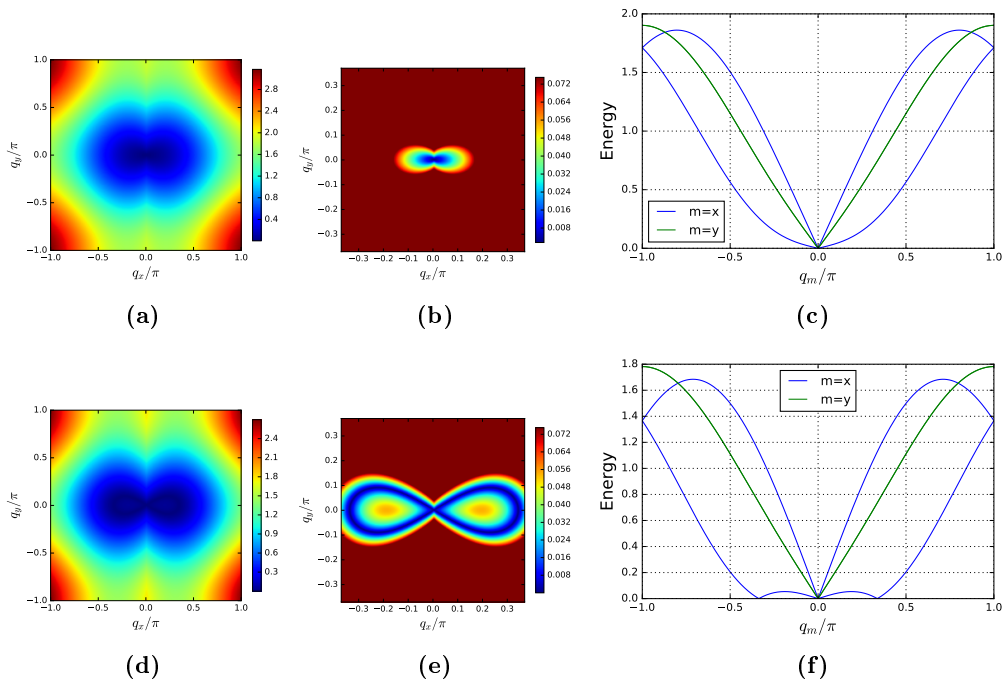(d)   (e)   (f)

Figure 6.12: Excitation spectrum for the xy-ferromagnet at $\lambda = 0.8$. Left figures: Dispersion relation in the first Brillouin zone. Middle figures: Brillouin zone structure of low energy excitations. Right figures: dispersion relation along x- and y-directions. First row: $\alpha/\pi = 0.1$. The dispersion relation is linear around the minimum. Second row: $\alpha/\pi = 0.15$. Sufficiently strong Dzyaloshinskii-Moriya interaction gives rise to a continuously degenerate minimum.

with

$$\gamma_0 = \frac{1}{2}(1 - \cos 2\alpha) + 2(1 - \lambda)\cos 2\alpha. \tag{6.113}$$

For sufficiently strong Dzyaloshinskii-Moriya interaction, the two terms can cancel, giving rise to a continuously degenerate minimum. This is illustrated in figure 6.12e. Since this minimum grows from $\mathbf{q} = 0$, the condition for this to happen can be determined from (6.112). If we let $\tan^2 \xi = q_y^2/q_x^2$, solving $\omega_q^- = 0$ at finite q gives

$$\frac{\lambda^2 \sin^2 2\alpha}{\gamma_0} - \cos 2\alpha = \tan^2 \xi. \tag{6.114}$$

As shown in 6.12e, the degenerate minimum has the shape of a cross close to the origin, and the direction of the arms is determined by this equation. To solve it, we need the left hand side to be positive, and the continuously degenerate minimum therefore appears at

$$\lambda^2 \sin^2 2\alpha - \gamma_0 \cos 2\alpha = 0 \tag{6.115}$$

Solving for λ gives

$$\lambda = -\cot^2 2\alpha + \cot^2 2\alpha \sqrt{1 + \frac{\sin^2 2\alpha}{\cos^3 2\alpha}\left(\frac{1}{2} + \frac{3}{2}\cos 2\alpha\right)}. \tag{6.116}$$

The formation of the continuously degenerate minimum leads to existence of costless excitation modes at finite quasimomentum vectors, which may destroy the ferromagnetic ordering. We should however keep in mind that we have neglected interaction between the Holstein-Primakoff bosons. In analogy with the Rashba degenerate minimum in the continuum BEC discussed in section 3.3, interactions may reduce the massive degeneracy [22, 96]. Appearance of the continuous degeneracy is in any case indicative that something happens.

Aligning spins in the xy-plane allows the Dzyaloshinskii-Moriya term to contribute to the excitation spectrum to lowest order in the spin wave expansion. We have shown that this causes relatively large quantum fluctuations, and that it breaks the classical ground state degeneracy in favour of alignment in the x- or y-direction. At sufficiently large Dzyaloshinskii-Moriya interaction strength, the formation of a continuously degenerate minimum allows for costless excitations possibly destroying ferromagnetic ordering, and hence reducing the xy-ferromagnet region in parameter space.

6.4.4 Stripe phase excitation spectrum

For the vortex family states in figure 6.2c, one should in principle introduce four different bosons on the four sublattices with different spin orientation. For simplicity, we consider the stripe phase, where it suffices to introduce different boson operators a and b on the two sublattices A and B with opposite magnetic ordering in figure 6.2d. Make a rotation

$$S^y \to S^z \qquad S^z \to -S^y \qquad S^x \to S^x, \tag{6.117}$$

so that in the new coordinates, spins are aligned parallel or antiparallel to the spin space z-direction. The Hamiltonian is then

$$H = \sum_{i,\delta}\left\{J_\delta^x S_i^x S_{i+\delta}^x + J_\delta^y S_i^z S_{i+\delta}^z + J_\delta^z S_i^y S_{i+\delta}^y\right\} + \mathcal{D}\sum_i\left\{S_i^y S_{i+\hat{x}}^x - S_i^x S_{i+\hat{x}}^y + S_i^y S_{i+\hat{y}}^z - S_i^z S_{i+\hat{y}}^y\right\} \tag{6.118}$$

Similar to the calculation for the z-antiferromagnet, introduce the bosons so that

$$S^z_\alpha = S - a^\dagger_\alpha a_\alpha \qquad S^+_\alpha \simeq \sqrt{2S} a_\alpha \qquad S^-_\alpha \simeq \sqrt{2S} a^\dagger_\alpha \tag{6.119}$$

$$S^z_\beta = -S + b^\dagger_\beta b_\beta \qquad S^+_\beta \simeq \sqrt{2S} b^\dagger_\beta \qquad S^-_\beta \simeq \sqrt{2S} b_\beta, \tag{6.120}$$

for $\alpha \in A$ and $\beta \in B$, the only difference from the zAFM calculation being the definition of the sublattices. Since we use a real space unit cell with twice the original size in y-direction, this is associated with a Brillouin zone reduction to $-\pi/2 < q_y \leq \pi/2$.

After inserting the Holstein-Primakoff transformation with different bosons on the two sublattices in the above rotated Hamiltonian, insert Fourier transformed boson operators defined as

$$a_i = \sqrt{\frac{2}{N}} \sum_q e^{i\mathbf{q}\cdot\mathbf{r}_i} a_q, \tag{6.121}$$

$$b_i = \sqrt{\frac{2}{N}} \sum_q e^{-i\mathbf{q}\cdot\mathbf{r}_i} b_q. \tag{6.122}$$

This gives

$$
\begin{aligned}
H = E_0 + \frac{1}{2} \sum_q \Big\{ &(A_q + B_q)(a^\dagger_q a_q + b^\dagger_q b_q) + (A_q - B_q)(a^\dagger_{-q} a_{-q} + b^\dagger_{-q} b_{-q}) \\
&+ C_q(a^\dagger_q a^\dagger_{-q} + a_q a_{-q} + b^\dagger_q b^\dagger_{-q} + b_q b_{-q}) \\
&+ D_q(a^\dagger_q b_{-q} + a_q b^\dagger_{-q} + a^\dagger_{-q} b_q + a_{-q} b^\dagger_q) \\
&+ E_q(a^\dagger_q b^\dagger_q + a_q b_q + a^\dagger_{-q} b^\dagger_{-q} + a_{-q} b_{-q}) \Big\},
\end{aligned}
\tag{6.123}
$$

where the coefficients are

$$E_0 = NS^2(J^y_x - J^y_y) \tag{6.124}$$

$$A_q = -2S(J^y_x - J^y_y) + S(J^x_x + J^z_x)\cos q_x \tag{6.125}$$

$$B_q = -2\mathcal{D}S\sin q_x \tag{6.126}$$

$$C_q = S(J^x_x - J^z_x)\cos q_x \tag{6.127}$$

$$D_q = S(J^x_y - J^z_y)\cos q_y \tag{6.128}$$

$$E_q = S(J^x_y + J^z_y)\cos q_y. \tag{6.129}$$

We can express the coefficients in terms of the original boson model parameters α and λ, obtaining

$$A_q = 2S\left(\frac{4t_0^2}{\lambda u}\right)(1 - \cos 2\alpha - \lambda\cos 2\alpha\cos q_x) \tag{6.130}$$

$$B_q = -2S\left(\frac{4t_0^2}{\lambda u}\right)\lambda\sin 2\alpha\sin q_x \tag{6.131}$$

$$C_q = 2S\left(\frac{4t_0^2}{\lambda u}\right)(\lambda - 1)\cos 2\alpha\cos q_x \tag{6.132}$$

$$D_q = -S\left(\frac{4t_0^2}{\lambda u}\right)[1 - (2\lambda - 1)\cos 2\alpha]\cos q_y \tag{6.133}$$

$$E_q = -S\left(\frac{4t_0^2}{\lambda u}\right)[1 + (2\lambda - 1)\cos 2\alpha]\cos q_y. \tag{6.134}$$

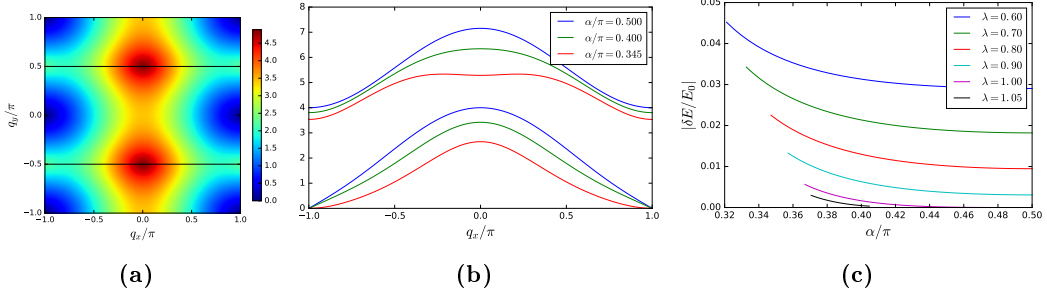**(a)**　　　　　　　　　　　　　**(b)**　　　　　　　　　　　　　**(c)**

Figure 6.13: Figure (a) shows the stripe phase excitation spectrum eigenvalue ω_q^- at $\lambda = 0.8$ and $\alpha/\pi = 0.4$, where the black lines indicate the reduced Brillouin zone. Figure (b) shows typical dispersion relations along $q_y = 0$ at $\lambda = 0.8$. The dispersion relation is linear around minima at $q_x = \pm\pi$ with a slope that is decreasing with α. For sufficiently small α the energy turns imaginary, corresponding to an instability. Figure (c) shows quantum corrections δE normalized to the ground state energy E_0 in the stable regime.

For each Fourier mode inside the reduced Brillouin zone, we can again write the Hamiltonian in matrix form, obtaining,

$$H = E_0 + \frac{1}{2} \sum_q \left(\frac{1}{2} \psi_q^\dagger M_q \psi_q - 2A_q \right). \tag{6.135}$$

We choose ψ_q as

$$\psi_q^\dagger = \begin{pmatrix} a_q^\dagger & b_{-q}^\dagger & a_{-q} & b_q & a_q & b_{-q} & a_{-q}^\dagger & b_q^\dagger \end{pmatrix} \tag{6.136}$$

to be able to write M_q on the block diagonal form

$$M_q = \begin{pmatrix} N_q & 0 \\ 0 & N_q \end{pmatrix}, \tag{6.137}$$

where N_q is the 4x4-matrix

$$N_q = \begin{pmatrix} A_q + B_q & D_q & C_q & E_q \\ D_q & A_q - B_q & E_q & C_q \\ C_q & E_q & A_q - B_q & D_q \\ E_q & C_q & D_q & A_q + B_q \end{pmatrix}. \tag{6.138}$$

The eigenvalues of the dynamic matrix $\tilde{M}_q$ are

$$\omega_q^\pm = \left[A_q^2 + B_q^2 + D_q^2 - C_q^2 - E_q^2 \pm 2\sqrt{A_q^2 B_q^2 - B_q^2 C_q^2 + A_q^2 D_q^2 - 2A_q C_q D_q E_q + C_q^2 E_q^2} \right]^{1/2}. \tag{6.139}$$

The Hamiltonian can now be written as

$$H = E_0 + \frac{1}{2} \sum_q (\omega_q^+ + \omega_q^- - 2A_q) + \sum_q (\omega_q^+ \alpha_q^\dagger \alpha_q + \omega_q^- \beta_q^\dagger \beta_q), \tag{6.140}$$

where α_q and β_q are boson operators.

Typical dispersion relations along $q_y = 0$ are plotted in figure 6.13b for $\lambda = 0.8$, while the Brillouin zone structure of the lowest band is illustrated in figure 6.13a for $\alpha/\pi = 0.4$. The minima

are located at $\mathbf{q} = (\pm\pi, 0)$, and except for the single point $(\alpha, \lambda) = (\pi/2, 1)$, the dispersion relation is linear around these points. The slope decreases with gauge field strength α, and at a critical point, the eigenvalue turns imaginary. This corresponds to an instability and breakdown of the stripe phase, and is marked with a red line on top of the variational phase diagram in figure 6.9. The stripe phase parameter space region is therefore significantly reduced by quantum fluctuations. In figure 6.13c, we plot the quantum corrections in the Hamiltonian (6.140) inside the stable region. The quantum fluctuations are rather large, and of the same order as in the xyFM state. The magnitude increases with decreasing α and λ because this strengthens the Dzyaloshinskii-Moriya interaction and z-component Heisenberg coupling relative to the planar couplings J_δ^x and J_δ^y.

6.4.5   Summary and related works

In the final section of this chapter, we summarize the excitation spectrum results to lowest order in the spin wave expansion and discuss the some very recent articles.

For the zFM phase, we introduce one type of boson. Although the Dzyaloshinskii-Moriya interaction does not contribute to the non-interacting Holstein-Primakoff excitation spectrum, the anisotropies in the Heisenberg term introduce small quantum fluctuations not present in the isotropic case. In return, a gap in the dispersion relation protects the phase against thermal fluctuations. For the zAFM phase, we need to introduce two different bosons. Apart from this, the situation is almost exactly the same as for the zFM state, there is no contribution from the Dzyaloshinskii-Moriya term, a gapped dispersion relation, and small quantum fluctuations. A notable difference from the Néel state of the isotropic AFM Heisenberg model, is that the dispersion minima are at $\mathbf{q} = (\pm\pi, 0)$ and $\mathbf{q} = (0, \pm\pi)$ instead of $\mathbf{q} = 0$. The xyFM and stripe phases are planar in the xy-plane, and the Dzyaloshinskii-Moriya interaction therefore contributes to the excitation spectrum. This gives rather large quantum fluctuations and a significant reduction of the stripe and xyFM regions in the phase diagram. There is no gap to lowest order in the spin wave expansion, and the excitation spectra are linear around the minima.

Two very recent articles discuss similar matters, and are of special interest.

Wang *et al.* [148] applied the recently developed technique of string bond states [152], which is a tensor network method generalizing the density matrix renormalization group method used in one dimension [153, 154]. Our results are largely in accordance with the simulations there. For the zFM and zAFM states, they find that quantum corrections to the ground state energy are negligible. For the xyFM and vortex family states, they find that the classical continuous degeneracy is lifted in favour of spin ordering along the x- or y-direction, and note that this is known as the order by disorder mechanism [155, 156]. Quantum fluctuations reduce the size of the xFM/yFM and stripe phase regions, but less dramatic than in our calculations.

Sun *et al.* [147] treats the case of spin-independent interaction ($\lambda = 1$) with Holstein-Primakoff transformation on the stripe phase. We may compare our dispersion relation result with $\lambda = 1$ with theirs at Rashba SOC, obtaining full agreement when letting $q_x \leftrightarrow q_y$ corresponding to different conventions in the definition of the SOC. Sun *et al.* introduce the four bosons required to analyse the the general vortex-family state, finding that the classical degeneracy is lifted in favour of the states with spin-ordering in the x- or y-directions, analogous to our xyFM result and in agreement with the simulations in Wang *et al.*. Sun *et. al* also remark that the stripe phase excitation spectrum is gapless only to lowest order in the spin wave expansion, and re-introduce it through a spin coherent state analysis. As a result of this, the breakdown of the stripe phase requires stronger Dzyaloshinskii-Moriya interaction. We expect that a similar analysis at $\lambda \neq 1$ will lead to better agreement between the Holstein-Primakoff result and the quantum simulations in Wang *et al.* [148]. The xyFM phase is not treated in Sun *et al.* because it reduces to the single point $\alpha = 0$ when $\lambda = 1$.

Chapter 7

Summary and outlook

In this thesis, we have studied two-component spin-orbit coupled ultracold bosonic atoms on a two-dimensional square optical lattice. These systems are particularly interesting because their tunability and absence of impurities allow simulation of condensed matter systems, but also the study of novel phenomena through access to parameter regimes otherwise hard to reach. After introducing the theoretical and experimental concepts behind the realization of these systems, we derive a Bose-Hubbard model in the tight-binding approximation, and include only nearest neighbour hopping and on-site interaction. Following an introductory discussion on the superfluid to Mott insulator transition, we consider the two extreme limits of weak and strong interaction, focusing on phase separation effects and spin textures.

In the weakly coupled regime, we use a real space uniform density mean field theory to decouple the interaction. After diagonalizing the single particle problem, we solve the self-consistent equations for component imbalance, and obtain a phase diagram for the phase separation transition as function of spin-orbit coupling strength and inter- relative to intracomponent interaction. At finite temperature, the system shows an expected remixing of the components in the phase separated regime, but also a more surprising entropy driven phase separation in the mixed regime. Both effects can be understood through interpretation of imbalance as an effective Zeeman field in the mean field Hamiltonian. We also provide an explanation in terms of locking between momentum and imbalance.

In the strongly interacting regime, we derive an effective spin model describing spin textures in the Mott insulator. In addition to an anisotropic Heisenberg term, we find Dzyaloshinskii-Moriya interaction. Based on classical Monte-Carlo simulations in the literature [102, 104, 129], we use a variational approach in real and Fourier space to reconstruct the phase diagram, which shows ferromagnetic, antiferromagnetic, spiral, stripe, vortex, and skyrmion phases. Quantum fluctuations are analysed with the Holstein-Primakoff transformation to lowest order in the spin wave expansion. For the phases with ferromagnetic or antiferromagnetic alignment in the z-direction corresponding to components in the pseudo-spin description, quantum fluctuations are small, and thermal fluctuations are suppressed by a gap. For the xy-planar states with particles at each lattice site in an equal superposition of the two components, there are substantial quantum fluctuations which may destroy ordering, and hence distort the classical phase diagram. The dispersion relation is linear around gapless minima to lowest order in the spin wave expansion.

In the weakly coupled regime, an extension of the real space mean field theory should focus on generalization to spatially inhomogeneous phases, since these are known to occur in certain parameter regimes [100, 104, 122]. In particular, it would be interesting to see if entropy driven phase separation persists also for the transition from a stripe phase, and how it is potentially changed. One may analyse bond current correlation functions using the transformed boson operators, trying to reproduce the antiferromagnetic pattern of current loops shown to be present in our

and in similar systems [104, 125]. Other possible topics for further exploration include solving the self-consistent equations for uneven combinations of Rashba and Dresselhaus spin-orbit coupling, the inclusion of an effective in-plane electric field $k_\delta \sigma_z$, and mapping out in more detail the phase diagram for the transition driven by the joint effort of interactions and the Zeeman field. One may also study the problem in the boson path integral formalism. When analysing the phase separation transition in mean field theory, one neglects quantum fluctuations in the problem. Many articles, for instance Refs. [100, 104, 120, 122], rest on either mean field theories or classical Monte-Carlo simulation, but a treatment of quantum fluctuations is necessary for the results to be entirely trusted. Particularly interesting would be the effect of quantum fluctuations on the entropy driven phase separation.

In the strongly coupled regime, one may improve the variational phase diagram by introducing a more general skyrmion phase. In addition, one may consider spiral-2 phases with periodicity larger than 6. For the possible incommensurate spiral-2 phase, an improvement would be to allow for spins to twist toward the direction with dominant Heisenberg coupling by introducing secondary Fourier modes. The excitation spectra of the vortex, commensurate spiral, and skyrmion phases can be analysed by introducing additional bosons. Making a position dependent rotation of the coordinate system could provide possibilities for studying the excitation spectra of the incommensurate spiral phases. One may also investigate the use of Schwinger bosons. While in literature, one has typically studied either the general linear combination of Rashba and Dresselhaus SOC with spin-independent interaction or Rashba SOC with spin-dependent interaction, one could also study the effective spin model in the most general case.

A different possibility is to study the model slightly away from half-filling, where real hopping processes are possible since not all lattice sites are occupied. For fermions, this can be done with the t-J model [157], which has been used to study lightly doped Mott insulators in high-T_c superconductors [158]. The bosonic version of this should also be a very interesting problem [159–162].

Appendix A

Methods for determining variational parameters

In this appendix, we show that the two methods for determining the variational parameters in section 5.2 are equivalent. The argument is based on Ref. [123]. The methods are:

- Minimizing the free energy with respect to the expectation values.

- Obtaining a self-consistent equation by calculating the given expectation values within the mean field approximation.

Given a mean field Hamiltonian H_{MF}, the partition function is $Z_{\mathrm{MF}} = \mathrm{Tr}\, e^{-\beta H_{\mathrm{MF}}}$. The minimization method can be expressed as

$$0 = \frac{\partial \Omega}{\partial n_{0\rho}} = \frac{\partial}{\partial n_{0\rho}} \left(-\frac{1}{\beta} \log Z_{\mathrm{MF}} \right) \tag{A.1}$$

$$= \frac{1}{Z_{\mathrm{MF}}} \mathrm{Tr} \left[e^{-\beta H_{\mathrm{MF}}} \frac{\partial}{\partial n_{0\rho}} H_{\mathrm{MF}} \right], \tag{A.2}$$

where we have used

$$\frac{\partial}{\partial x} \mathrm{Tr}\, O(x) = \mathrm{Tr} \left[\frac{\partial}{\partial x} O(x) \right]. \tag{A.3}$$

Since only the mean field interaction in the Hamiltonian (5.6) depends on $n_{0\sigma}$, we get

$$\frac{\partial H_{\mathrm{MF}}}{\partial n_{0\rho}} = -N \sum_{\sigma} u_{\rho\sigma} n_{0\sigma} + \sum_{i\sigma} u_{\rho\sigma} n_{i\sigma} = \sum_{i,\sigma} u_{\rho\sigma}(n_{i\sigma} - n_{0\sigma}).$$

Inserting this in the minimization condition (A.2), we get

$$n_{0\sigma} = \frac{1}{N} \sum_i \langle n_{i\sigma} \rangle, \tag{A.4}$$

which is exactly the self-consistent equation occurring when we calculate the average occupation from within mean field theory.

Appendix B

Complete spin model derivation

In section 6.1, we outlined the derivation of the effective spin model describing magnetic textures in the Mott insulator. In this appendix, we fill in the missing steps and complete the derivation.

The Hamiltonian can be written as a sum of contributions H_{eff}^s and H_{eff}^d corresponding to terms in the energy correction where virtual hopping processes produce states in the s- and d-subspaces. These correspond to states where the single doubly occupied lattice site has bosons of the same and of different species. For $r \in \{s, d\}$, we have shown

$$H_{\text{eff}}^r = -\frac{1}{u_r} \sum_{\langle ij \rangle \alpha\beta\gamma\delta} \left[-\delta_{\alpha\beta} t + \delta_{\alpha,-\beta} s_{ij}^{\alpha\beta} \right] \left[-\delta_{\gamma\delta} t + \delta_{\gamma,-\delta} s_{ji}^{\gamma\delta} \right] a_{i\alpha}^{\dagger} a_{j\beta} P_r a_{j\gamma}^{\dagger} a_{i\delta}. \tag{B.1}$$

We now write out all terms in the Hamiltonian giving a non-zero second order contribution to the ground state energy. In this appendix, two operators are therefore considered equal if they give the same result when acting on the space of ground states of the non-perturbed Hamiltonian in the subspace we are considering, even if they are not equal on the full Hilbert space. Recall also that we have introduced operator notation

$$|\alpha\beta|\gamma\delta, \epsilon| = a_{i\alpha}^{\dagger} a_{i\beta} a_{j\gamma}^{\dagger} a_{j\delta} n_{j\epsilon}, \tag{B.2}$$

We let a single $|\uparrow|$ denote the corresponding number operator. We consider the s- and d-subspaces separately.

B.1 Same species subspace

The correction ΔE_2^s to the energy from the virtual hoppings which produce a state belonging to the s-subspace is $\Delta E_2^s = \langle \psi_0 | H_{\text{eff}}^s | \psi_0 \rangle$, where

$$H_{\text{eff}}^s = -\frac{1}{u} \sum_{\langle ij \rangle \alpha\beta\gamma\delta} \left[-\delta_{\alpha\beta} t + \delta_{\alpha,-\beta} s_{ij}^{\alpha\beta} \right] \left[-\delta_{\gamma\delta} t + \delta_{\gamma,-\delta} s_{ji}^{\gamma\delta} \right] a_{i\alpha}^{\dagger} a_{j\beta} P_s a_{j\gamma}^{\dagger} a_{i\delta}. \tag{B.3}$$

As discussed in the main text, we use the operator identity

$$a_{i\alpha}^{\dagger} a_{j\beta} P_s a_{j\gamma}^{\dagger} a_{i\delta} = a_{i\alpha}^{\dagger} a_{i\delta} (\delta_{\beta\gamma} + a_{j\gamma}^{\dagger} a_{j\beta}) n_{j\gamma} \tag{B.4}$$

From the square bracket product in (B.3), we obtain three types of terms, tt, ts, and ss. We can then write

$$H_{\text{eff}}^s = H_{\text{eff}}^{s,\text{tt}} + H_{\text{eff}}^{s,\text{ss}} + H_{\text{eff}}^{s,\text{ts}}. \tag{B.5}$$

Consider each of these terms separately.

B.1.1   tt-terms

For tt-terms, the Hamiltonian becomes

$$
\begin{aligned}
H_{\text{eff}}^{\text{s,tt}} &= -\frac{t^2}{u} \sum_{\langle ij \rangle, \alpha\beta\gamma\delta} \delta_{\alpha\beta}\delta_{\gamma\delta} \left(a_{i\alpha}^{\dagger} a_{i\delta} \delta_{\beta\gamma} n_{j\gamma} + a_{i\alpha}^{\dagger} a_{i\delta} a_{j\gamma}^{\dagger} a_{j\beta} n_{j\gamma} \right) \\
&= -\frac{t^2}{u} \sum_{\langle ij \rangle, \alpha} a_{i\alpha}^{\dagger} a_{i\alpha} n_{j\alpha} - \frac{t^2}{u} \sum_{\langle ij \rangle, \alpha\gamma} a_{i\alpha}^{\dagger} a_{i\gamma} a_{j\gamma}^{\dagger} a_{j\alpha} n_{j\gamma} \\
&= -\frac{t^2}{u} \sum_{\langle ij \rangle} (2|\uparrow|\uparrow| + 2|\downarrow|\downarrow| + |\uparrow\downarrow|\downarrow,\downarrow| + |\downarrow\uparrow|\uparrow\downarrow,\uparrow|) \\
&= -\frac{t^2}{4u} \sum_{\langle ij \rangle} \left[2(1 + \sigma_i^z)(1 + \sigma_j^z) + 2(1 - \sigma_i^z)(1 - \sigma_j^z) \right] \\
&= -\frac{t^2}{u} \sum_{\langle ij \rangle} (1 + \sigma_i^z \sigma_j^z),
\end{aligned}
$$

where we have used that $|\uparrow\downarrow,\uparrow| = |\downarrow\uparrow,\downarrow| = 0$.

B.1.2   ss-terms

For the ss-terms, we get

$$
\begin{aligned}
H_{\text{eff}}^{\text{s,ss}} &= -\frac{1}{u} \sum_{\langle ij \rangle, \alpha\beta\gamma\delta} \delta_{\alpha,-\beta} \delta_{\gamma,-\delta} s_{ij}^{\alpha\beta} s_{ji}^{\gamma\delta} \left(a_{i\alpha}^{\dagger} a_{i\delta} \delta_{\beta\gamma} n_{j\gamma} + a_{i\alpha}^{\dagger} a_{i\delta} a_{j\gamma}^{\dagger} a_{j\beta} n_{j\gamma} \right) \\
&= -\frac{1}{u} \sum_{\langle ij \rangle, \alpha\gamma} |s_{ij}^{\alpha,-\alpha}|^2 a_{i\alpha}^{\dagger} a_{i\alpha} n_{j,-\alpha} + s_{ij}^{\alpha,-\alpha} s_{ji}^{\gamma,-\gamma} a_{i\alpha}^{\dagger} a_{i,-\gamma} a_{j\gamma}^{\dagger} a_{j,-\alpha} n_{j\gamma} \\
&= -\frac{1}{u} \sum_{\langle ij \rangle} |s_{ij}^{\uparrow\downarrow}|^2 \left(|\uparrow|\downarrow| + |\downarrow|\uparrow| + |\uparrow\uparrow|\downarrow\downarrow,\downarrow| + |\downarrow\downarrow|\uparrow\uparrow,\uparrow| \right) \\
&= -\frac{1}{4u} \sum_{\langle ij \rangle} |s_{ij}^{\uparrow\downarrow}|^2 \left(2(1 + \sigma_i^z)(1 - \sigma_j^z) + 2(1 - \sigma_i^z)(1 + \sigma_j^z) \right) \\
&= -\frac{1}{u} \sum_{\langle ij \rangle} |s_{ij}^{\uparrow\downarrow}|^2 (1 - \sigma_i^z \sigma_j^z)
\end{aligned}
$$

by using again $|\uparrow\downarrow,\uparrow| = |\downarrow\uparrow,\downarrow| = 0$.

B.1.3   ts-terms

Finally, the ts-terms give

$$
\begin{aligned}
H_{\text{eff}}^{\text{s,ts}} &= \frac{t}{u} \sum_{\langle ij \rangle, \alpha\beta\gamma\delta} \left(\delta_{\alpha\beta}\delta_{\gamma,-\delta} s_{ji}^{\gamma\delta} + \delta_{\alpha,-\beta}\delta_{\gamma\delta} s_{ij}^{\alpha\beta} \right) \left(a_{i\alpha}^\dagger a_{i\delta} \delta_{\beta\gamma} n_{j\gamma} + a_{i\alpha}^\dagger a_{i\delta} a_{j\gamma}^\dagger a_{j\beta} n_{j\gamma} \right) \\
&= \frac{t}{u} \sum_{\langle ij \rangle, \alpha\gamma} \Bigg[s_{ji}^{\alpha,-\alpha} a_{i\alpha}^\dagger a_{i,-\alpha} n_{j\alpha} \delta_{\alpha\gamma} + s_{ji}^{\gamma;-\gamma} a_{i\alpha}^\dagger a_{i,-\gamma} a_{j\gamma}^\dagger a_{j\alpha} n_{j\gamma} \\
&\qquad\qquad + s_{ij}^{\alpha,-\alpha} \left(a_{i\alpha}^\dagger a_{i,-\alpha} n_{j,-\alpha} \delta_{\alpha,-\gamma} + a_{i\alpha}^\dagger a_{i\gamma} a_{j\gamma}^\dagger a_{j,-\alpha} n_{j\gamma} \right) \Bigg] \\
&= \frac{t}{u} \sum_{\langle ij \rangle} \Bigg[s_{ji}^{\uparrow\downarrow} \left(2 | \uparrow\downarrow \rangle | \uparrow | + | \downarrow\downarrow \rangle | \uparrow\downarrow, \uparrow | \right) + s_{ji}^{\downarrow\uparrow} \left(2 | \downarrow\uparrow \rangle | \downarrow | + | \uparrow\uparrow \rangle | \downarrow\uparrow, \downarrow | \right) \\
&\qquad\qquad + s_{ij}^{\uparrow\downarrow} \left(2 | \uparrow\downarrow \rangle | \downarrow | + | \downarrow\downarrow \rangle | \downarrow\uparrow, \downarrow | \right) + s_{ij}^{\downarrow\uparrow} \left(2 | \downarrow\uparrow \rangle | \uparrow | + | \downarrow\downarrow \rangle | \downarrow\uparrow, \downarrow | \right) \Bigg] \\
&= \frac{2t}{u} \sum_{\langle ij \rangle} \Bigg[s_{ji}^{\uparrow\downarrow} | \uparrow\downarrow \rangle | \uparrow | + s_{ji}^{\downarrow\uparrow} | \downarrow\uparrow \rangle | \downarrow | + s_{ij}^{\uparrow\downarrow} | \uparrow\downarrow \rangle | \downarrow | + s_{ij}^{\downarrow\uparrow} | \downarrow\uparrow \rangle | \uparrow | \Bigg] \\
&= \frac{t}{2u} \sum_{\langle ij \rangle} \Bigg[s_{ji}^{\uparrow\downarrow} \sigma_i^+ (1 + \sigma_j^z) + s_{ji}^{\downarrow\uparrow} \sigma_i^- (1 - \sigma_j^z) + s_{ij}^{\uparrow\downarrow} \sigma_i^+ (1 - \sigma_j^z) + s_{ij}^{\downarrow\uparrow} \sigma_i^- (1 + \sigma_j^z) \Bigg].
\end{aligned}
$$

Use the symmetry properties of $s_{ij}^{\sigma\sigma'}$ to express all spin-orbit coupling coefficients in terms of $s_{ij}^{\uparrow\downarrow}$. After several cancellations, we are left with

$$
H_{\text{eff}}^{\text{s,ts}} = -\frac{t}{u} \sum_{\langle ij \rangle} \sigma_j^z \left(s_{ij}^{\uparrow\downarrow} \sigma_i^+ + (s_{ij}^{\uparrow\downarrow})^* \sigma_i^- \right).
$$

Use now the antisymmetry of $s_{ij}^{\uparrow\downarrow}$ under $i \leftrightarrow j$ and $s_\delta = s_{ij}^{\uparrow\downarrow}$ to express this as

$$
H_{\text{eff}}^{\text{s,ts}} = \frac{t}{u} \sum_{i,\delta} \left[\sigma_i^z (s_\delta \sigma_{i+\delta}^+ + s_\delta^* \sigma_{i+\delta}^-) - \sigma_{i+\delta}^z (s_\delta \sigma_i^+ + s_\delta^* \sigma_i^-) \right],
$$

and insert

$$
s_\delta \sigma_{i+\delta}^+ + s_\delta^* \sigma_{i+\delta}^- = 2 \operatorname{Re}(s_\delta) \sigma_{i+\delta}^x - 2 \operatorname{Im}(s_\delta) \sigma_{i+\delta}^y
$$

in the Hamiltonian. We then obtain

$$
\begin{aligned}
H_{\text{eff}}^{\text{s,ts}} &= \frac{2t}{u} \sum_{i,\delta} \left[\operatorname{Re}(s_\delta) \left(\sigma_i^z \sigma_{i+\delta}^x - \sigma_{i+\delta}^z \sigma_i^x \right) - \operatorname{Im}(s_\delta) \left(\sigma_i^z \sigma_{i+\delta}^y - \sigma_{i+\delta}^z \sigma_i^y \right) \right] \\
&= \frac{2t}{u} \sum_{i,\delta} \left[\operatorname{Re}(s_\delta) \hat{y} \cdot \vec{\sigma}_i \times \vec{\sigma}_{i+\delta} + \operatorname{Im}(s_\delta) \hat{x} \cdot \vec{\sigma}_i \times \vec{\sigma}_{i+\delta} \right].
\end{aligned} \tag{B.6}
$$

B.2 Different species subspace

We now perform the analogous calculation for the d-subspace. In the arrow-representation of the operators, this corresponds to switching the orientation of the last spin.

B.2.1 tt-terms

The tt-terms give

$$
\begin{aligned}
H_{\text{eff}}^{\text{s,tt}} &= -\frac{t^2}{u} \sum_{\langle ij \rangle, \alpha} a_{i\alpha}^\dagger a_{i\alpha} n_{j,-\alpha} - \frac{t^2}{u} \sum_{\langle ij \rangle, \alpha\gamma} a_{i\alpha}^\dagger a_{i\gamma} a_{j\gamma}^\dagger a_{j\alpha} n_{j,-\gamma} \\
&= -\frac{t^2}{u} \sum_{\langle ij \rangle} \left(|\uparrow| \downarrow| + |\downarrow| \uparrow| + |\uparrow\downarrow| \downarrow\uparrow, \uparrow| + |\downarrow\uparrow| \uparrow\downarrow, \downarrow| \right) \\
&= -\frac{t^2}{4u} \sum_{\langle ij \rangle} \left[(1 + \sigma_i^z)(1 - \sigma_j^z) + (1 - \sigma_i^z)(1 + \sigma_j^z) + \sigma_i^+ \sigma_j^- + \sigma_i^- \sigma_j^+ \right] \\
&= -\frac{t^2}{2u} \sum_{\langle ij \rangle} (1 - \sigma_i^z \sigma_j^z + \sigma_i^x \sigma_j^x + \sigma_i^y \sigma_j^y),
\end{aligned}
$$

where we have left out the zero-terms with $|\uparrow\uparrow, \downarrow| = 0$ in the intermediate steps.

B.2.2 ss-terms

For the ss-terms,

$$
\begin{aligned}
H_{\text{eff}}^{\text{s,ss}} &= -\frac{1}{u} \sum_{\langle ij \rangle, \alpha\gamma} \left[|s_{ij}^{\alpha,-\alpha}|^2 a_{i\alpha}^\dagger a_{i\alpha} n_{j,\alpha} + s_{ij}^{\alpha,-\alpha} s_{ji}^{\gamma,-\gamma} a_{i\alpha}^\dagger a_{i,-\gamma} a_{j\gamma}^\dagger a_{j,-\alpha} n_{j,-\gamma} \right] \\
&= -\frac{1}{u} \sum_{\langle ij \rangle} \left[|s_{ij}^{\uparrow\downarrow}|^2 \left(|\uparrow| \uparrow| + |\downarrow| \downarrow| \right) + s_{ij}^{\uparrow\downarrow} s_{ji}^{\uparrow\downarrow} |\uparrow\downarrow| \uparrow\downarrow, \downarrow| + s_{ij}^{\downarrow\uparrow} s_{ji}^{\downarrow\uparrow} |\downarrow\uparrow| \uparrow\downarrow, \uparrow| \right] \\
&= -\frac{1}{4u} \sum_{\langle ij \rangle} \left[2 |s_{ij}^{\uparrow\downarrow}|^2 (1 + \sigma_i^z \sigma_j^z) + s_{ij}^{\uparrow\downarrow} s_{ji}^{\uparrow\downarrow} \sigma_i^+ \sigma_j^+ + s_{ij}^{\downarrow\uparrow} s_{ji}^{\downarrow\uparrow} \sigma_i^- \sigma_j^- \right].
\end{aligned}
$$

We again use the symmetry properties of $s_{ij}^{\alpha\beta}$, and obtain $s_{ij}^{\uparrow\downarrow} s_{ji}^{\uparrow\downarrow} = -s_\delta^2$ and $s_{ij}^{\downarrow\uparrow} s_{ji}^{\downarrow\uparrow} = -(s_\delta^*)^2$. One may then write the Hamiltonian as

$$
H_{\text{eff}}^{\text{s, ss}} = -\frac{1}{4u} \sum_{\langle ij \rangle} \left[2|s_m|^2 (1 + \sigma_i^z \sigma_j^z) - (s_m^2 + (s_m^*)^2)(\sigma_i^x \sigma_j^x - \sigma_i^y \sigma_j^y) - (s_m^2 - (s_m^*)^2)(\sigma_i^x \sigma_j^y + \sigma_i^y \sigma_j^x) \right]
$$
(B.7)

$$
= -\frac{1}{2u} \sum_{\langle ij \rangle} \left[|s_m|^2 (1 + \sigma_i^z \sigma_j^z) - \text{Re}(s_m^2)(\sigma_i^x \sigma_j^x - \sigma_i^y \sigma_j^y) + \text{Im}(s_m^2)(\sigma_i^x \sigma_j^y + \sigma_i^y \sigma_j^x) \right]. \tag{B.8}
$$

As pointed out in the main text, the term with coupling between x- and y-components of the spin vanish for diagonal or off-diagonal SOC-matrix β_{lm}.

B.2.3 ts-terms

For the ts-terms, we obtain

$$
\begin{aligned}
H_{\text{eff}}^{\text{s,ts}} = {} & \frac{t}{u} \sum_{\langle ij \rangle, \alpha\gamma} \Bigg[s_{ij}^{\alpha,-\alpha} \left(a_{i\alpha}^{\dagger} a_{i\gamma} n_{j,\alpha} \delta_{\alpha,-\gamma} + a_{i\alpha}^{\dagger} a_{i\gamma} a_{j\gamma}^{\dagger} a_{j,-\alpha} n_{j,-\gamma} \right) \\
& + s_{ji}^{\gamma;-\gamma} \left(\delta_{\alpha\gamma} a_{i\alpha}^{\dagger} a_{i,-\gamma} n_{j,-\gamma} \delta_{\alpha\gamma} + a_{i\alpha}^{\dagger} a_{i,-\gamma} a_{j\gamma}^{\dagger} a_{j\alpha} n_{j,-\gamma} \right) \Bigg] \\
= {} & \frac{t}{u} \sum_{\langle ij \rangle} \Bigg[s_{ji}^{\uparrow\downarrow} \left(|\uparrow\downarrow|\downarrow| + |\downarrow\downarrow|\uparrow\downarrow,\downarrow| \right) + s_{ji}^{\downarrow\uparrow} \left(|\downarrow\uparrow|\uparrow| + |\uparrow\uparrow|\downarrow\uparrow,\uparrow| \right) \Bigg] \\
& + s_{ij}^{\uparrow\downarrow} \left(|\uparrow\downarrow|\uparrow| + |\uparrow\uparrow|\uparrow\downarrow,\downarrow| \right) + s_{ij}^{\downarrow\uparrow} \left(|\downarrow\uparrow|\downarrow| + |\downarrow\downarrow|\downarrow\uparrow,\uparrow| \right) \\
= {} & \frac{t}{2u} \sum_{\langle ij \rangle} \Bigg[s_{ji}^{\uparrow\downarrow} \left(\sigma_i^+ (1-\sigma_j^z) + (1-\sigma_i^z)\sigma_j^+ \right) + s_{ji}^{\downarrow\uparrow} \left(\sigma_i^+ (1-\sigma_j^z) + (1-\sigma_i^z)\sigma_j^+ \right) \\
& + s_{ij}^{\uparrow\downarrow} \left(\sigma_i^+ (1+\sigma_j^z) + (1+\sigma_i^z)\sigma_j^+ \right) + s_{ij}^{\downarrow\uparrow} \left(\sigma_i^- (1-\sigma_j^z) + (1-\sigma_i^z)\sigma_j^- \right) \Bigg] \\
= {} & \frac{t}{2u} \sum_{\langle ij \rangle} \left[\sigma_i^z (s_\delta \sigma_j^+ + s_\delta^* \sigma_j^-) + \sigma_j^z (s_\delta \sigma_i^+ + s_\delta^* \sigma_i^-) \right],
\end{aligned}
$$

where $\delta = j - i$. This expressions looks very similar to the expression we found for the ts-term in the calculation for the s-subspace, but since $s_\delta \to -s_\delta$ under $i \leftrightarrow j$, there is no contribution from this term at all,

$$
H_{\text{eff}}^{\text{d,ts}} = 0. \tag{B.9}
$$

This concludes the effective spin model derivation. We can now collect the terms and write down the final result

$$
H_{\text{eff}}^d = -\frac{t^2}{\lambda u} \sum_{i,\delta} \left(1 - \sigma_i^z \sigma_{i+\delta}^z + \sigma_i^x \sigma_{i+\delta}^x + \sigma_i^y \sigma_{i+\delta}^y \right) - \frac{1}{\lambda u} \sum_{i,\delta} |s_\delta|^2 (1 + \sigma_i^z \sigma_{i+\delta}^z) \tag{B.10}
$$

$$
+ \frac{1}{\lambda u} \sum_{i,\delta} \left[\text{Re}(s_\delta^2)(\sigma_i^x \sigma_{i+\delta}^x - \sigma_i^y \sigma_{i+\delta}^y) - \text{Im}(s_\delta^2)(\sigma_i^x \sigma_{i+\delta}^y + \sigma_i^y \sigma_{i+\delta}^x) \right] \tag{B.11}
$$

$$
H_{\text{eff}}^s = -\frac{2}{u} \sum_{i,\delta} \left[(t^2 - |s_\delta|^2)\sigma_i^z \sigma_{i+\delta}^z - t\,\text{Re}(s_\delta)\hat{y} \cdot \vec{\sigma}_i \times \vec{\sigma}_{i+\delta} - t\,\text{Im}(s_\delta)\hat{x} \cdot \vec{\sigma}_i \times \vec{\sigma}_{i+\delta} \right], \tag{B.12}
$$

as also reported in the main text.

Bibliography

[1] X.-G. Wen, *Quantum Field Theory of Many-Body Systems* (Oxford Graduate Texts, 2003).

[2] R. P. Feynman, Int. J. Theor. Phys. **21**, 467 (1982).

[3] I. Bloch, J. Dalibard, and S. Nascimbene, Nat Phys **8**, 267 (2012).

[4] W. Isaacson, *Einstein: His Life and Universe* (Simon and Schuster, 2007).

[5] S. N. Bose, Zeitschrift für Physik **26**, 178 (1924).

[6] A. Einstein, Sitzungsber. K.-Preuss. Akad. Wiss. **26**, 178 (1924).

[7] A. Einstein, Sitzungsber. K.-Preuss. Akad. Wiss. **1** (1925).

[8] J.-F. Allen and H. Jones, Nature **141**, 243 (1938).

[9] P. Kapitza, Nature **141**, 74 (1938).

[10] F. London, Nature **141**, 643 (1938).

[11] L. Pitaevskii and S. Stringari, *Bose-Einstein Condensation* (Clarendon Press, 2003).

[12] L. Landau, Phys. Rev. **60**, 356 (1941).

[13] C. J. Pethick and H. Smith, *Bose–Einstein Condensation in Dilute Gases*, 2nd ed. (Cambridge University Press, 2008).

[14] N. Bogoliubov, J. Phys (USSR) **11** (1947).

[15] E. H. Lieb, R. Seiringer, J. P. Solovej, and J. Yngvason, *The Mathematics of the Bose Gas and its Condensation* (Birkhäuser Basel, 2005).

[16] A. J. Leggett, *Quantum Liquids. Bose Condensation and Cooper Pairing in Condensed-Matter Systems* (Oxford University Press, 2006).

[17] O. Penrose and L. Onsager, Phys. Rev. **104**, 576 (1956).

[18] M. H. Anderson, J. R. Ensher, M. R. Matthews, C. E. Wieman, and E. A. Cornell, Science **269**, 198 (1995).

[19] K. B. Davis, M. O. Mewes, M. R. Andrews, N. J. van Druten, D. S. Durfee, D. M. Kurn, and W. Ketterle, Phys. Rev. Lett. **75**, 3969 (1995).

[20] W. Ketterle, Rev. Mod. Phys. **74**, 1131 (2002).

[21] E. A. Cornell and C. E. Wieman, Rev. Mod. Phys. **74**, 875 (2002).

[22] V. Galitski and I. B. Spielman, Nature **494**, 49 (2013).

[23] T. Volz, S. Dürr, S. Ernst, A. Marte, and G. Rempe, Phys. Rev. A **68**, 010702 (2003).

[24] I. Bloch, Nat Phys **1**, 23 (2005).

[25] C. J. Myatt, E. A. Burt, R. W. Ghrist, E. A. Cornell, and C. E. Wieman, Phys. Rev. Lett. **78**, 586 (1997).

[26] A. Manchon, H. C. Koo, J. Nitta, S. M. Frolov, and R. A. Duine, Nature Materials **14**, 871 (2015).

[27] R. Winkler, *Spin-orbit Coupling Effects in Two-Dimensional Electron and Hole Systems* (Springer, 2003).

[28] F. Schwabl, *Quantum Mechanics* (Springer-Verlag Berlin Heidelberg, 2002).

[29] G. Dresselhaus, Phys. Rev. **100**, 580 (1955).

[30] E. I. Rashba and V. I. Sheka, Fiz. Tverd. Tela: Collected Papers 2 , 162 (1959).

[31] G. Bihlmayer, O. Rader, and R. Winkler, New Journal of Physics **17**, 050202 (2015).

[32] Y. A. Bychkov and E. I. Rashba, Pis'ma Zh. Eksp. Teor. Fiz. **39** (1984).

[33] I. Žutić, J. Fabian, and S. Das Sarma, Rev. Mod. Phys. **76**, 323 (2004).

[34] C. L. Kane and E. J. Mele, Phys. Rev. Lett. **95**, 226801 (2005).

[35] M. Z. Hasan and C. L. Kane, Rev. Mod. Phys. **82**, 3045 (2010).

[36] P. Phillips, *Advanced Sollid State Physics* (Cambridge University Press, 2012).

[37] S.-C. Z. Xiao-Liang Qi, Physics Today **63** (2010), 10.1063/1.3293411.

[38] C. L. Kane and E. J. Mele, Phys. Rev. Lett. **95**, 146802 (2005).

[39] M. König, S. Wiedmann, C. Brüne, A. Roth, H. Buhmann, L. W. Molenkamp, X.-L. Qi, and S.-C. Zhang, Science **318**, 766 (2007).

[40] The Royal Swedish Academy of Sciences, "Topological phase transitions and topological phases of matter," (2016), Scientific Background on the Nobel Prize in Physics 2016.

[41] N. Nagaosa and Y. Tokura, Nat Nano **8**, 899 (2013).

[42] K. Osterloh, M. Baig, L. Santos, P. Zoller, and M. Lewenstein, Phys. Rev. Lett. **95**, 010403 (2005).

[43] J. Ruseckas, G. Juzeliūnas, P. Öhberg, and M. Fleischhauer, Phys. Rev. Lett. **95**, 010404 (2005).

[44] Y.-J. Lin, K. Jimenez-Garcia, and I. B. Spielman, Nature **471**, 83 (2011).

[45] L. W. Cheuk, A. T. Sommer, Z. Hadzibabic, T. Yefsah, W. S. Bakr, and M. W. Zwierlein, Phys. Rev. Lett. **109**, 095302 (2012).

[46] J.-Y. Zhang, S.-C. Ji, Z. Chen, L. Zhang, Z.-D. Du, B. Yan, G.-S. Pan, B. Zhao, Y.-J. Deng, H. Zhai, S. Chen, and J.-W. Pan, Phys. Rev. Lett. **109**, 115301 (2012).

[47] C. Hamner, Y. Zhang, M. A. Khamehchi, M. J. Davis, and P. Engels, Phys. Rev. Lett. **114**, 070401 (2015).

[48] Y. Zhang, G. Chen, and C. Zhang, Scientific Reports **3**, 1937 EP (2013).

[49] S.-C. Ji, J.-Y. Zhang, L. Zhang, Z.-D. Du, W. Zheng, Y.-J. Deng, H. Zhai, S. Chen, and J.-W. Pan, Nat Phys **10**, 314 (2014).

[50] J.-R. Li, J. Lee, W. Huang, S. Burchesky, B. Shteynas, F. Ç. Top, A. O. Jamison, and W. Ketterle, Nature **543**, 91 (2017).

[51] L. J. LeBlanc, M. C. Beeler, K. Jiménez-García, A. R. Perry, S. Sugawa, R. A. Williams, and I. B. Spielman, New Journal of Physics **15**, 073011 (2013).

[52] C. Qu, C. Hamner, M. Gong, C. Zhang, and P. Engels, Phys. Rev. A **88**, 021604 (2013).

[53] F. Schwabl, *Advanced Quantum Mechanics* (Springer Berlin Heidelberg, 2008).

[54] R. Gerritsma, G. Kirchmair, F. Zahringer, E. Solano, R. Blatt, and C. F. Roos, Nature **463**, 68 (2010).

[55] Z. Wu, L. Zhang, W. Sun, X.-T. Xu, B.-Z. Wang, S.-C. Ji, Y. Deng, S. Chen, X.-J. Liu, and J.-W. Pan, Science **354**, 83 (2016).

[56] M. Aidelsburger, Science **354**, 35 (2016).

[57] L. Huang, Z. Meng, P. Wang, P. Peng, S.-L. Zhang, L. Chen, D. Li, Q. Zhou, and J. Zhang, Nat Phys **12**, 540 (2016).

[58] Z. Meng, L. Huang, P. Peng, D. Li, L. Chen, Y. Xu, C. Zhang, P. Wang, and J. Zhang, Phys. Rev. Lett. **117**, 235304 (2016).

[59] P. C. Hemmer, *Kvantemekanikk* (Tapir Akademisk Forlag, 2005).

[60] N. Ashcroft and D. Mermin, *Solid State Physics* (Saunders College, 1976).

[61] J. Bardeen, L. N. Cooper, and J. R. Schrieffer, Phys. Rev. **108**, 1175 (1957).

[62] N. N. Bogoliubov, V. V. Tolmachev, and D. V. Schirkov, *A new method in the Theory of Superconductivity* (Consultants Bureau, 1959).

[63] A. L. Fetter and J. D. Walecka, *Quantum Theory of Many-Particle Systems* (Dover Publications, 2003).

[64] C. Kittel, *Quantum Theory of Solids* (Wiley, 1963).

[65] C. Tsallis, Journal of Mathematical Physics **19**, 277 (1978).

[66] M.-w. Xiao, ArXiv e-prints (2009), arXiv:0908.0787 .

[67] K. L. Lee, N. B. Jørgensen, I.-K. Liu, L. Wacker, J. J. Arlt, and N. P. Proukakis, Phys. Rev. A **94**, 013602 (2016).

[68] S. Dürr, "Lecture Notes on Ultracold Quantum Gases 1," (2016), unpublished.

[69] S. Dürr, "Lecture Notes on Ultracold Quantum Gases 2," (2016), unpublished.

[70] W. D. Phillips, Rev. Mod. Phys. **70**, 721 (1998).

[71] S. Stellmer, B. Pasquiou, R. Grimm, and F. Schreck, Phys. Rev. Lett. **110**, 263003 (2013).

[72] E. Hecht, *Optics* (Addison-Wesley, 2002).

[73] C. Becker, P. Soltan-Panahi, J. Kronjäger, S. Dörscher, K. Bongs, and K. Sengstock, New Journal of Physics **12**, 065025 (2010).

[74] L. Duca, T. Li, M. Reitter, I. Bloch, M. Schleier-Smith, and U. Schneider, Science **347**, 288 (2015).

[75] G.-B. Jo, J. Guzman, C. K. Thomas, P. Hosur, A. Vishwanath, and D. M. Stamper-Kurn, Phys. Rev. Lett. **108**, 045305 (2012).

[76] J. J. Sakurai and S. F. Tuan, *Modern Quantum Mechanics* (Addison-Wesley, 1994).

[77] K. Wódkiewicz, Phys. Rev. A **43**, 68 (1991).

[78] V. Lechner, *Bulk and Structure Inversion Asymmetry in Semiconductor Quantum Well Structures*, Ph.D. thesis, Universität Regensburg (2012).

[79] J. D. Koralek, C. P. Weber, J. Orenstein, B. A. Bernevig, S.-C. Zhang, S. Mack, and D. D. Awschalom, Nature **458**, 610 (2009).

[80] J. Schliemann, J. C. Egues, and D. Loss, Phys. Rev. Lett. **90**, 146801 (2003).

[81] L. Meier, G. Salis, I. Shorubalko, E. Gini, S. Schon, and K. Ensslin, Nat Phys **3**, 650 (2007).

[82] A. J. Olson, S.-J. Wang, R. J. Niffenegger, C.-H. Li, C. H. Greene, and Y. P. Chen, Phys. Rev. A **90**, 013616 (2014).

[83] S.-C. Ji, L. Zhang, X.-T. Xu, Z. Wu, Y. Deng, S. Chen, and J.-W. Pan, Phys. Rev. Lett. **114**, 105301 (2015).

[84] J. Li, W. Huang, B. Shteynas, S. Burchesky, F. Ç. Top, E. Su, J. Lee, A. O. Jamison, and W. Ketterle, Phys. Rev. Lett. **117**, 185301 (2016).

[85] M. A. Khamehchi, K. Hossain, M. E. Mossman, Y. Zhang, T. Busch, M. M. Forbes, and P. Engels, Phys. Rev. Lett. **118**, 155301 (2017).

[86] A. Eckardt, Rev. Mod. Phys. **89**, 011004 (2017).

[87] P. Hauke, O. Tieleman, A. Celi, C. Ölschläger, J. Simonet, J. Struck, M. Weinberg, P. Windpassinger, K. Sengstock, M. Lewenstein, and A. Eckardt, Phys. Rev. Lett. **109**, 145301 (2012).

[88] B. M. Anderson, I. B. Spielman, and G. Juzeliūnas, Phys. Rev. Lett. **111**, 125301 (2013).

[89] Z.-F. Xu, L. You, and M. Ueda, Phys. Rev. A **87**, 063634 (2013).

[90] J. Struck, J. Simonet, and K. Sengstock, Phys. Rev. A **90**, 031601 (2014).

[91] N. Goldman and J. Dalibard, Phys. Rev. X **4**, 031027 (2014).

[92] X. Luo, L. Wu, J. Chen, Q. Guan, K. Gao, Z.-F. Xu, L. You, and R. Wang, Scientific Reports **6**, 18983 EP (2016).

[93] S. Zhang, W. S. Cole, A. Paramekanti, and N. Trivedi, "Spin-orbit coupling in optical lattices," in *Annual Review of Cold Atoms and Molecules - Volume 3.*, edited by K. W. Madison (World Scientific Publishing Co, 2015) pp. 135–179.

[94] T.-L. Ho and S. Zhang, Phys. Rev. Lett. **107**, 150403 (2011).

[95] T. A. Sedrakyan, A. Kamenev, and L. I. Glazman, Phys. Rev. A **86**, 063639 (2012).

[96] T. D. Stanescu, B. Anderson, and V. Galitski, Phys. Rev. A **78**, 023616 (2008).

[97] E. A. Donley, N. R. Claussen, S. L. Cornish, J. L. Roberts, E. A. Cornell, and C. E. Wieman, Nature **412**, 295 (2001).

[98] M. Lewenstein, Physics **1** (2008), 10.1103/Physics.1.13.

[99] L. Zhang, Y. Deng, and P. Zhang, Phys. Rev. A **87**, 053626 (2013).

[100] P. N. Galteland and A. Sudbø, Phys. Rev. B **94**, 054510 (2016).

[101] W. Zwerger, J Opt B Quantum and Semiclassical Opt **5**, S9 (2003).

[102] M. Gong, Y. Qian, M. Yan, V. W. Scarola, and C. Zhang, Scientific Reports **5** (2015).

[103] M. Greiner, O. Mandel, T. Esslinger, T. W. Hansch, and I. Bloch, Nature **415**, 39 (2002).

[104] W. S. Cole, S. Zhang, A. Paramekanti, and N. Trivedi, Phys. Rev. Lett. **109**, 085302 (2012).

[105] S. Sachdev, *Quantum Phase Transitions* (Camebridge University Press, 2011).

[106] A. Altland and B. Simons, *Condensed Matter Field Theory* (Camebridge University Press, 2010).

[107] F. E. A. dos Santos and A. Pelster, Phys. Rev. A **79**, 013614 (2009).

[108] K. Sheshadri, H. R. Krishnamurthy, R. Pandit, and T. V. Ramakrishnan, EPL (Europhysics Letters) **22**, 257 (1993).

[109] J. K. Freericks and H. Monien, Phys. Rev. B **53**, 2691 (1996).

[110] L. Pollet, Comptes Rendus Physique **14**, 712 (2013).

[111] B. Capogrosso-Sansone, N. V. Prokof'ev, and B. V. Svistunov, Phys. Rev. B **75**, 134302 (2007).

[112] K. Byczuk and D. Vollhardt, Phys. Rev. B **77**, 235106 (2008).

[113] P. Anders, E. Gull, L. Pollet, M. Troyer, and P. Werner, Phys. Rev. Lett. **105**, 096402 (2010).

[114] T. D. Kühner and H. Monien, Phys. Rev. B **58**, R14741 (1998).

[115] T. Graß, K. Saha, K. Sengupta, and M. Lewenstein, Phys. Rev. A **84**, 053632 (2011).

[116] Y. Qian, M. Gong, V. W. Scarola, and C. Zhang, ArXiv e-prints (2013), arXiv:1312.4011 .

[117] A. T. Bolukbasi and M. Iskin, Phys. Rev. A **89**, 043603 (2014).

[118] Z. Xu, W. S. Cole, and S. Zhang, Phys. Rev. A **89**, 051604 (2014).

[119] Y. Li, M. R. Bakhtiari, L. He, and W. Hofstetter, Phys. Rev. B **84**, 144411 (2011).

[120] L. He, A. Ji, and W. Hofstetter, Phys. Rev. A **92**, 023630 (2015).

[121] B. Bradlyn, F. E. A. dos Santos, and A. Pelster, Phys. Rev. A **79**, 013615 (2009).

[122] C. Wang, C. Gao, C.-M. Jian, and H. Zhai, Phys. Rev. Lett. **105**, 160403 (2010).

[123] H. Bruus and K. Flensberg, *Many-Body Quantum Theory in Condensed Matter Physics* (Oxford University Press, 2004).

[124] D. Toniolo and J. Linder, Phys. Rev. A **89**, 061605 (2014).

[125] P. N. Galteland and A. Sudbø, Phys. Rev. B **94**, 054518 (2016).

[126] R. H. Landau, M. J. Páez, C. C. Bordeianu, and M. J. Paez, *Computational Physics* (John Wiley & Sons, 2015).

[127] N. Nagaosa, *Quantum Field Theory in Strongly Correlated Electronic Systems* (Springer, 1999).

[128] A. Sudbø, "Kvanteteori for faste stoffer," Unpublished lecture notes.

[129] J. Radić, A. D. Ciolo, K. Sun, and V. Galitski, Phys. Rev. Lett **109** (2012).

[130] I. E. Dzyaloshinskii, Soviet Phys. JETP **19** (1964).

[131] T. Moriya, Phys. Rev. **120**, 91 (1960).

[132] I. Dzyaloshinsky, J. Phys. and Chem. Solids **4**, 241 (1958).

[133] E. H. Hauge, *Go critical!* (2001) , unpublished lecture notes.

[134] T. Skyrme, Nuclear Physics **31**, 556 (1962).

[135] B. Xi, S. Hu, Q. Luo, J. Zhao, and X. Wang, Phys. Rev. B **95**, 014405 (2017).

[136] A. Auerbach and D. P. Arovas, "Schwinger Bosons Approaches to Quantum Antiferromagnetism," in *Introduction to Frustrated Magnetism: Materials, Experiments, Theory*, edited by C. Lacroix, P. Mendels, and F. Mila (Springer Berlin Heidelberg, 2011) pp. 365–377.

[137] L. O. Manuel, C. J. Gazza, A. E. Trumper, and H. A. Ceccatto, Phys. Rev. B **54**, 12946 (1996).

[138] L. Messio, O. Cépas, and C. Lhuillier, Phys. Rev. B **81**, 064428 (2010).

[139] H.-D. Chen and Z. Nussinov, Journal of Physics A: Mathematical and Theoretical **41**, 075001 (2008).

[140] U. K. Rößler, A. N. Bogdanov, and C. Pfleiderer, Nature **442**, 797 (2006).

[141] J. Rowland, S. Banerjee, and M. Randeria, Phys. Rev. B **93**, 020404 (2016).

[142] A. Benyoussef, A. Boubekri, and H. Ez-Zahraouy, Physica B Condensed Matter **266**, 382 (1999).

[143] A. Zheludev, S. Maslov, G. Shirane, I. Tsukada, T. Masuda, K. Uchinokura, I. Zaliznyak, R. Erwin, and L. P. Regnault, Phys. Rev. B **59**, 11432 (1999).

[144] Z. Cai, X. Zhou, and C. Wu, Phys. Rev. A **85**, 061605 (2012).

[145] F. Sun, J. Ye, and W.-M. Liu, Phys. Rev. A **92** (2015), 10.1103/PhysRevA.92.043609.

[146] F. Sun, J. Ye, and W.-M. Liu, Phys. Rev. B **94**, 024409 (2016).

[147] F. Sun and J. Ye, ArXiv e-prints (2016), arXiv:1603.00451 .

[148] C. Wang, M. Gong, Y. Han, G. Guo, and L. He, ArXiv e-prints (2017), arXiv:1603.00451 .

[149] T. Holstein and H. Primakoff, Phys. Rev. **58**, 1098 (1940).

[150] M. Correggi, A. Giuliani, and R. Seiringer, EPL (Europhysics Letters) **108**, 20003 (2014).

[151] R. Kubo, Phys. Rev. **87**, 568 (1952).

[152] N. Schuch, M. M. Wolf, F. Verstraete, and J. I. Cirac, Phys. Rev. Lett. **100**, 040501 (2008).

[153] G. Vidal, Phys. Rev. Lett. **91**, 147902 (2003).

[154] U. Schollwöck, Phil. Trans. R. Soc. A **369**, 2643 (2011).

[155] C. L. Henley, Phys. Rev. Lett. **62**, 2056 (1989).

[156] J. T. Chalker, "Geometrically frustrated antiferromagnets: Statistical mechanics and dynamics," in *Introduction to Frustrated Magnetism: Materials, Experiments, Theory*, edited by C. Lacroix, P. Mendels, and F. Mila (Springer Berlin Heidelberg, Berlin, Heidelberg, 2011) pp. 3–22.

[157] J. Spałek, Acta Physica Polonica A **111**, 409 (2007), arXiv:0706.4236 .

[158] P. A. Lee, N. Nagaosa, and X.-G. Wen, Rev. Mod. Phys. **78**, 17 (2006).

[159] M. Boninsegni, Phys. Rev. B **65**, 134403 (2002).

[160] Y. Nakano, T. Ishima, N. Kobayashi, T. Yamamoto, I. Ichinose, and T. Matsui, Phys. Rev. A **85**, 023617 (2012).

[161] C. Hickey and A. Paramekanti, Phys. Rev. Lett. **113**, 265302 (2014).

[162] Y. Kuno, T. Mori, and I. Ichinose, New Journal of Physics **16**, 083030 (2014).